LABORATORY TESTING TO EVALUATE THE EFFECTIVENESS OF CAPROCKS FOR CO_2 STORAGE

A Thesis

Submitted to the College of Graduate and Postdoctoral Studies

in Partial Fulfillment of the Requirements

for the

Degree of Master of Science

in the

Department of Civil, Geological and Environmental Engineering

University of Saskatchewan

Saskatoon

by

Shahid Mehmood

PERMISSION TO USE AND DISCLAIMER

In presenting this thesis/dissertation in partial fulfillment of the requirements for a Postgraduate degree from the University of Saskatchewan, I agree that the Libraries of this University may make it freely available for inspection. I further agree that permission for copying of this thesis/dissertation in any manner, in whole or in part, for scholarly purposes may be granted by the professor or professors who supervised my thesis/dissertation work or, in their absence, by the Head of the Department or the Dean of the College in which my thesis work was done. It is understood that any copying or publication or use of this thesis/dissertation or parts thereof for financial gain shall not be allowed without my written permission. It is also understood that due recognition shall be given to me and to the University of Saskatchewan in any scholarly use which may be made of any material in my thesis/dissertation.

Requests for permission to copy or to make other uses of materials in this thesis/dissertation in whole or part should be addressed to:
Requests for permission to copy or to make any other use of the material in this thesis in whole or in part should be addressed to:

Head of the Department of Civil, Geological and Environmental Engineering
3B48.3 Engineering Building, 57 Campus Drive
University of Saskatchewan
Saskatoon, Saskatchewan
S7N 5A9 Canada

OR

Dean
College of Graduate and Postdoctoral Studies
University of Saskatchewan
116 Thorvaldson Building, 110 Science Place
Saskatoon, Saskatchewan S7N 5C9
Canada

ABSTRACT

The increased anthropogenic emission of carbon dioxide (CO_2) is a serious concern due to its effects on global climate change. Capture of CO_2 from point sources and storage in the porous rocks of deep saline reservoirs is considered a practical choice for reducing CO_2 emissions into the atmosphere. A fundamental necessity for long-term storage of CO_2 in saline reservoirs is the integrity of non-permeable rock called the caprock. The caprock overlies the porous saline reservoir and prevents migration of CO_2 upwards out of the reservoir. As such, the primary focus of this research is to test the effectiveness of caprock as a seal or barrier to fluid migration under representative conditions of a geological storage site. Additionally, a secondary focus is the assessment of the rock thermal properties and geomechanical modeling of CO_2 injection. This is because thermally induced stress changes resulting from the injection of relatively cold CO_2 can lead to the creation of leakage paths (e.g., formation fracturing or reactivation of existing discontinuities). The study area of this research is the proposed CO_2 injection location of Project Pioneer (TransAlta) in Alberta. The caprock and storage reservoir in the study area are the Calmar and Nisku Formations, respectively.

An experimental setup was developed to measure the permeability of intact and fractured caprock samples exposed to CO_2-rich brine under representative temperature and pressure conditions of the injection site. The objective of determining the permeability of fractured caprock samples exposed to CO_2-rich brine was to examine how caprock seal effectiveness may evolve over time in the presence of fractures which either preexisted or are generated during CO_2 injection. The outcomes were used to assess the collective effects of chemical and physical processes that could lead to caprock leakage.

Geomechanical modeling was conducted in this work to investigate injection-induced stress changes and to see whether their effects (deformation) within the storage reservoir are observed on the ground surface. The models incorporate the thermal, geomechanical and geometrical parameters of the saline reservoir and surrounding rocks.

The permeability of intact samples of the Calmar Formation (primary seal/caprock) were measured as 0.3 nd ($0.3 \cdot 10^{-21}$ m^2), and measured permeability of fractured caprock samples ranged between 10 to 40 µd ($10 \cdot 10^{-18}$ to $40 \cdot 10^{-18}$ m^2). The intact rock permeability is very low, hence, the rate of leakage would be very low ($7.4 \cdot 10^{-7}$ $m^3 s^{-1}$). Potential leakage rates could be up to four orders of magnitude higher if the caprock is fractured from base to top. The geomechanical deformation model predicted that CO_2 injection in the Nisku zone is not likely to cause any significant surface heave (< 2 mm), and it likely too small to be measured effectively using standard surface deformation monitoring techniques. Numerical modeling conducted by a research collaborator using results generated in this research suggests that thermally induced fracturing may occur at the study site if the injection rate is not carefully chosen.

ACKNOWLEDGEMENTS

First and foremost, I would like to express gratitude to my supervisor, Dr. Christopher Hawkes, for his continuous support throughout this research work. Dr. Hawkes provided excellent guidance which will serve me well in my professional career. I would also like to thank my co-supervisor Dr. Yuanming Pan for his help and guidance during this research work. I would like to thank Zig Szczepanik, Donna Beneteau, Brandon Fell, Tom Bonli, Helen Yin and Blaine Novakovski for their help in my laboratory work. Gratitude is also extended to my graduate students colleagues for their support during my graduate studies. I also thank my committee members, Dr. Doug Milne and Dr. Grant A. Ferguson, for their time and guidance.

I appreciate the support of all of my family members but especially to my parents. Finally, I would like to thank the Department of Civil, Geological and Environmental Engineering for providing me the opportunity to do my research work at the University of Saskatchewan. This study was funded in part by Carbon Management Canada.

This thesis is dedicated to my parents and my research mentor.

TABLE OF CONTENTS

LIST OF FIGURES

LIST OF TABLES

LIST OF SYMBOLS AND ABBREVIATIONS

SYMBOLS:

A – cross-sectional area

a – slope of ln (ΔP) vs. time graph

A, B – Skempton pore water pressure coefficients

C_b – bulk compressibility of porous medium

C_{fl} – pore fluid compressibility

d – effective pore diameter

d_{crit} – critical pore diameter

E_d – dynamic Young's modulus E_s – static Young's modulus

g – gravitational acceleration

k – permeability

L– length

n – porosity

P_c – confining pressure

P_{cap} – capillary pressure

P_n – pressure in non-wetting phase

P – pore pressure

P_w – pressure in wetting phase

Q – flow rate

R_1 – upstream reservoir

R_2 – downstream reservoir

S_d – compressive storage of downstream reservoir

S_u – compressive storage of upstream reservoir

t – time

V_1 – volume of upstream reservoir

V_2 – volume of downstream reservoir

V_p – compressional wave velocity

V_p – pore volume

V_s – shear wave velocity

l – thickness of laterally infinite layer through which diffusion (or flow) is occurring

h – depth

ρ – density

ρ_b – bulk density

μ - fluid viscosity

β – Biot's coefficient

ΔP – pressure increment

ΔT – temperature increment

ΔP_1 – pressure increment in reservoir 1 at time 0

$\Delta\sigma_1$ – change in total major principal stress

$\Delta\sigma_3$ – change in total minor principal stress

υ_d – dynamic Poisson's ratio

$\Delta\sigma_v$ – change in vertical stress

ABBREVIATIONS:

BTP – breakthrough pressure

CCS – carbon capture and storage

CO_2 – carbon dioxide

EOR – enhanced oil recovery

GHG – greenhouse gas

IEA GHG – International Energy Agency Greenhouse Gas Program

IFT – interfacial tension

SEM – scanning electron microscope analysis

Syringe pumps – Teledyne-Isco 260D syringe pumps

XRD – x-ray diffraction

GtC – (gigatonnes of carbon)

NON-SI UNITS USED IN THIS WORK:

nd – nanodarcy, a measure of permeability ($\sim 10^{-21}$ m^2)

µd– microdarcy, a measure of permeability ($\sim 10^{-18}$ m^2)

md – millidarcy, a measure of permeability ($\sim 10^{-15}$ m^2)

Mt – megatonne, a measure of mass ($= 10^9$ kg)

1. INTRODUCTION

1.1 Geological Carbon Storage

The increased emission of greenhouse gases (GHG), such as carbon dioxide (CO_2), is a serious concern to both scientists and policy makers due to its implications for global climate change. There has been a marked increase in the concentration of CO_2 in the atmosphere since the industrial revolution (IPCC-WGII, 2007). This imbalance in the global carbon cycle created by anthropogenic activity cannot be simply balanced by natural CO_2 sinks (Falkowski et al., 2000; IPCC-WGII, 2007).

A primary source of anthropogenic GHG emissions comes from the burning of fossil fuels for energy. For example, coal combustion for the production of electricity releases a huge quantity of CO_2 into the atmosphere. Conservation of energy, improving end-use energy efficiency and increased use of renewables can lower CO_2 emissions from power generation. However, due to major technical and economic obstacles such as the inherent intermittent nature of renewable energy sources and incompatibility with the current fossil fuel energy infrastructure, these measures may not result in substantial cuts in CO_2 emission for decades to come (Wilson et al., 2009). Finding a short-term solution that decreases CO_2 emissions while still allowing for the continued use of fossil fuels is an essential component in any effort seeking to slow down the increase in anthropogenic atmospheric CO_2 concentration (Krey and Riahi, 2009; Pacala and Socolow, 2004).

One strategy to reduce GHG is carbon capture and the geological storage of CO_2 (CCS). CCS is a process in which CO_2 is captured from a point source (e.g., power and cement plants) and stored in a geological storage site. In this process, CO_2 is injected deep below the earth's surface into porous rocks of deep saline formations/reservoirs or depleted oil and gas reservoirs (Schrag, 2007, Bruant et al., 2002).

In general, there are three basic categories of storage: deep in the ocean, in terrestrial biomass, and in geological formations (Hepple and Benson, 2005). This is illustrated in Figure 1.1. Sequestration (i.e., storage in geological formations) includes storing the CO_2 in depleted and/or depleting oil and gas reservoirs, in saline reservoirs, or within unmineable coal seams (Holloway,

2001; Bachu and Stewart, 2002; Ennis-King and Paterson, 2002; Hepple and Benson, 2005). The technology associated with storage in geological formations is better understood than the other storage options such as within ocean or in terrestrial biomass.

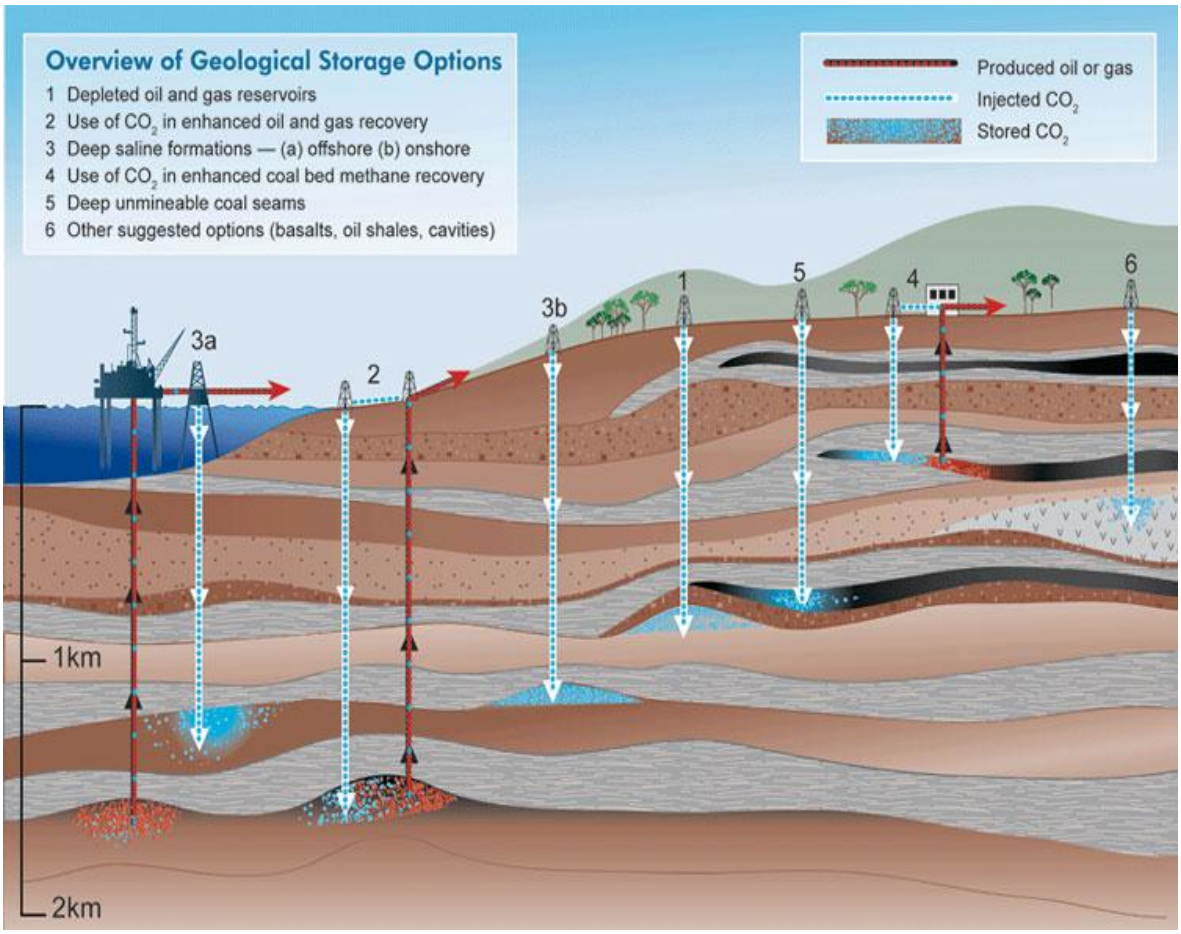

Figure 1.1. Various ways of storing CO_2 in sedimentary basins (geological storage) (IPCC, 2000).

Sequestration in oil and gas reservoirs is the most attractive choice at present. This is because the reservoirs have been comprehensively studied and their geological and physical properties have been characterized, making them ideal candidates for CO_2 storage (Thomas and Benson, 2005). Also, much of the infrastructure required to inject and store CO_2 is already in place (Li et al., 2005). It is believed that these reservoirs have the potential to store 40% of the CO_2 that needs to be removed from the atmosphere (Flin, 2004). CCS in oil reservoir applications can also be combined with enhanced oil recovery (EOR). In this situation, CO_2 is injected into the depleting oil reservoir and this improves oil recovery by causing the oil to flow better. The profits generated from increased oil production can be used to offset the expenses associated with CCS (Bossie-Codreanu, 2008).

As of 2014, operating CCS projects have reduced global CO_2 emissions by approximately 8 Mt (megatonne) annually, corresponding to 0.2% of the estimated globally emitted 37 Gt (gigatonne) (Hangx et al., 2015). Clearly, significantly larger storage volumes are necessary to have a significant impact. A number of studies have been conducted over the past decade to approximate the amount of CO_2 that can be stored in sedimentary basins (Bergman & Winter 1995; IEA 1995; Holloway 1997a; Gunter et al. 1998; Stevens et al. 1999; Benson, 2001; Bachu, 2002). These studies have tried to estimate the pore volume available for CO_2 storage in depleted oil and gas reservoirs, unmineable coal seams and deep brine-filled formations. More recently, Bachu & Adams (2003) and Bachu et al. (2003) have projected that the ultimate CO_2 storage capacity in the deep saline reservoirs of western Canada is of the order of 170Gt. As there is no generally accepted technique to estimate the storage capacity of a particular formation, each of these studies has established a different methodology. However, as shown in Table 1.1, there is general agreement on a number of important issues. First, global storage capacity is more than 1000 GtC (gigatonnes of carbon). Second, brine-filled formations have the maximum capacity, followed by oil and gas reservoirs. Third, the capacity needed for CO_2 storage is greater than the capacity of depleted oil and gas reservoirs. Therefore, storage in brine-filled formations will eventually be required if geological storage is to play an important role in mitigating CO_2 emissions.

Saline reservoirs (commonly referred to as saline formations) have little to no economic value. Saline formations are considered reservoirs because they are porous and contain water. Moreover, their water is four to five times (or more) saltier than ocean water, so it is not drinkable, nor can it

be used for agricultural purposes. As a result, such formations can be used as storage units for greenhouse gasses (GHG) with limited to no impact. These formations cover a large area all over the world, including locations in west-central North America (Farokhpoor et al., 2013). Furthermore, these saline formations are generally found in sedimentary basins that are often located at or very near to many point-source CO_2 emission sites (Bergman and Winter, 1995; Gunter et al., 1996, Hitchon et al., 1999; Bachu, 2008). These formations are the least characterized of the geological storage options because the number of wells drilled into these formations is small compared to the number of wells drilled into resource-bearing rocks such as oil and gas reservoirs (Farokhpoor et al., 2013).

Table 1.1. Storage capacity in sedimentary basins from after (Gunter et al., 2004).

	Global capacity (GTC)	US capacity (GTC)	Canada capacity (GTC)
Depleted oil reservoirs	40-190	10-14	0.6
Depleted gas reservoirs	140-310	20-30	4
Saline formations	87-2700	1-130	>10
Total	267-3200	31-154	>10

1.2 Caprock and Leakage Mechanisms

One important thing that should be taken into consideration in CO_2 geological storage projects is to demonstrate that CO_2 will remain stored for the long term in the geological formation where it is injected, in order to minimize the risk to humans and the environment. According to the IEA-GHG, long-term is defined as a time period ranging from several hundred to several thousands of years (Davison, 2007).

For injected CO_2 to remain secured underground, the storage saline formations must be overlain by formations of very low permeability that serve as geological seals or 'caprocks'. The storage formations are generally chosen to have pressures and temperatures such that the stored CO_2 exists as a dense supercritical fluid phase in order to optimize storage efficiency. However, in the majority of cases, this supercritical CO_2 phase will be less dense than the formation brine. Hence, due to buoyancy, the injected CO_2 will move up to the top of the formation and accumulate under the caprock; for horizontal caprocks, eventually developing into a cone-shaped radial CO_2 plume

(Nordbotten et al., 2005). The injected CO_2 will require many years to dissolve into the brine present in the storage formation.

Storage safety is thus dependent on the caprock's ability to retain the supercritical CO_2 phase over long periods of time. CO_2 leakage through the caprock may occur because of two main physical processes: (i) CO_2 pressure exceeding the capillary breakthrough pressure of the caprock resulting in flow through the caprock matrix at a rate controlled by the intact caprock's permeability to CO_2, and (ii) thermally and/or hydraulically induced fracturing of the caprock due to increasing pore pressure and temperature reduction resulting from the CO_2 injection (Farokhpoor et al., 2013).

1.3 Effects of Temperature and Pressure on Caprock Fracturing

In many cases, the pressurized injected CO_2 is cooler than the native formation temperature. Hence, the pressure and temperature of the formation are affected by the mass and heat transfer between the injected CO_2, native fluids and the rock. These changes have geomechanical consequences such as stress change, displacements and potential fracturing in the formations. To be more specific, this may result in the creation of new fractures or the reactivation or reopening of existing fractures, due to shear and tension in the storage formation and overlying caprock (Rutqvist et al., 2008; Shukla et al., 2010). Any of these fracture-related processes could potentially provide pathways for CO_2 leakage to overlying formations (Smith et al., 2011).

In several cases, the horizontal stress magnitude in the caprock is larger than the reservoir. If fractures are created due to change of temperature and pressure in the reservoir and extend into the caprock then this higher value of caprock stress can limit the fracture growth into the caprock. In some cases, this fracturing of the reservoir formation and caprock (but not the whole caprock) might increase ease of injection of CO_2 into reservoirs without endangering the security of storage. Consequently, it is important to understand initial (in-situ) stress in the reservoir formation and caprock, and how these stresses will change during CO_2 injection.

1.4 Surface Deformation

Temperature and pressure changes resulting from CO_2 injection create local stress changes within the saline reservoir. The deformations resulting from these stress changes are transmitted to the overburden and surface. Surface deformations can result in significant economic losses because of the failure of underground utility lines, well casings, and pipelines, as well as structural damage

generated by seawater intrusions and foundation settlements (Xu et al., 2004). Induced land uplift/subsidence have exceeded several meters in some extreme cases involving subsurface fluid extraction or injection. In some cases, even small subsurface deformations can cause significant damage to the surrounding environment (Nagel, 2001). Extensive research has been done globally on this topic because several regions have been affected by ground surface deformations with detrimental consequences. In most studies, the main objective has been to predict surface deformations so that preventative actions can be taken as quickly as possible in order to minimize damage, optimize production and injection, and develop better monitoring strategies in the future (Geertsma, 1957; Segall, 1985; Vasco, 2004).

In a positive sense, important information can be derived from deformation data for tracking the areas of extraction and injection of fluids. Understanding ground surface deformation during injection operations can be useful for determining whether the injected fluid has remained in its desired target locations (Dusseault et al., 2002).

It is important that appropriate models are used in predicting the induced deformation both in the reservoir formation and at the ground surface. The results help to understand any environmental impact that may result from this surface deformation. It can also be useful to design the monitoring program for a geological storage site.

1.5 CO_2-Brine-Rock Interactions and Change in Permeability

At the CO_2-brine interface, CO_2 dissolution will lead to brine acidification due to generation of weak carbonic acid (H_2CO_3). The dissolved CO_2 concentrations may be on the order of 1 mol L^{-1} at injection depths of 1 km (Duan et al., 2006) and the brine pH may be driven down to as low as 3 (Gunter et al., 2000). This brine acidification may lead to mineral dissolution within the reservoir and potentially, along the base of the caprock, could be detrimental to the caprock seal integrity (Gaus et al., 2008). The existence of fractures within the caprock formation, whether preexisting or generated due to pressurized and comparatively cold CO_2 injection, may serve as leakage pathways for the injected CO_2 (Smith et al., 2011). The permeability of these leakage pathways may increase or decrease due to mineral dissolution or precipitation during the flow of acidic brine through these fractures (Ellis et al., 2011). There have been limited experimental studies examining the impact of CO_2-acidified brine on the seal integrity of caprocks. The most notable investigations

into the evolution of caprock integrity have examined the flow of CO_2-acidified brine through fractures in CO_2 sensitive rocks (Gouze et al., 2003a; Noiriel et al., 2007a; Andreani et al., 2008b). However, these studies tended to examine fairly homogeneous rock cores with simple mineralogy (e.g., clean limestones), thereby avoiding many of the complexities present in naturally heterogeneous rocks. Hence, it is crucial to examine permeability changes occurring in actual caprock lithologies with exposure to CO_2-rich brines.

1.6 Research Study Area

Currently, Canada has an estimated 800 megatonnes (Mt) of annual CO_2 emission. Alberta contributed 114.4 Mt/year of emissions in 2007, which was the highest rate in Canada (Preston et al., 2005). The annual emissions from large stationary power plants in central Alberta are in the order of 30 Mt/yr. These emitters include four coal-fired power plants in the Wabamun Lake area, southwest of Edmonton, which emit between 3 to 6 Mt/year. To mitigate these massive emissions, TransAlta Corporation and its associates Capital Power L.P., Enbridge Inc. and the government of Alberta, Canada led a planned carbon capture, utilization, and storage project entitled Project Pioneer (TransAlta, 2013).

The objective of Project Pioneer was to retrofit coal-fired power plants, situated in the Wabamun Lake area (Figure 1.2), with a carbon capture ability that would capture a total of nearly 1 Mt of CO_2 annually. The CO_2 would have been compressed and transported by pipeline both to a nearby site for injection into the brine-saturated Nisku Formation, and to the more distant Pembina oilfield for consumption in enhanced oil recovery operations. The Project Pioneer study area was chosen based on the results of a previous major integrated study called the Wabamun Area CO_2 Sequestration Project (WASP). The depth of the injection site is approximately 1850 m below surface and fluid pore pressure and temperature at this depth were measured at 17 MPa and 70 ^oC respectively (Keith and Lavoie, 2009).

The Nisku Formation, a saline formation in the study area, was chosen as a CO_2 storage target based on its storage capacity, expected ease of injectivity, low leakage risks and lack of interference with current petroleum production in the area (Shevalier et al., 2010). The storage capacity of this formation is estimated at 1 Gt over 50 years, which is about 2% of the total pore volume available (Eisinger and Jensen, 2009; Ghaderi, 2009). The Calmar Formation, which lies

over the Nisku Formation, is a fine-grained clastic dominated unit of low permeability which acts as a caprock/seal.

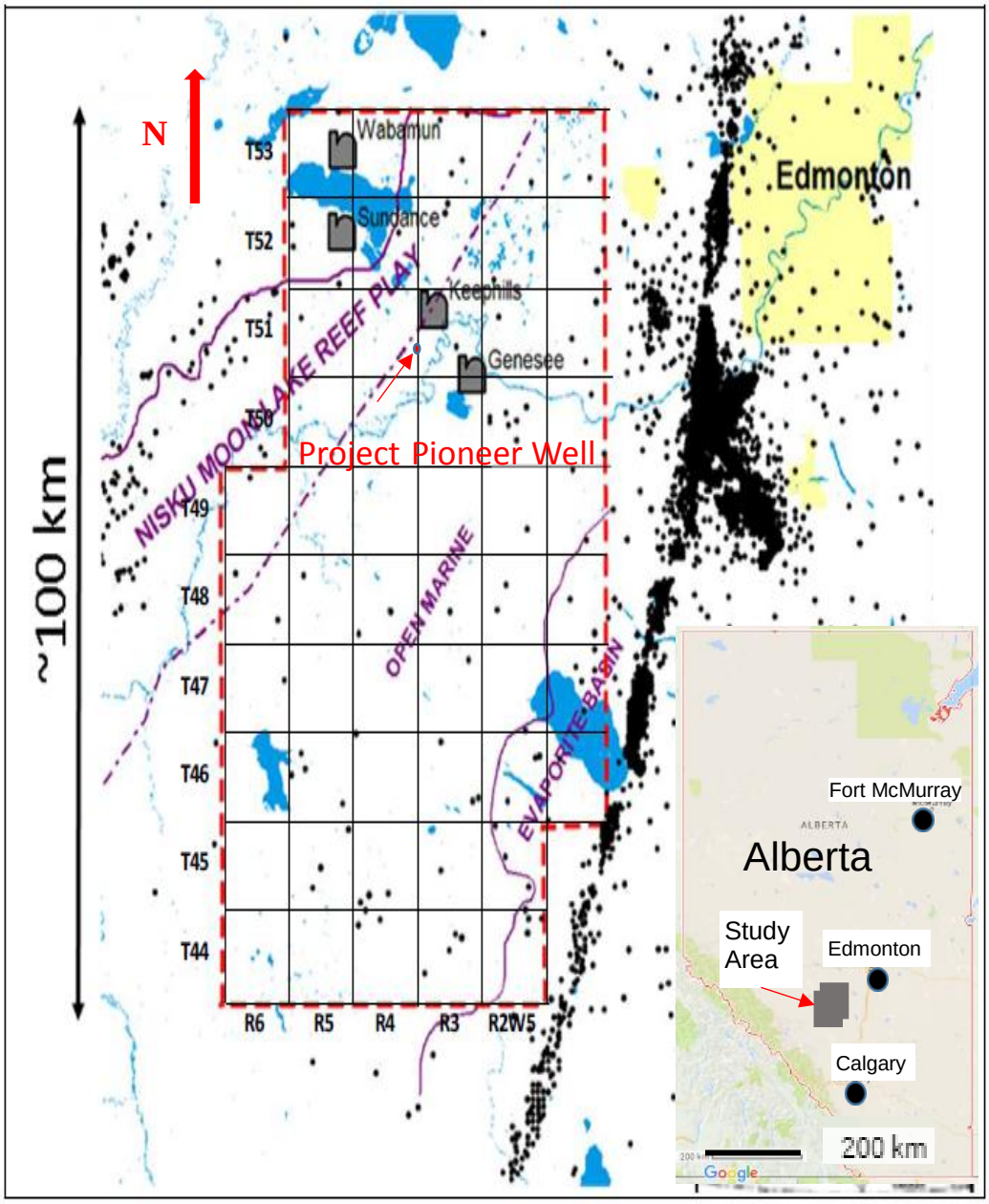

Figure 1.2. The Project Pioneer study area is shown in red dashed line. An arrow identifies the injection well, black dots show other wells and the black rectangles represent coal-fired, CO_2-producing power plants (after Wright, 1994; Google, 2018).

1.7 Research Objectives

The main objectives of this research were:

- To design and conduct laboratory tests to assess the effectiveness of the Calmar Formation (caprock) as a seal at the Project Pioneer geological storage site, and to determine how caprock seal effectiveness may evolve over time. This research hypothesizes that it is possible that pressure and temperature changes during the injection may induce fractures, but these fractures may have low permeabilities, and the rate of permeability change due to rock-fluid chemical interaction will diminish rapidly with time.
- To understand and model the geomechanical and geochemical mechanisms occurring during or after CO_2 injection; specifically fracturing in the Nisku Formation and fracture propagation into the caprock.

1.8 Significance

The outcome of this study will be to provide data that is suitable for analyzing CO_2 containment at the Project Pioneer site. The study also presents experimental methods that are suitable for generating such data for other prospective sites.

1.9 Organization of Thesis

Chapter 2 contains a review of relevant literature associated with this thesis. Chapter 3 describes the experimental design and procedures that were used in this research. Chapter 4 presents and discusses the results obtained from the tests described in Chapter 3. Chapter 5 provides conclusions and Chapter 6 recommendations.

2. LITERATURE REVIEW

2.1 Introduction

This chapter includes a geological description of the study area, a review of measurement techniques unique to low-permeability rocks, a discussion of rock thermal properties which are relevant when injecting relatively cool CO_2 into a porous geological formation, and an overview of geomechanical and geochemical processes that are relevant to injection and secure storage of CO_2.

2.2 Geology of Project Pioneer site

The sedimentary sequence for the Project Pioneer study area can be divided into Cretaceous and pre-Cretaceous (i.e., Mississippian, Devonian, and Cambrian) units. The collective Cretaceous and pre-Cretaceous intervals can be more than 1500 m thick in the area of interest. The upper part of the Paleozoic sequence (Mississippian and Devonian) is marine carbonate and shale dominated, while the Cambrian basal unit consists of passive margin sandstones (Switzer, 1994).

The Cretaceous formations are generally siliciclastics—sandstones, siltstones, and shales. All of the beds dip gently from Northeast to Southwest (NE-SW) at approximately 0.5 degrees on average over the study area. No faults have been identified over the study area (Switzer, 1994).

The Nisku Formation is part of the Winterburn Group. It was deposited after the last phase of the Woodland Group sequence, when the Western Canada Sedimentary Basin was almost filled with shales and carbonates. The Nisku interval represents a strong marine transgression with dominant carbonate ramp deposition (Switzer, 1994). Signs suggest a late stage regressive episode as well, but deposition was reduced during this time in the area of interest (Switzer, 1994).

Figure 2.1 shows a partial stratigraphic chart of the study area; the Nisku Formation and Calmar Formation are shown in the dashed rectangle (Eisinger, 2011; Alberta Geological Survey, 2015). The thickness of the Nisku carbonate accumulation ranges from 40 m near the eastern boundary of the study area to over 100 m closer to the shelf margin. Basinward are hydrocarbon bearing pinnacle reefs (Zeta Pinnacle Trend) and shelf margin reefs (Moon Lake Build-Ups). These mark the western boundary of the possible injection reservoir.

By estimation from wireline geophysical logs at the Project Pioneer injection well site the Nisku Formation has approximately 70 m thickness. The Nisku Formation has an average porosity of 10%, and horizontal and vertical permeabilities 30 md and 3 md respectively (Goodarzi et al., 2012). Although the permeability is not as high as might be desired, this is one of the best injection targets in the Wabamun area due to high storage capacity and low leakage risks in the area (Shevalier et al., 2010). The Nisku Formation is a reservoir containing saline water (brine), but it will be referred as a saline formation in this thesis, to be consistent with much of the literature on CO_2 storage.

The Nisku Formation is underlain by Ireton Formation shales and overlain by the Calmar Formation which is continuous and has an average thickness of 43 m. The Calmar Formation would serve as the primary barrier or seal against leakage of CO_2 injected into lower units. It's estimated porosity, horizontal permeability and vertical permeability are 1%, $30 \cdot 10^{-5}$ md and $7 \cdot 10^{-7}$ md, respectively (Goodarzi et al., 2012).

The upper and lower contacts of the Calmar Formation occasionally appear to be gradational, making the unit difficult to distinguish from bounding strata. The Calmar Formation consists of mottled red and green dolomitic shales and siltstones, interbedded with anhydrite. Relative amounts of carbonate, siltstone, shale and anhydrite are quite variable within the formation in central Alberta. In west-central Alberta, the formation becomes increasingly argillaceous and less silty. The Calmar Formation is overlain by dolomitic siltstones, silty dolomites, and anhydrites of the Graminia Formation (Winterburn Group). In central Alberta, these become burrowed dolomites of the Blue Ridge Member (Graminia Formation), as shown in Figure 2.1.

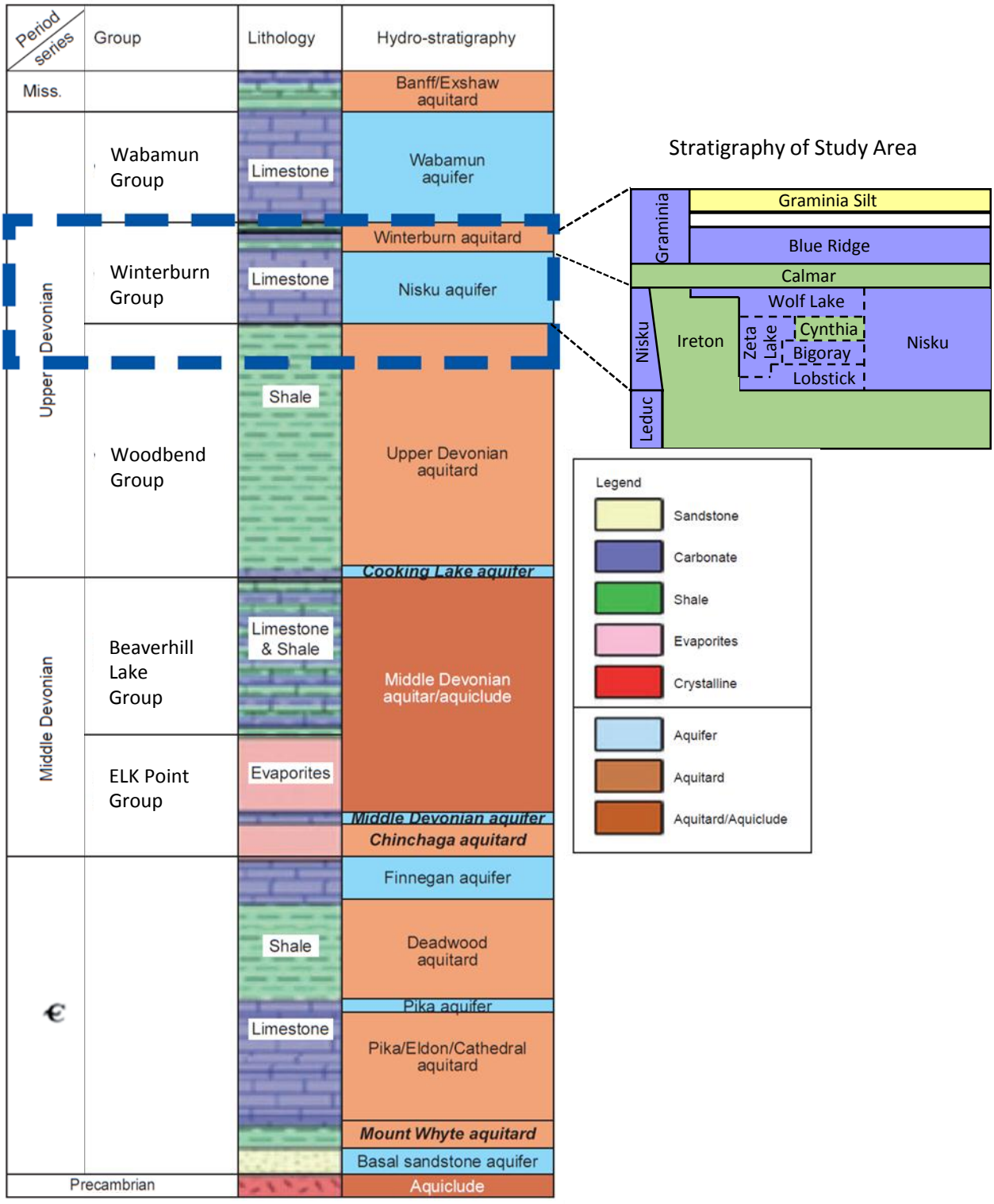

Figure 2.1. This figure shows a partial stratigraphic chart of the study area; the Nisku Formation and Calmar Formation are shown in the dashed rectangle (after Eisinger, 2011; Alberta Geological Survey, 2015).

2.3 Intact Rock Permeability

Regarding long-term CO_2 storage, there are several paths through which leakage may occur. Potentially high leakage rates may be associated with leakage through well casings, along hydraulically-conductive discontinuities or by mechanical failure of the caprock (Shipton et al., 2004; Soltanzadeh and Hawkes, 2008). Assuming that storage sites are properly selected, remediated (as required) and operated so as to mitigate the potential for leakage through such features, then a key question is the leakage potential through intact caprock. In such a case, leakage can occur by overcoming the capillary entry pressure of the caprock, and the leakage rate will be controlled by the permeability of the caprock, or by diffusion (Busch et al., 2008; Chiquet et al., 2007). Chiquet et al. (2007) stated that CO_2 diffusion through a brine-saturated caprock is so slow that it is only significant over geological time scales. This is supported by the work of Busch et al. (2008) who did a series of diffusion experiments on the Muderong Shale of Australia. They concluded that for a 100 meter thick shale, a CO_2 breakthrough by diffusion would occur after approximately 0.3 million years.

Making the conservative assumption that CO_2 capillary pressure will be overcome during large-scale CO_2 injection, an analysis of potential CO_2 leakage rates through caprocks requires the measurement of the permeabilities of these rocks. According to Darcy's Law, the permeability of a porous medium governs the rate of fluid flow occurring in response to an applied pressure gradient. The calculation of rock intrinsic permeability for the flow of an incompressible fluid is typically accomplished by rearranging Darcy's Law as follows:

$$\boldsymbol{k = \frac{L \cdot \mu \cdot Q}{A \cdot \Delta P}} \tag{2.1}$$

Where μ = fluid viscosity (Pa·s)

Q = fluid flow rate at steady-state condition (m^3s^{-1})

L = length of the specimen (m)

A = cross-sectional area of the specimen (m^2) and

ΔP = pressure drop across the sample (Pa)

k = permeability (m^2; often expressed in milidarcy, where 10^{-15} m^2 ~ 1 md)

Unfortunately, the measurements required to calculate permeability using equation 2.1 are often impractical for low permeability rocks. When applying a practical pressure differential across a caprock sample, the flow rates tend to be very small and are difficult to measure accurately (Haskett et al., 1988). Also, the time required to reach steady state can be prohibitively long, and the data is not always reliable (Brace et al., 1968; Dicker and Smits, 1988b; Haskett et al., 1988).

The Gas Research Institute (GRI) method, also known as crushed-rock method (Gunter et al., 1996; Luffel et al., 1993), has become a popular method for measuring permeability of tight rocks or caprocks; however, some studies have shown that this method results in a wide variation in permeability values (Passey et al., 2010; Sondergeld et al., 2010). Furthermore, studies have shown that there are several fundamental limitations to the GRI or crushed-rock permeability technique; e.g., measurements are conducted in the absence of effective reservoir stress, also there are issues related to the particle size of crushed samples and time scales for these measurements.

To determine the permeability of fine-grained rocks, Brace et al. (1968) developed a pressure-pulse decay method. The underlying assumption behind the pressure pulse decay method is to observe the decay of a small change in pressure, which is applied to one end of a sample, as it traverses across the sample (Brace et al., 1968). This method is relevant for determining effective permeability to gas in the presence of a liquid, and for measuring absolute permeability to liquid or gas in single-fluidphase saturation scenarios (Dicker and Smits, 1988b).

In the Brace et al., (1968) technique, a cylindrical sample with pore volume V_p was placed between two reservoirs, one upstream (R_1) and one downstream (R_2), with reservoir volumes V_1 and V_2, respectively (Figure 2.2). The two reservoirs with volumes R_1 and R_2 are simply functions of the testing equipment. The reservoirs on each end of the sample consist of a porous plate that sits flush with the end of the sample, as well as the tubing, pressure transducer(s), and valve(s) that are connected to it. The reservoirs R_1 and R_2 are filled with the test fluid at some initial pressure. A confining pressure, P_c, is applied to the sample that must be greater than the pressures in R_1 and R_2 (Brace et al., 1968; Jones, 1997).

At start time $t=t_0$, the pressure in R_1 and R_2 are equal (Brace et al., 1968; Jones, 1997). The pressure in R_1 is then increased by a small amount, ΔP_1, and when the test fluid flows from R_1 into the

sample, the pressure in R_1 decreases and the pressure in R_2 finally increases, after staying approximately constant initially (Figure 2.3).

To examine the experimental results, in which the pore volume of the sample is small relative to the volumes of R_1 and R_2, the measured pressure difference between R_1 and R_2 is plotted versus time on a semi-logarithmic scale, as shown in Figure 2.4 (Brace et al., 1968; Dicker and Smits, 1988a).

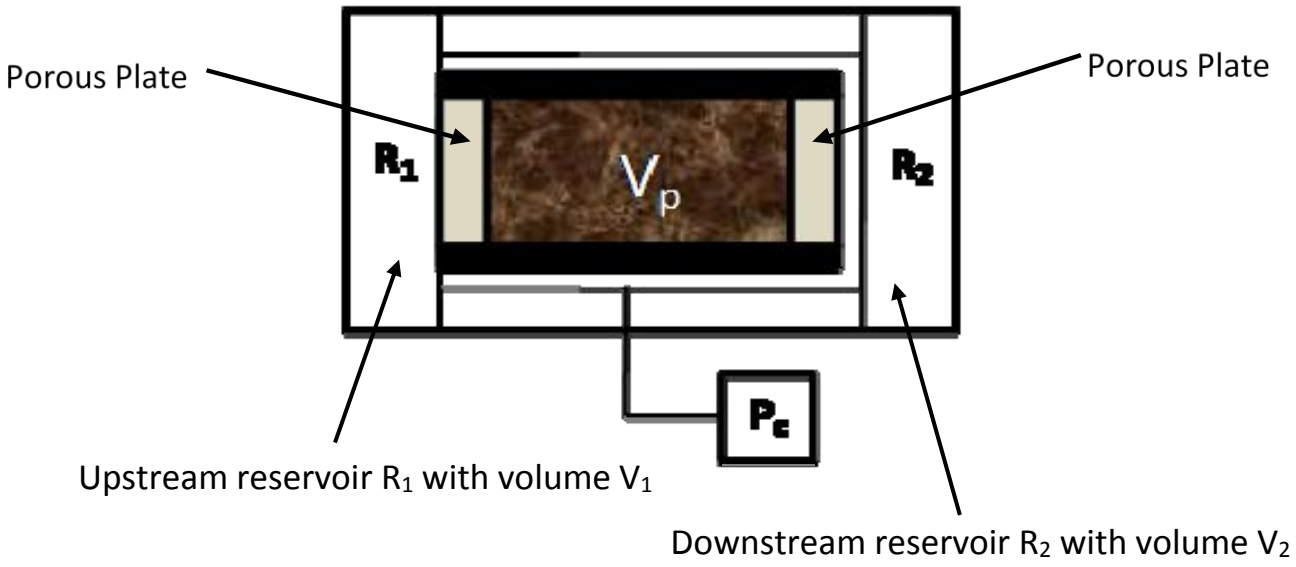

Figure 2.2. Experimental apparatus for pressure-pulse decay permeability testing on a cylindrical sample of volume V_p (Larsen, 2011)

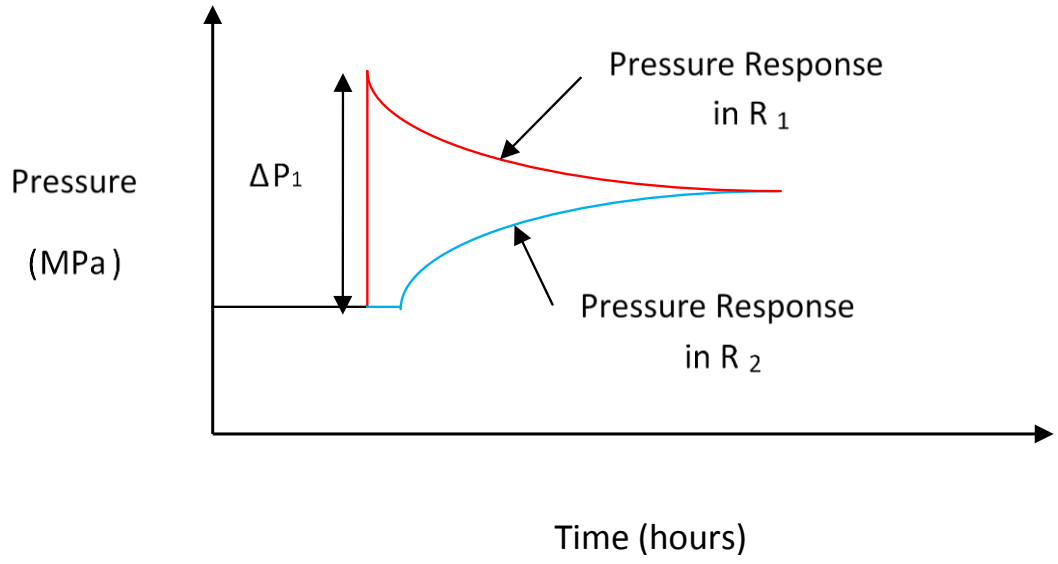

Figure 2.3. Typical experimental results for a pressure-pulse decay permeability test (Larsen, 2011).

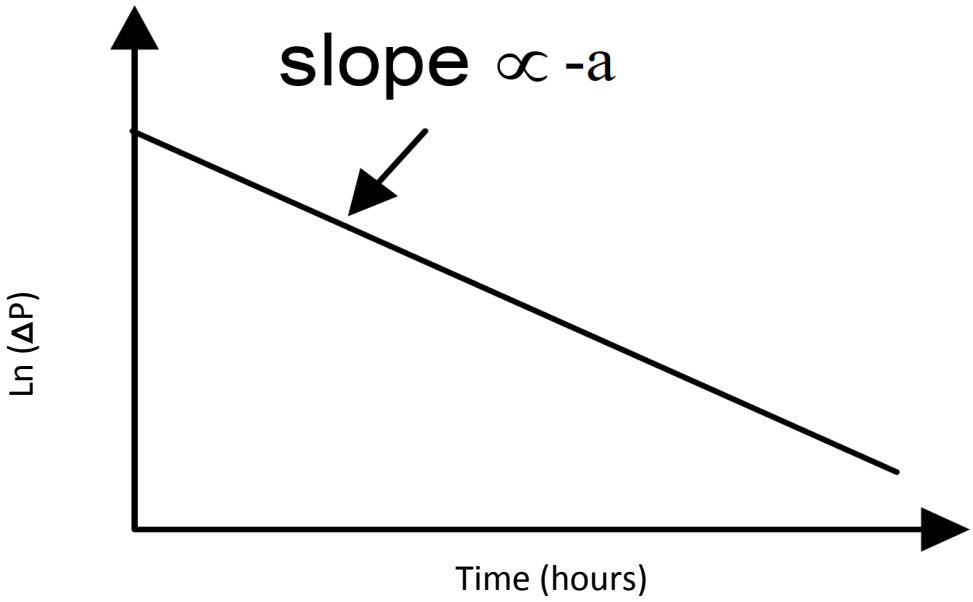

Figure 2.4. A typical plot of permeability test results (Larsen, 2011).

The slope of the straight-line portion of the graph in Figure 2.4 is designated as *a* (s^{-1}) and is used to calculate permeability, *k*, as follows:

$$k = \frac{-a\mu LSuSd}{A(Su+Sd)} \tag{2.2}$$

Where k = permeability (m^2)

a = slope (s^{-1})

μ = fluid viscosity ($Pa{\cdot}s$)

L = length of the sample (m)

S_u = compressive storage of the upstream reservoir ($m^3{\cdot}Pa^{-1}$)

S_d = compressive storage of the downstream reservoir ($m^3{\cdot}Pa^{-1}$) and

A = cross-sectional area of the sample (m^2)

Brace et al.'s (1968) method is considered to provide as an estimate of permeability. Trimmer (1981) observed that the error associated with using equation 2.2 was dependent only on the ratio of the effective pore volume of the sample and the reservoir volumes (R_1 and R_2). If the sample's pore volume is greater than the reservoir volume (i.e., if this ratio is greater than one), then the semi-log plot is not linear and cannot be used to determine a slope. However, if the ratio is less than 0.25, the error associated with using equation 2.2 is 10% or less. Even though the pulse-decay permeability test is conceptually simple, it is a difficult test to implement because it is extremely sensitive to temperature change and small leaks (e.g., through valves or fittings) in the testing system (Larsen, 2011).

2.4 Rock Thermal Properties Relevant to Caprock Integrity

Knowledge of the thermal properties of both reservoir and caprock formations is required in order to assess the geomechanical response to CO_2 injection.Three thermal transport properties (thermal conductivity (λ), volumetric heat capacity (ρC_p), and linear thermal expansion coefficient (α)) control the thermal behaviour of rocks when subjected to temperature change. The first two parameters describe the capability of a material to conduct and accumulate heat, respectively; and the third one is a measure of an amount of strain per unit change in temperature. These parameters

are discussed in more detail in the following sections. Measurements of these thermal properties on Calmar Formation and Nisku Formation samples were performed in this research at the Rock Mechanics laboratory of the University of Saskatchewan.

2.4.1 Thermal Conductivity

The thermal conductivity, λ, of material is defined as the quantity of heat transmitted due to a unit temperature gradient in unit time, under steady-state conditions in a direction normal to a unit area of a given surface. The standard unit of thermal conductivity is $Wm^{-1}{}^{\circ}C^{-1}$ (Somerton, 1992).

Thermal conductivity depends on many factors such as the thermal conductivities of constituent phases, their corresponding volume fractions, the contact areas between these phases and their distribution within the medium, the shapes of particles, and the type of packing. In rocks and soils, pore volume and pore network characteristics influence thermal conductivity. More specifically, it has been shown that magnitude of the porosity, and size, shape and orientation of pores have considerable effects on thermal conductivity. Rocks are generally poor conductors of heat and have a comparatively narrow range (0.1 to 7 W $m^{-1}{}^{\circ}C^{-1}$) of thermal conductivity (Sass et al., 1971).

2.4.2 Heat Capacity

The heat capacity, *C*, of a substance is the amount of thermal energy required to change its temperature by one degree. The units are energy per degree. The heat capacity is an extensive variable since a large quantity of matter will have a proportionally large heat capacity. It is generally more useful to quantify heat capacity per unit mass (specific heat capacity) or per unit volume (volumetric heat capacity) of a substance. For example, the specific heat capacity is the amount of heat required to change the temperature of a unit mass of a substance by one degree. Specific heat capacity is an intensive variable and has units of energy per mass per degree. Volumetric heat capacity is also an intensive variable and is obtained by multiplying specific heat capacity by the bulk density of a substance.

The SI units of specific heat capacity (C_p) are $Jkg^{-1}{}^{\circ}C^{-1}$. The range of variation of the heat capacity of solids in general, and rocks in particular, is even narrower than the range of thermal conductivity. The dependence of specific heat capacity on porosity is governed by the specific heat capacities of the pore fluids and minerals grains present in the solid phase (Somerton, 1992).

Typical values of specific heat capacities are between 0.5 to 3 $\cdot 10^{-3}$ $Jkg^{-1\circ}C^{-1}$ (Huotari and Kukkonen, 2004).

2.4.3 Thermal Diffusivity

Thermal diffusivity represents the ratio of heat transmission and energy storage capacity of a substance, and is calculated as follows (Somerton, 1992):

$$\kappa = \frac{\lambda}{C_p \rho} \tag{2.3}$$

Where, κ = thermal diffusivity (m^2/s)

λ = thermal conductivity ($Wm^{-1\circ}C^{-1}$)

ρC_p = volumetric heat capacity ($Jm^{-3\circ}C^{-1}$)

The above equation shows that thermal diffusivity varies in a manner similar to that of thermal conductivity. Thermal diffusivity of rocks is generally a strong function of temperature and its value decreases with increasing temperature (Somerton, 1992). Rocks generally have values of thermal diffusivity of 3 to 18 $\cdot 10^{7}$ (Bergman and Winter, 1995; Collieu et al., 1975).

2.4.4 Linear Thermal Expansion Coefficient

The linear thermal expansion coefficient (with unit $^\circ C^{-1}$or $\mu\xi\ ^\circ C^{-1}$) of a material is a fundamental physical property which can be of considerable importance in mechanical and structural design applications because of its effect on thermally produced stresses. In rocks, its value depends on constituent minerals and their crystallographic orientation. The typical range of thermal coefficient values is up to $36 \cdot 10^{-6}\ ^\circ C^{-1}$ (Huotari and Kukkonen, 2004). The existence of pores and cracks may affect or change the anisotropy of thermal expansion (Cooper and Simmons, 1977). Cooper and Simmons (1977) observed in their study that granite samples which had the maximum anisotropy in crack distribution also had the maximum anisotropy in linear thermal expansion coefficient. However, they noticed that with increasing temperature the anisotropy of the linear expansion coefficient decreased. This is probably due to the creation of new cracks, which are possibly isotropically orientated in comparison to the original cracks that are generally anisotropic in orientation.

2.5 Induced Poroelastic and Thermoelastic Stresses and Surface Deformation

Induced stresses are generated due to changes in temperature and/or pore pressure of rock masses. Applications resulting in induced stresses include fluid production from hydrocarbon reservoirs, fluid injection for enhanced oil recovery, and greenhouse gas sequestration. The geomechanical effects could include rock deformation, induced fracturing and fault reactivation. Potential detrimental results could include ground movement from subsidence or expansion, well failures, reservoir fluid leakage, and earthquakes. Due to these associated risks, performance assessments of injection or production projects should include geomechanical monitoring and modeling of induced stresses, to measure and predict the induced stresses in order to avoid possible damaging consequences (Du and Olson, 2001; Nagel, 2001; Hermansen et al., 2000; Bruno, 1992).

2.6 Geophysical Monitoring Techniques

Different geophysical techniques can be used to monitor surface deformation. These include Interferometric Synthetic Aperture Radar (InSAR), tiltmeters, and Differential Global Positioning Systems (DGPS). Surface deformation monitoring techniques are generally applicable only onshore. The only exception is tiltmeters which are installed to monitor bottom-based sea structures. They have not been, however, used in larger arrays yet (McColpin, 2009).

2.6.1 InSAR

InSAR is a satellite-based radar measurement technique used for surveying large areas of the earth's surface in order to detect ground deformation (McColpin, 2009). For InSAR, a satellite is programmed to collect ground deformation over an area of interest which normally covers 2,500 to 10,000 km^2. InSAR takes measurements at regular intervals of time and calculates changes to elevation between time periods, with an accuracy in the centimeter to millimeter range after eliminating atmospheric errors.

Three main benefits of this approach are: the cost efficiency due to the collection of a vast quantity of data remotely, the ability to examine the heterogeneity of the mechanical properties of the reservoir, and the availability of data to estimate the flow properties. Henschel et al. (2014) used Interferometric Synthetic Aperture Radar (InSAR) to measure surface deformation during injection and production operations of fluids and they successfully applied this technique for monitoring remotely Enhanced Oil Recovery (EOR) activities.

The accuracy of InSAR can be improved through integration of DGPS and tiltmeter data. This provides finer resolution over smaller areas (McColpin, 2009). Differences between images are usually represented as coloured bands with each band representing an interval of ground movement. This technology is now being used in various modified formats, notable examples are DInSAR (Differential Interferometric Synthetic Aperture Radar) and PSInSAR (Permanent Scatterers) (Onuma et al., 2011).

InSAR works best in areas with consistent radar reflections and can be problematic within areas of dense vegetation, or in areas with natural variations in the surface caused by frost or wetting-drying cycles. These conditions mask the changes that occur due to pressure changes (Parry, 2007).

A study was done by Henschel et al. (2014) in which they collected two years (2009 to 2011) space-based SAR data in order to better understand injection operations and their resultant surface deformation at a SAGD site in Alberta, Canada. At the SAGD site, oil fields were operational for many years. The data was taken from the satellite archives and advanced InSAR processing techniques were applied. The InSAR results showed ground deformation between 1 to 35 mm at the SAGD site. History matching with InSAR observation at the SAGD site provided enhanced prediction and estimation of reservoir growth, which helped in making decisions related to reservoir performance and caprock integrity.

2.6.2 Differential Global Positioning Systems (DGPS)

DGPS is a sophisticated monitoring technique which uses a minimum of two GPS receivers and a sophisticated Kalman filtering algorithm (reference data) to achieve measurements of millimeter-level accuracy of horizontal and vertical motion. One receiver is usually located in an area that is relatively stable and the second receiver is located in region of interest where motion is expected. By using the two stations, atmospheric variations can be identified and backed out, resulting in the desired millimeter-level accuracy (McColpin, 2009).

A successful example of the application of DGPS occurred at Cephalonia Island, Greece which showed horizontal displacements between 10 and 35 mm, and vertical displacements of 65 mm in the western part and 30 mm subsidence in the Eastern part of the island due to natural seismic activity in the region. These results are in agreement with InSAR (Lagios et al., 2007). Like InSAR, DGPS readings can be influenced by vegetation or interference caused by buildings, fences and

any other objects which might reflect or delay the GPS signal. DGPS stations are normally used to supplement data retrieved from tiltmeter arrays and InSAR data acquisition system (Mathieson et al., 2010).

2.6.3 Tiltmeter

A tiltmeter is a sensitive form of inclinometer made to measure very minute changes from the vertical position, either on the ground surface or in structures. Tiltmeters are normally deployed in surface arrays where they pick up ground deformations caused by subsurface strain changes, or they can be placed in boreholes (McColpin, 2009). In CO_2 storage projects, tiltmeters can be strategically placed around the site to determine surface deformation caused by the injection process. Readings are commonly taken every few minutes from a surface array by a data acquisition computer and the results are processed daily. Measurements can be collected remotely and sent for interpretation via radio or satellite telemetry. The magnitude of the surface deformation is usually less than a few centimeters, which can be measured with existing tiltmeters (Luquot and Gouze, 2009).

A valuable attribute of tilt measurements is that the surface deformation detected increases with decreasing depth of the strain change. This makes tiltmeters a favourable tool for quick identification of events like out-of-zone fluid migration or caprock integrity failure, which correspond to significant irregularities in the CO_2 storage site behaviour. A disadvantage of the tiltmeters is that they only provide point-related information. An array of many tiltmeters might be required (often far from the injection site) to measure the area of deformation. The anomalies usually do not directly identify the CO_2 plume (Luquot and Gouze, 2009). Another issue is their high sensitivity to Earth tides caused by the gravity effect of the sun and the moon (McColpin, 2009). The gravity tides represent a very large signal for these instruments and need to be suppressed by data processing if present. In this respect, good local knowledge of the tidal variations is essential, based on baseline surveys and simulations carried out before the storage operations commence.

2.6.4 Sample Application

Due to the geographical characteristics of the area, the In Salah CO_2 storage site in the Algerian part of the Sahara desert has become a field laboratory for testing of the InSAR, tiltmeter and

DGPS technologies for the purposes of monitoring CO_2 storage. Results using these techniques have been published by several independent working groups (Onuma et al., 2011; Vasco et al., 2010; Mathieson et al., 2010; Rutqvist et al., 2008; Morris et al., 2011; Shi et al., 2012; Cavanagh and Ringrose, 2011). These investigators have demonstrated the feasibility of monitoring CO_2 migration by monitoring surface deformation (under certain conditions, at least).

2.7 Geomechanical Modelling

2.7.1 Introduction

If a reservoir were a free body, effective stress changes would simply result in its contraction or expansion. However, reservoirs are "attached" to surrounding rock, and this prevents the reservoir from contraction or expansion. Due to the competition between internal driving forces and external constraints, anisotropic changes in total stress may be induced. The magnitudes of stress changes depend on reservoir geometry, mechanical property contrasts between the reservoir and surrounding rock, and the distribution of pore pressure within the reservoir. This phenomenon has been called stress arching (Mulders, 2003). There are different types of model used for geomechanical analysis of reservoirs which may be categorized as analytical models, semi-analytical models, and numerical models. These models are described briefly in the following sections.

2.7.2 Analytical Models

Analytical models have been developed by using basic concepts of uniaxial poroelasticity (Hawkes et al., 2004), reservoir normal compaction (Goulty, 2003) or frictional equilibrium mechanisms (Holt et al., 2004). These are restricted to analyzing stress changes within a reservoir of idealized geometry and simplified fluid flow conditions.

The assumption of uniaxial deformation has been one of the most popular approaches in modelling the thermo-mechanical behaviour of reservoirs. For this type of model, the reservoir is considered to be constrained laterally and to deform solely in the vertical direction. This represents an assumption of a laterally infinite reservoir, but in a practical sense, it does apply to reservoirs that are very thin relative to their lateral dimensions. Uniaxial models are not realistic for reservoirs with aspect ratios (i.e., thickness/length ratios) that are not negligible and/or if there is a significant contrast between the reservoir and the surrounding rock elastic properties.

2.7.3 Semi-Analytical Models

Semi-analytical models essentially use analytical solutions that can only be evaluated using numerical integration procedures. They are often capable of assessing stress changes both within a reservoir and in the surrounding rocks. These model types are based on simplified geometrical and fluid flow assumptions of linear poroelastic material behaviour for the reservoir and the surrounding rocks (Segall, 1985). There are three main theories upon which semi-analytical models for reservoir geomechanical analysis are based:

(1) the theory of strain nuclei (Geertsma, 1957; Segall, 1985);
(2) the theory of inclusions (Segall and Fitzgerald, 1998; Soltanzadeh and Hawkes, 2008); and
(3) the theory of inhomogeneities (Soltanzadeh et al., 2007; Rudnicki, 1999).

The theory of strain nuclei was fundamentally established to solve the equations in an elastic medium for point loading settings, also called singularities, such as point forces, concentrated moments, and centers of dilatation (or compression). However, by integration, this approach was extended to solve problems of distributed loading settings (Love, 1944). The theory of inclusions is one more technique for analyzing elasticity problems, which is different than the approach of strain nuclei models. In this theory, reservoir and surrounding rock have identical elastic properties, whereas in inhomogeneity scenarios, elastic properties of the reservoir are different from the surrounding rock. In this work, the theory of inclusions with a special case of a pennyshaped reservoir is used. The poroelastic stress change equations are as follows:

$$\frac{\Delta\sigma_{H1}}{\beta\Delta P} = \frac{\Delta\sigma_{H2}}{\beta\Delta P} = \frac{1-2\nu}{1-\nu}\left(1 - \frac{\pi e}{4}\right) \tag{2.4}$$

$$\frac{\Delta\sigma_{v}}{\beta\Delta P} = \frac{1-2\nu}{1-\nu}\left(\frac{\pi e}{2}\right) \tag{2.5}$$

Thermo-elastic stress changes can be calculated using a conversion of the analogous poroelastic stress change component, as follows:

$$\frac{\Delta\sigma_{i}}{\eta\Delta T} = \frac{2s(1+\nu)}{1-2\nu}\left(\frac{\Delta\sigma_{i}}{\beta\Delta P}\right) \tag{2.6}$$

Where *i* represents H_1, H_2 *or* V and shown in Figure 2.5.

Also

β = Biot's coefficient

ΔP = pressure increment (Pa)

ΔT = temperature increment ($^{\circ}$C)

$\Delta\sigma_v$ = change in vertical stress (Pa)

$\Delta\sigma_H$ = change in horizontal stress (Pa)

e = reservoir aspect ratio (height/width, where width represents the lateral dimension of the zone in which pressure or temperature has changed)

P = pore pressure (Pa)

η = linear coefficient of thermal expansion ($^{\circ}C^{-1}$)

s = shear modulus of the surrounding rock (Pa)

v = Poisson's ratio of the reservoir and surrounding rock

It is assumed that the elastic properties of the reservoir and overburden are the same, and these properties are isotropic and homogeneously distributed. A positive number indicates compressive stress change.

2.7.4 Numerical Models

To analyze more complicated reservoirs, accounting for more realistic geometries and rock/fluid behaviour, the use of numerical models is required. In recent decades there has been a significant effort towards developing simulation techniques to model deformation and fracturing for petroleum industry applications. Settari and Warren (1994) have developed two different models; the parametric leak-off model and a numerical leak-off model. They tested the effect of injection, relative permeability, thermal effects and pre-existing propped/acid fractures on fracture propagation rates. This rigorous coupling of fracture dynamics with geomechanics as well as fluid flow is very computationally expensive.

Ji et al. (2006) developed a fully coupled reservoir and geomechanical model for modeling hydraulic fracture propagation. Their method ignores the fracture volume and introduces

pressure/stress dependent dynamic transmissibility multipliers for matrix blocks. The goal is to study the effect of fractures on the fluid flow and geomechanical processes.

GEOSIM is a coupled flow, geomechanical and heat transfer model that is effective for analyzing reservoir and caprock response during CO_2 injection (Goodarzi et al., 2012). The GEOSIM models account for poroelastic and thermoelastic effects and apply for both static and/or dynamic fractures.

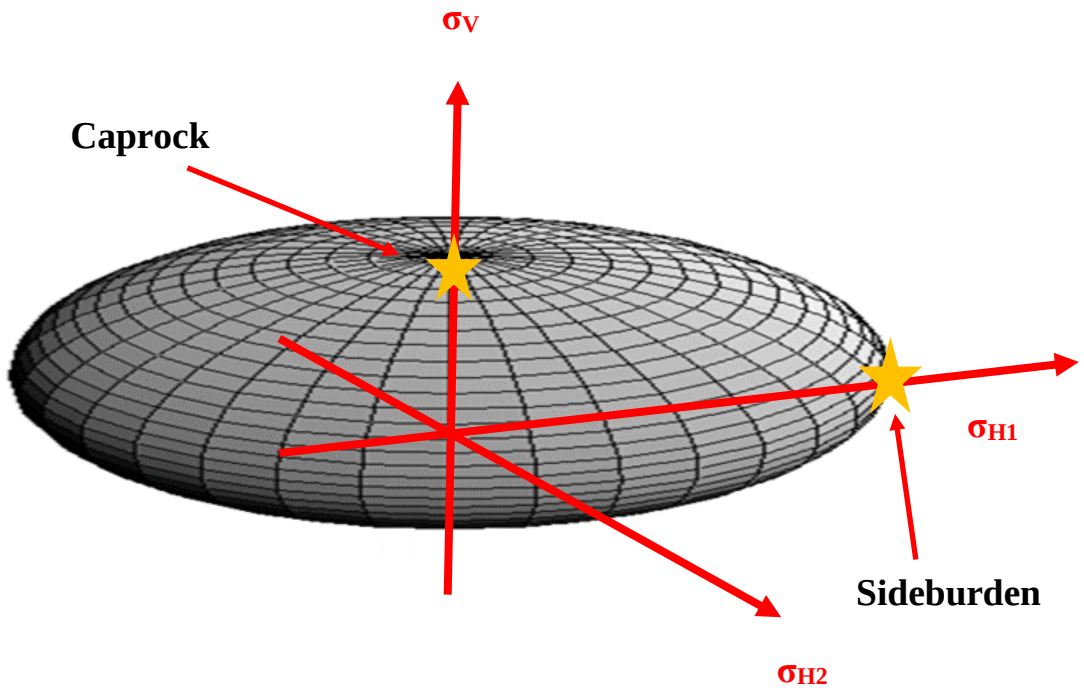

Figure 2.5. Coordinate axis notation used in penny-shaped poroelastic solutions.

2.8 Analytical Models for Temperature Distribution, and Induced Stress Change and Deformation around a CO_2 Injection Well

Knowledge of the temperature distribution around a CO_2 injection well is required to determine the magnitude of the temperature induced stress changes and deformations. An analytical solution presented by Koning (1988) predicts the temperature field around a well which is injected with a fluid of different temperature than the in-situ reservoir temperature. Though Koning's model was developed for water injectors in oil reservoirs, it can also be used for a vertical CO_2 injection well.

Figure 2.6 shows the idealized disk shaped geometry of the fluid front that Koning (1988) used to develop his solution. Koning's solution applies to the injection of an incompressible fluid at a constant rate and assumes that the temperature is constant in the vertical direction inside the reservoir. The model assumes a homogeneous reservoir of a constant thickness (h). Koning's solution also takes into account one-dimensional vertical heat conduction in the cap and base rock while neglecting horizontal conduction. The radius (r) of the fluid front is determined by material balance and the radius of the temperature front inside the reservoir is calculated by assuming simple convective heat balance (Koning, 1988).

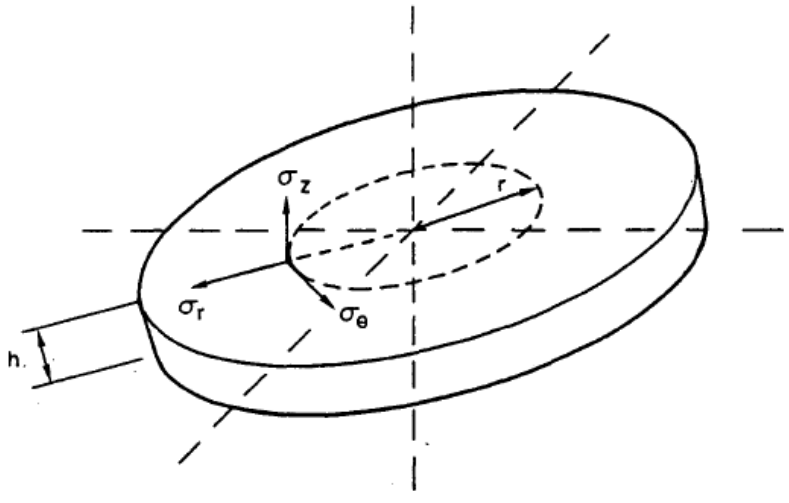

Figure 2.6. The geometry of disk-shaped reservoir.

The equations given by Koning (1988) to calculate the temperature distribution, temperature front and flood front inside the injection reservoir are shown below:

$$R_C = \left(\frac{M_w}{M_r}\frac{qt}{h\pi}\right)^{\frac{1}{2}} \tag{2.7}$$

$$R_F = \left(\frac{1}{\emptyset(1-S_{wr})}\frac{qt}{h\pi}\right)^{\frac{1}{2}} \tag{2.8}$$

$$T_D = \operatorname{erfc}\left(\sqrt{\tau_D}\frac{{R_D}^2}{2(1-{R_D}^2)}\right) \qquad \text{If: } R_D < 1, |z| \leq \frac{h}{2} \tag{2.9}$$

$$= 0 \qquad \text{If: } R_D \geq 1, -\infty < z < \infty$$

Where:

$$T_D = \frac{T - T_{res}}{T_{inj} - T_{res}}$$

$$\tau_D = \frac{4K t {M_s}^2}{h^2 {M_r}^2}$$

$$R_D = \frac{r}{R_c}$$

And:

R_C = radius of temperature front (m)

R_F = radius of flood front (m)

T = final reservoir temperature (°C)

T_{res} = initial reservoir temperature (°C)

T_{inj} = injection temperature (°C)

K = thermal diffusivity of cap and base rock ($m^2 day^{-1}$)

M_w = heat capacity of injection fluid (kJ m^{-3} °C^{-1})

M_r = heat capacity of fluid filled reservoir rock (kJ m^{-3} °C^{-1})

M_s = heat capacity of cap and base rock (kJ m^{-3} °C^{-1})

q = injection rate ($m^3 day^{-1}$)

t = injection time (days)

h = reservoir height (m)

$\emptyset$ = porosity

S_{wr} = residual water saturation

Assuming there is no contrast in mechanical properties between the reservoir and surrounding rock, temperature induced vertical stress change within the reservoir can be calculated using the following equation (Soltanzadeh et al., 2009):

$$\Delta\sigma_V = \eta\Delta T s \frac{(1+\upsilon)}{(1-\upsilon)} \pi e \quad (2.10)$$

Where:

$\Delta\sigma_v$ = change in vertical stress due to temperature change (Pa)

η = linear coefficient of thermal expansion $\left(^{\circ}C^{-1}\right)$

ΔT = reservoir temperature (°C) − injection fluid temperature (°C)

s = shear modulus (Pa)

υ = Poisson's ratio

$$e = \text{reservoir aspect ratio} = \frac{\frac{1}{2}\text{reservoir height (m)}}{\text{temperature front radius (m)}}$$

Thermally and/or pressure induced stress changes will cause expansion/compaction of the reservoir which could lead to some measurable ground surface uplift/subsidence (Figure 2.7 and Figure 2.8). The maximum ground surface uplift/subsidence is assumed to occur at the centre of the injection well. Though equations 2.7 to 2.10 were originally developed in the context of compaction and subsidence for pressure depletion problems, they are also usable for evaluating expansion and uplift (heave) for problems including pressure and/or temperature changes, bearing in mind that the radius of pressure change (i.e., the pressure front) during injection may be significantly greater than the radius of temperature change (i.e., the temperature front).

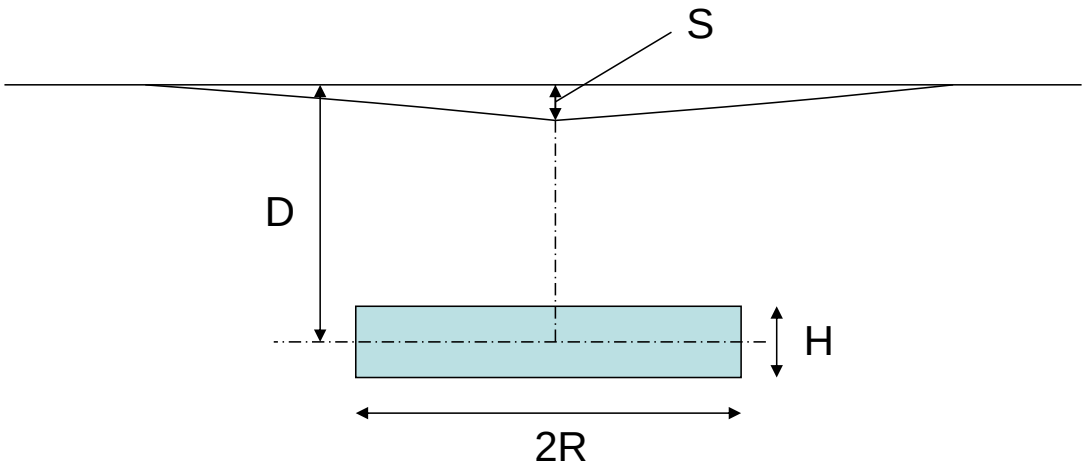

Figure 2.7. Subsidence due to reservoir contraction (e.g., due to fluid withdrawal and/or reservoir cooling).

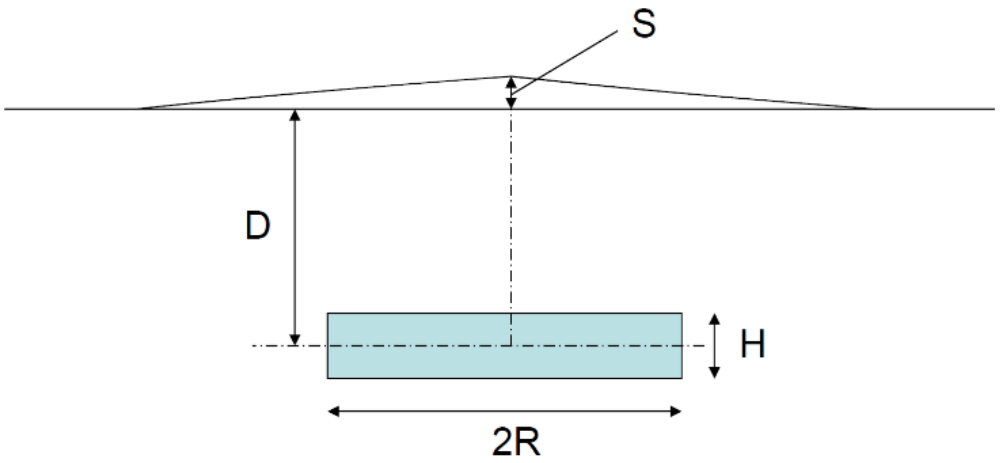

Figure 2.8. Uplift due to reservoir expansion (e.g., due to fluid injection and/or reservoir heating).

To determine the maximum ground surface uplift due to reservoir temperature change based on the method presented by Bruno (1992), a compaction coefficient must be calculated. For isotropic, elastic materials, the uniaxial compaction coefficient can be calculated using the following equation:

$$C_v = \frac{(1-2\upsilon)(1+\upsilon)}{E(1-\upsilon)} \tag{2.11}$$

Where:

C_v = compaction coefficient (Pa^{-1})

υ = Poisson's ratio

E = Young's Modulus (Pa)

Using the compaction coefficient, the uniaxial compaction of the reservoir can be calculated using the following equation:

$$\Delta H = C_v \Delta \sigma'_v H \tag{2.12}$$

Where:

ΔH = unixaxial compaction (m)

H = reservoir height (m)

C_v = uniaxial compaction coefficient (Pa^{-1})

$\Delta \sigma'_v$ = change in effective vertical stress (Pa)

The following equation can then be used to calculate the maximum surface subsidence/uplift:

$$S = 2(1-\upsilon)\left[1 - \frac{1}{\sqrt{1+(R_c/D)^2}}\right] \times \Delta H \tag{2.13}$$

Where

S = surface subsidence/uplift (m)

υ = Poisson's ratio

ΔH = uniaxial compaction (m)

R_c = radius of temperature front (m)

D = depth (m)

2.9 CO_2-Brine-Rock Interactions and Effects on Caprock Integrity

The existence of potential CO_2 leakage pathways from a reservoir into a caprock, and estimates of the volume of CO_2 leakage, have been discussed extensively in literature (Emberley et al., 2005; Celia and Nordbotten, 2009; Damen et al., 2006; Hawkes et al., 2004; LeNeveu, 2008; Lewicki et al., 2007; Viswanathan et al., 2008; Zhang et al., 2010). However, current leakage risk assessment models (LeNeveu, 2008; Viswanathan et al., 2008) do not account for geochemical alterations of the rock surfaces on these pathways in the caprock formations. Leakage pathways are assumed to either exist or not to exist, and the pathway permeability is assumed to be constant over time. Ellis et al. (2011) observed in a fractured carbonate caprock study that modelling could be incorrect without making adjustments to the changes in permeabilitiesof fractures over time, accounting for solid precipitation from fluids and/or dissolution of rock on fracture faces.

Recent research has shown that caprocks provide a less effective seal in a CO_2/brine system than they do in a hydrocarbon/brine system. Therefore, a given caprock which has been effectively sealing hydrocarbons over geological time will not necessarily do so for CO_2. There have been many experimental studies examining the CO_2-brine-rock interactions likely to occur after CO_2 injection into deep saline reservoirs. Most of these studies have investigated the geochemical alterations within the injection formation (Bateman et al., 2005; Izgec et al., 2008; Kaszuba et al., 2003; Le Guen et al., 2007; Luquot et al., 2012; Luquot and Gouze, 2009; Noiriel et al., 2005; Rosenbauer et al., 2005; Shiraki and Dunn, 2000). These studies have demonstrated how low pH created by CO_2 injection can lead to mineral dissolution and subsequent release of metal cations from carbonate and aluminosilicate minerals. These metal cations may later combine with dissolved carbonate ions and truly ‘sequester’ the injected CO_2 in the form of stable carbonate precipitates.

There have been fewer experimental studies examining the impact of CO_2-acidified brine on the seal integrity of caprock formations. The most notable investigations into the evolution of caprock integrity have examined the flow of CO_2-acidified brine through reactive fractures (Andreani et al., 2008a; Gouze et al., 2003b; Noiriel et al., 2007b). However, these studies tended to examine fairly homogeneous rock cores with simple mineralogy (e.g., clean limestones), thereby avoiding many of the complexities present in naturally heterogeneous rocks. Since leakage of CO_2 is most

likely to occur along hydraulically connected flow pathways within the low permeability caprocks, it is crucial to predict the evolution of permeability along these pathways.

Carbonate minerals, such as calcite and dolomite, are known to be reactive when in contact with CO_2 acidified brines (Luquot and Gouze, 2009). Therefore, some degree of geochemical change/reaction is expected along flow paths where CO_2-acidified brine contacts carbonate rocks, such as in hydraulically connected fractures in carbonate caprocks. Characterizing fluid flow and reaction in fractures is challenging due to the interrelationship of these processes and the effects of spatial heterogeneities in fracture geometry and mineral distributions (Berkowitz, 2002; Detwiler, 2010; Dijk et al., 2002). Reaction-induced changes in fracture geometry can alter intrinsic permeabilities and relative permeabilities in ways that are difficult to predict.

It is well known that permeability increases as fracture aperture increase (Snow, 1969), and that flow and permeability decrease due to increase in the roughness of fracture surfaces (Brown et al., 1998; Cavanagh and Ringrose, 2011). Therefore, predictions of long-term seal integrity require an understanding of the complex interplay of CO_2 water-rock interactions and how fluid transport will impact fracture evolution. Although geochemical reactions that alter caprock integrity may take place over the course of hundreds to thousands of years due to slow reaction kinetics (Gaus et al., 2008), important reactions may occur over much shorter time periods, as demonstrated in bench scale experimental investigations (Andreani et al., 2008a; Detwiler, 2010; Ellis et al., 2011, Kaszuba et al., 2005; Shao et al., 2010; Shiraki and Dunn, 2000; Wigand et al., 2009). Experiments conducted at injection temperature and pressure conditions on actual caprock samples offer an opportunity to identify some of the conditions that could control changes in caprock permeability and evolution of reactive leakage pathways.

Previous studies have demonstrated the complex behaviour of fractured limestones when exposed to flow of acidic fluids ($pH \leq 6$), including observations of dissolution of critical fracture asperities (Polak et al., 2003), non-uniform aperture alterations along the fracture surface (Ellis et al., 2011; Gouze et al., 2003b), and particle clogging along the fracture (Noiriel et al., 2007b).

2.9.1 Possible Reactions of Brine with the Fluids and Minerals

Injected CO_2 gas will first dissolve in the water, to turn the CO_2 into an aqueous species ($CO_{2(aq)}$). $CO_{2(aq)}$ will then go through a number of reactions with the fluids and minerals present in the

reservoir and fractures in the caprock. These consist of reaction with the formation water (Emberley et al., 2005), reaction with existing carbonate minerals (Emberley et al., 2005) and reaction with existing carbonate and silicate minerals in the reservoir and fractures in the caprock (Gunter et al., 2000). In the first reaction, $CO_{2(aq)}$ will react with water to produce carbonic acid H_2CO_3 as follows (Emberley et al., 2005):

$$CO_2(aq) + H_2O \leftrightarrow H_2CO_3 \quad (2.14)$$

The aqueous solubility of CO_2 is dependant on temperature, pressure and ionic strength. The concentration of $CO_{2(aq)}$ is generally lower at elevated temperature and salinity and higher at higher pressure (Rosenbauer et al., 2005; Duan et al., 2006; Takenouchi and Kennedy, 1964). This dissolving of CO_2 results in an acidic solution with lower pH because of the dissociation of carbonic acid. This reaction of $CO_{2(aq)}$ with carbonic acid can be represented as:

$$H_2CO_3 + CO_2 \leftrightarrow H^+ + HCO_3^- \quad (2.15)$$

Where, H_2CO_3 is carbonic acid. In equation 2.15, the carbonic acid is available to react with carbonate minerals that may exist in the rock with the net reaction as follows (Emberley et al., 2005):

$$H_2O + CO_{2(aq)} + CaCO_3 \leftrightarrow + 2HCO^-_3 + Ca^{+2} \quad (2.16)$$

This reaction is a very stable and results in an increase in the concentrations of Ca^{+2} and HCO^-_3, which can be monitored geochemically. In the presence of Mg ion, calcite is converted to dolomite as follows:

$$Mg^{+2} + 2CaCO_3 \leftrightarrow CaMg\,(CO_3)_2 + Ca^{+2} \quad (2.17)$$

Where $CaCO_3$ is calcite and $CaMg\,(CO_3)_2$ is dolomite. The third reaction includes $CO_{2(aq)}$ reacting with both carbonate and silicate minerals which may exist in the reservoir or caprock, as shown below (Gunter et al., 2000):

$$CaAl_2Si_2O_8 + CO_{2(aq)} + 2H_2O \leftrightarrow CaCO_3 + Al_2Si_2O_5(OH)_4 \quad (2.18)$$

Where, $CaAl_2Si_2O_8$, is the calcium end member of plagioclase feldspar (anorthite) and $Al_2Si_2O_5(OH)_4$ is kaolinite. In the reaction of equation 2.18, $CO_{2(aq)}$ reacts with a silicate mineral (anorthite) to form calcite. Here the $CO_{2(aq)}$ is converted to a solid phase as calcite.

In relation to potential long-term reactions, quartz mineral reaction dictates the chemical processes of CO_2 in deep saline reservoirs, as the reservoir rocks are generally plentiful in silicate minerals. The common reaction mechanism of quartz is given bellow:

$$SiO_2 + 4H^+ \leftrightarrow Si^{4+} + 2H_2O \quad (2.19)$$

The quartz dissolution rate decreases with increasing pore fluid pH and increases with the existence of cations in the pore fluid (e.g., sodium, calcium, and magnesium) (Kaszuba et al., 2003; Bergman and Winter, 1995; Dove and Crerar, 1990). However, since this quartz dissolution reaction takes a long time to start, this cannot be detected in short-term laboratory studies.

2.10 Summary

It is generally not possible to use the traditional steady-state flow method to determine the permeability of a low-permeability caprock sample. As a result, the pressure pulse decay method developed by Brace et al. (1968) can be used. For this approach, the sample pore volume must be small relative to the reservoir volume used for the test equipment (Trimmer, 1981). Determining permeability using Brace et al.'s method is conceptually simple, but it is difficult to implement because pressure change in the testing system is extremely sensitive to temperature change and small leaks.

During CO_2 injection into a reservoir, increasing pore pressure and the temperature difference between CO_2 and reservoir rock results in geomechanical deformation of both the reservoir and surrounding rocks. One of the most significant concerns about the long-term CO_2 storage is that stress changes caused by injection could lead to formation fracturing, reactivation of fracture networks and fault movements which could potentially provide pathways for CO_2 leakage through previously impermeable rocks. Surface deformations can be problematic if they are large. Monitoring programmes can be implemented to verify if changes are occurring, even if they are small (but large enough to be measured). CO_2 diffusion through a brine-saturated caprock is only significant over geological time and is negligible when compared with volume flow (Chiquet et al., 2007; Li et al., 2005).

Geochemical interactions on caprocks have not been studied extensively, but it is expected that these interactions would occur at the base of the caprock, and would occur very slowly. More

studies are necessary to determine how geochemical interactions affect the porosity and permeability of caprocks.

It is well recognized that chemical reaction between aqueous CO_2 and rock may alter the transport and geomechanical properties of the rock. This can be computed by experimental analysis on the rock formation and the injected CO_2. Established in the WASP (2011) geochemical study, minor quantities of dolomite are predicted to dissolve in reaction with aqueous CO_2 and small quantities of calcite might precipitate in the reservoir (Shevalier et al., 2010).

3. MATERIALS AND METHODS

3.1 Introduction

An experimental investigation was undertaken with the intent of providing data that can be used to assess the permeability of caprock at the Project Pioneer site, to predict thermally induced fracturing or deformation, and to assess initial and time-dependent permeabilities of fractures. This chapter describes the samples and testing procedures used during this research work. All results, except for the mineralogy of the samples, are provided in section 4. Mineralogy is provided in section 3 to show the variability in sample composition.

Table 3.1 summarizes the various tests that were performed on each sample of the Calmar (CMR) and Nisku (NSK) Formation samples. Prior to this research, TeraTek had conducted an extensive array of destructive and non-destructive testing on the Nisku samples, but no thermal property measurements. These Nisku samples were then provided to the author of this thesis for thermal properties measurements. Conversely, the Calmar samples had not been tested prior to this research. Unfortunately, a limited number of these samples were available, and they were only available for a limited time. The tests conducted during this research were as follows:

1. SEM and XRD Analysis of Calmar and Nisku samples. The methodology and results are described in section 3.2.
2. Linear thermal expansion coefficient determination of Calmar and Nisku samples. Details are described in section 3.3.
3. Thermal transport properties determination including thermal conductivity, thermal diffusivity and heat capacity per unit volume of Calmar and Nisku samples. Details are described in section 3.4.
4. Matrix reactivity experiment to measure the reactivity of Calmar samples with CO_2 rich brine. Details are described in sections 3.5.
5. Permeability measurements of intact and fractured Calmar samples. Details are described in section 3.6.
6. Surface profiling of Calmar samples. Details are described in sections 3.7.

Table 3.1. Summary of different tests performed on each sample of Calmar (CMR) and Nisku (NSK) Formation, taken from the Project Pioneer well. The Calmar and Nisku sample diameters were 5.1 cm (2.0 inch) and 3.8 cm (1.5 inch), respectively.

Sample	Depth (m)	SEM Analysis	XRD Analysis	Thermal Expansion Coefficient	Thermal Transport Properties	Matrix Reactivity	Intact Sample Permeability	Fractured Sample Permeability	Surface Profiling
CMR1	1789.00	x	x	x	x			x	x
CMR2	1791.97	x	x	x	x		x		
CMR3	1792.86	x	x	x	x	x			
CMR4	1793.19	x	x	x	x			x	x
NSK1	1796.22			x	x				
NSK2	1805.00			x	x				
NSK3	1807.92			x	x				
NSK4	1839.73			x	x				
NSK5	1844.94			x	x				
Described in Section		3.2	3.2	3.3	3.4	3.5	3.6	3.6	3.7
Stand-aloneTest		Yes	Yes	Yes	Yes	Component of Equipment 3.6	Yes	Yes	Yes

3.2 Sample Description

Core samples (Table 3.1) taken from the Project Pioneer site are shown in Figure 3.1. The samples came from two geological formations: the Nisku Formation (samples 3.8 cm in diameter and roughly 7.6 cm in length), which will be used for storage, and the Calmar Formation (samples 5.1 cm in diameter and roughly 2.5 cm in length), which will act as a primary seal/caprock for this storage site.

In this work, X-ray diffraction (XRD) was used to identify the primary minerals present in some samples (Table 3.2) and to assess mineralogy which may affect CO_2-brine effect which could impact long-term storage of CO_2. This analysis was performed using a Panalytical Empyrean X-ray Diffractometer, at the Geological Sciences Department, University of Saskatchewan. Overall results are contained in Table 3.2 for samples CMR1 to CMR4 which were tested in this work. The results for NSK6 to NSK13 were obtained from the literature (Shevalier et al., 2010).

The results of bulk XRD analysis of CMR3 are shown in Figure 3.2. A section of each sample was cut and polished for SEM analysis. Backscattered electron (BSE) microscopy was used to differentiate between minerals and pore space, and where possible, to distinguish between

minerals. These BSE images were then combined with energy dispersive spectroscopy (EDS) elemental maps, such as those for calcium and magnesium (Figure 3.3). Specific minerals and their percentage contribution to the sample area were identified using an algorithm that overlays the BSE gray-scale images with the EDS elemental maps. For example, the BSE images can be used to separate calcite from dolomite. Dolomite is assigned to regions of the EDS map where calcium and magnesium co-exist, with no other metals present, and where the BSE map has a gray-scale intensity corresponding to the range assigned to dolomite. These area estimates are used as a proxy for the percentage volume contribution of each mineral and represent a semi-quantitative estimate of bulk mineralogy.

Several 2-D images were taken at random locations on each polished section (Figure 3.4 and Figure 3.5). The Calmar Formation mostly consist of small clasts of quartz, micas (predominately muscovite) in a fine clay (illite) matrix, and feldspars (k-spar and albite) (Figure 3.4). Fine-grained pyrite was found in all four Calmar samples analyzed. A significant quantity of replacement dolomitization of the original limestone is apparent in the eight samples of Nisku core analyzed (Shevalier et al., 2010). The Calmar samples were examined by the author at the Geoanalytical laboratory at the Geological Sciences Department, University of Saskatchewan, Saskatoon Canada, and the Nisku samples were analyzed by personnel at the Earth Sciences laboratory, University of Calgary, Alberta, Canada. The outcome of these tests is shown in Table 3.2. More photomicrograph of Calmar and Nisku **s**amples are given in Appendix A.

.

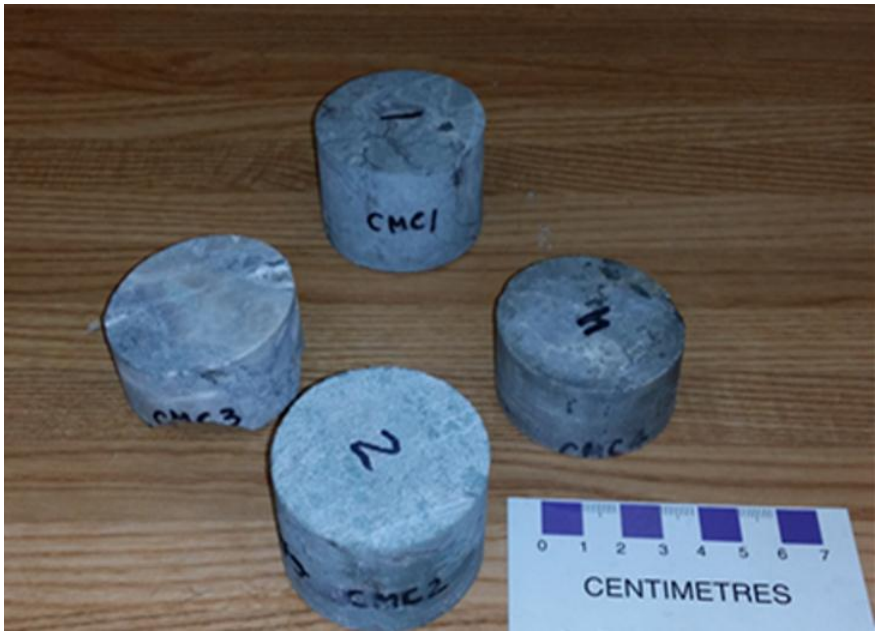

(a)

(b)

Figure 3.1. (a) Calmar, (b) Nisku samples in final form for investigation and experimentation.

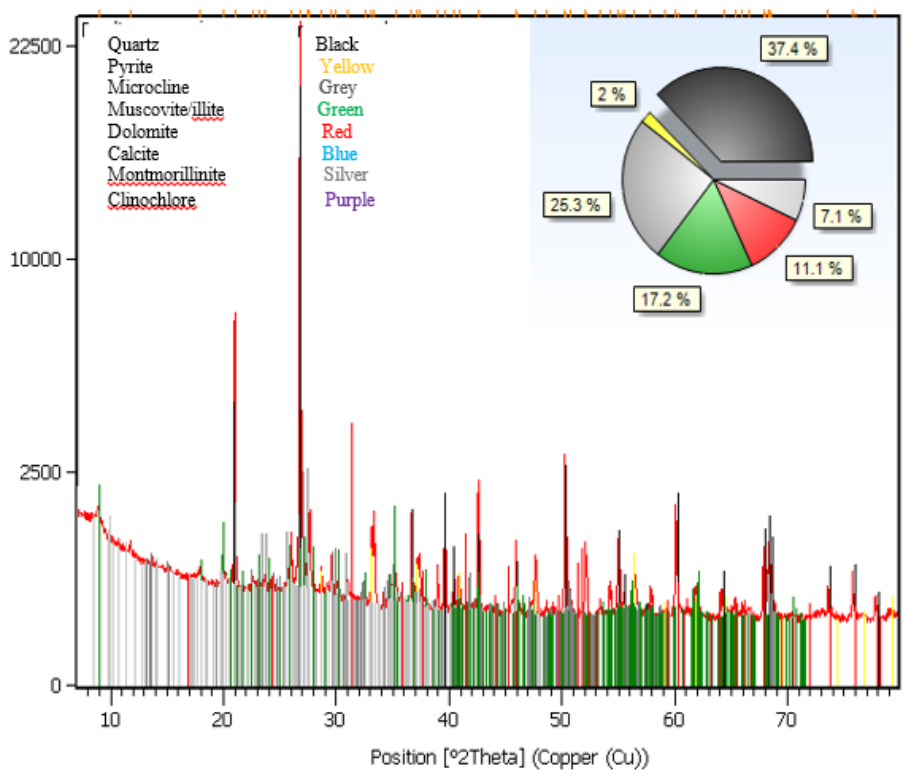

Figure 3.2. Bulk XRD results for Calmar sample CMR3.

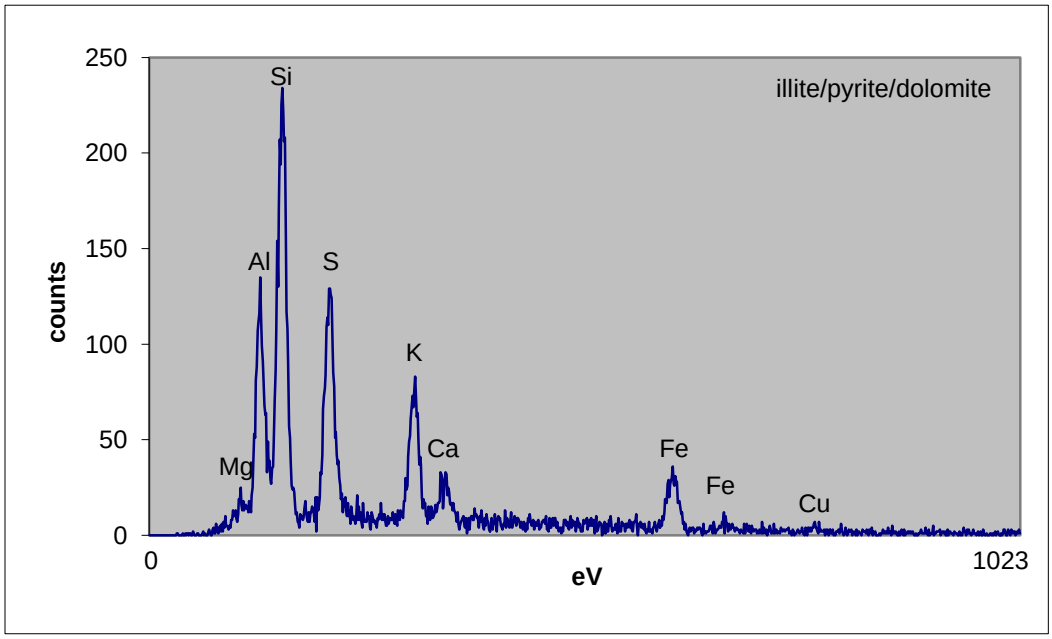

Figure 3.3. EDS spectra of Calmar sample CMR3.

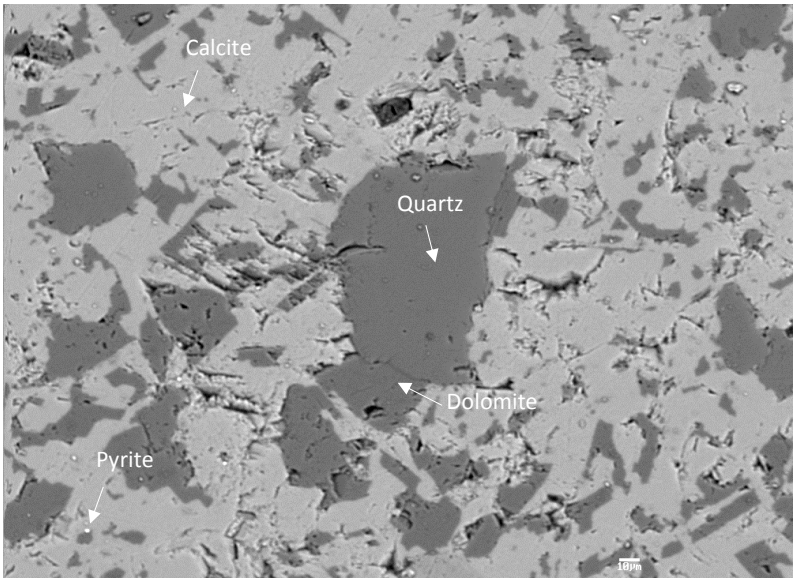

Figure 3.4. Photomicrograph of Calmar sample CMR1. It consists of clasts of quartz, dolomite, calcite and disseminated pyrite.

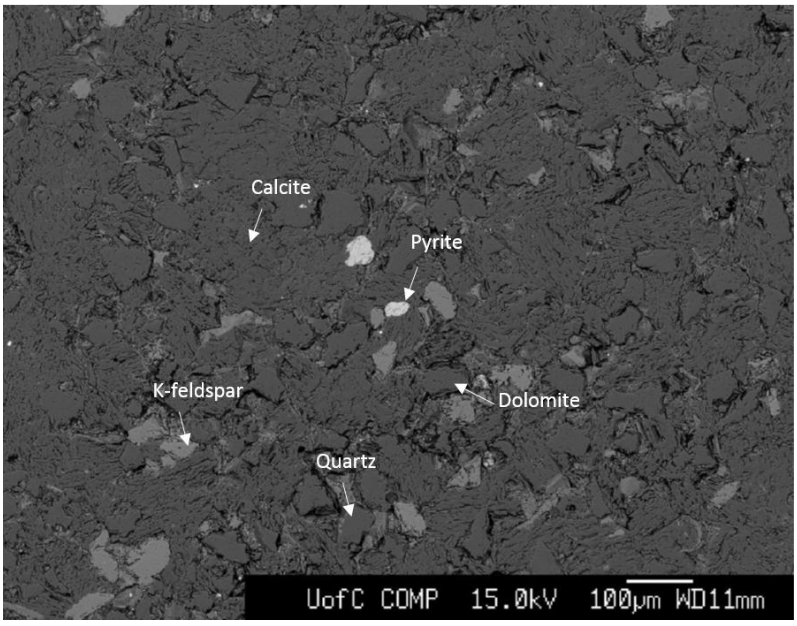

Figure 3.5. Photomicrograph of Nisku sample (NSK8). It consists a significant amount of dolomite and calcite and some pyrite. (Shevalier et al., 2010).

Table 3.2. Quantitative mineral composition (wt%) of Nisku (NSK) and Calmar (CMR) samples. Nisku samples results from Shevalier et al. (2010).

Sample	Calcite	Dolomite	Quartz	Albite	K-spar	Ill/Mus	Anhydrite	Pyrite
CMR1	23.1	9.7	31.4	1.5	11.9	19.6	0.2	1.7
CMR2	14.5	12.3	32.7	3.5	14.2	21.1	0.0	1.4
CMR3	18.6	7.4	31.8	2.4	15.6	22.5	0.0	1.6
CMR4	12.7	14.0	40.5	3.4	12.8	14.7	0.1	1.3
NSK6	6.2	89.2	2.0	0.0	0.2	2.0	0.0	0.0
NSK7	15.2	79.9	0.0	0.6	0.9	1.9	0.0	0.0
NSK8	3.8	52.9	27.6	1.7	5.1	4.4	0.0	1.3
NSK9	5.5	44.4	0.9	0.0	0.4	0.5	47.1	0.0
NSK10	11.7	83.8	1.4	0.5	0.6	0.0	0.0	0.2
NSK11	5.9	90.7	0.3	0.0	0.6	0.0	0.0	0.0
NSK12	5.1	90.2	0.4	0.5	0.3	0.0	0.0	0.2
NSK13	4.7	91.6	0.0	0.0	0.4	0.5	0.0	0.0

3.3 Linear Thermal Expansion Coefficient Experiment

A known method for measuring the expansion coefficient of a test material was used. The technique used two strain gauges with similar expansion characteristics, with one bonded to a specimen of a reference material, and the second to a specimen of the test material.

Various shapes and sizes of samples can be used in this technique as long as specimen size is compatible with the available equipment for heating and cooling. To minimize potential problems related to temperature gradients, the cross-section of the sample should be uniform. Under stress-free conditions, the differential output between the gauges on the two specimens, at any common temperature, is equal to the differential unit expansion. Aside from the basic simplicity and relative ease of making linear thermal expansion measurements by this method, it has the distinct advantage of requiring no specialized instruments beyond those generally found in a stress analysis laboratory (Figures 3.6 and Figure 3.7).

3.3.1 Operating Physical Principle

When a resistance strain gauge is installed on a stress-free specimen of any test material and the temperature of the material is changed, the output of the gauge changes correspondingly. This effect, present in all resistance strain gauges which consist of grid alloy, is commonly referred to as "temperature-induced apparent strain", or "thermal output". The linear thermal expansion coefficient of the grid alloy is usually different from that of the test material to which it is bonded and because of this difference, an additional resistance change occurs. Thus, with temperature change, the grid is mechanically strained by an amount equal to the difference in expansion coefficients. Since the gauge grid is made from a strain sensitive alloy, it produces a resistance change proportional to the thermally induced strain. The thermal output of the gauge is due to the combined resistance changes from both sources. The net resistance change can be expressed as the sum of resistivity and differential expansion effects which can be expressed as shown in equations 3.1 through 3.3:

$$\Delta R/R = [\beta_G + (\alpha_S - \alpha_G) F_G] \Delta T \quad (3.1)$$

Where:

$\Delta R/R$ = unit resistance change

β_G = thermal coefficient of resistivity of grid material ($^{\circ}C^{-1}$)

$\alpha_s - \alpha_G$ = difference in linear thermal expansion coefficients between specimen and grid respectively ($^{\circ}C^{-1}$)

F_G = instrument gauge factor

ΔT = temperature change from arbitrary initial reference temperature ($^{\circ}C$)

According to the definition of strain

$$\varepsilon = (\Delta R/R)/F_G \quad (3.2)$$

Rearranging the terms we get

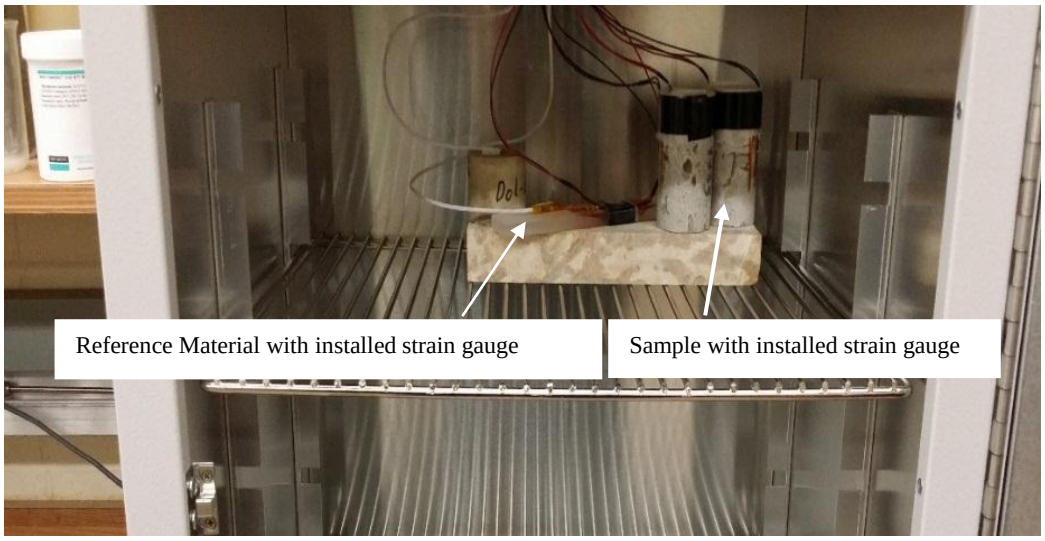

(a)

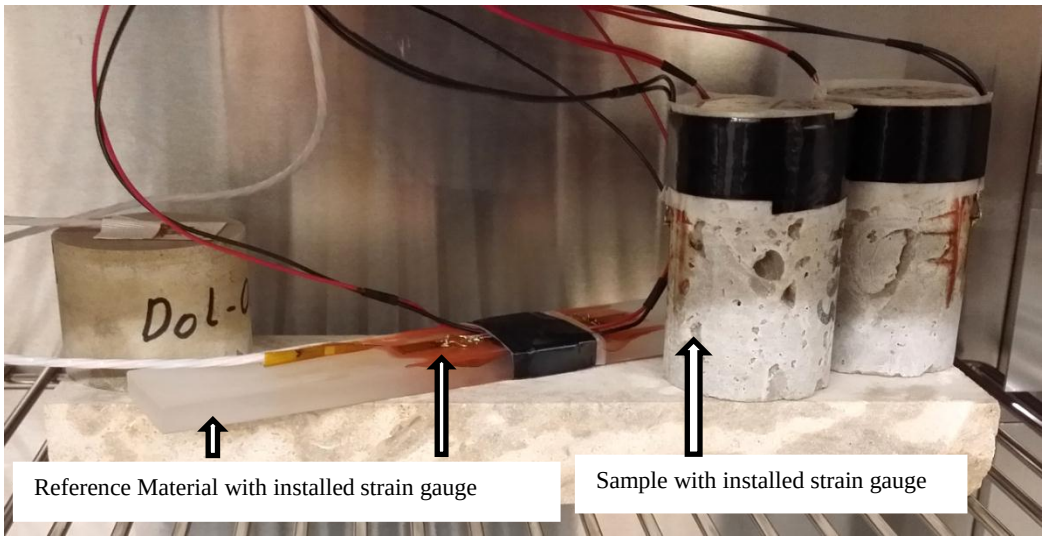

(b)

Figure 3.6. (a) Specimens and reference material with installed strain gauges (brown coloured) in an oven for linear thermal expansion measurements, (b) a close up view of the reference material and sample.

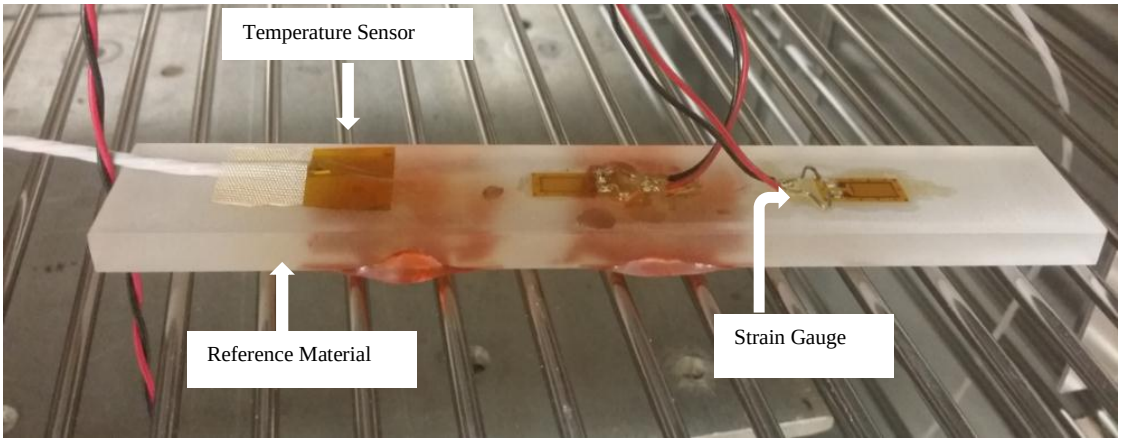

(a)

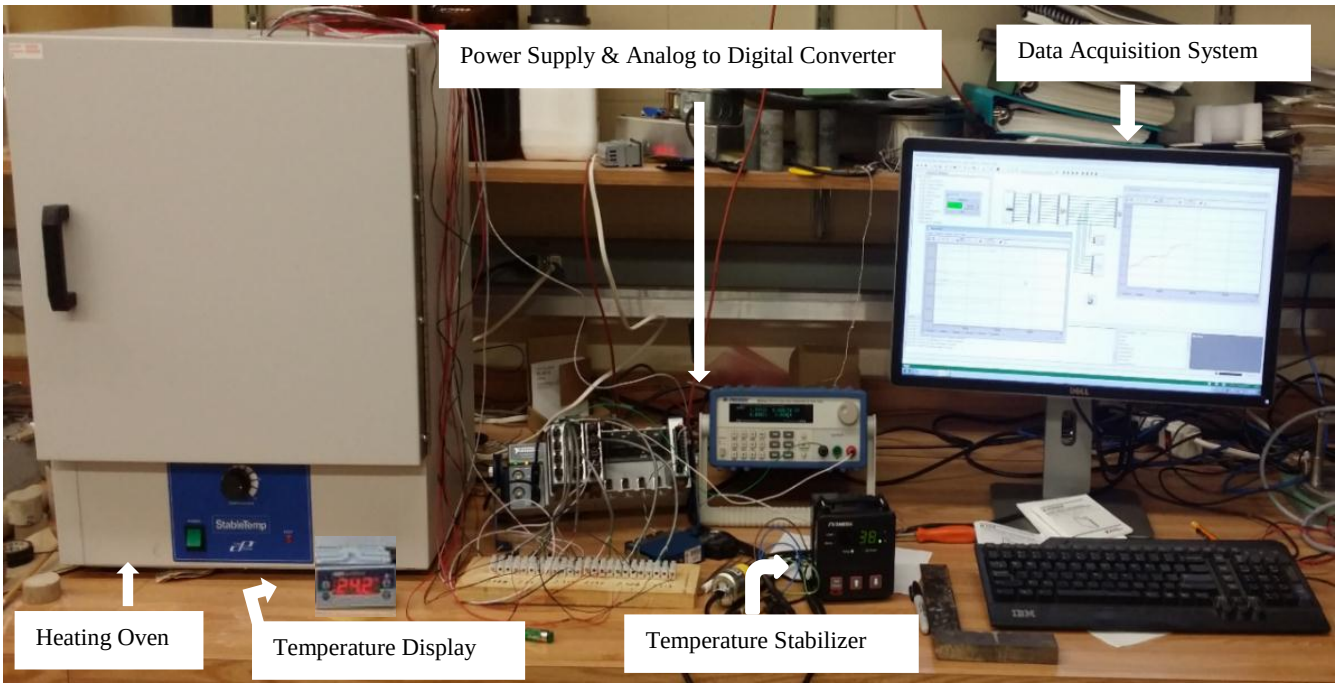

(b)

Figure 3.7. (a) Strain gauges, a temperature sensor attached to reference material, (b) A complete setup, oven with temperature controller (stabilizer), room temperature display with data acquisition system.

$$\varepsilon = [(\beta_{G/} F_{G)} + (\alpha_S - \alpha_G)] \Delta T \quad (3.3)$$

An algebraic demonstration of the principle can be obtained by rewriting equation 3.3 twice; once for the gauge installed on a specimen of the test material of unknown expansion coefficient α_S, and again for the same type of gauge installed on a standard reference material with a known expansion coefficient α_R.

$$\varepsilon_1 = [(\beta_{G/} F_{G)} + (\alpha_S - \alpha_G)] \Delta T \quad (3.4)$$

And

$$\varepsilon_2 = [(\beta_{G/} F_{G)} + (\alpha_R - \alpha_G)] \Delta T \quad (3.5)$$

Subtracting equation 3.5 from equation 3.4 and rearranging,

$$\alpha_S - \alpha_{R =} {}_{(}\varepsilon_1 - \varepsilon_2) / \Delta T \quad (3.6)$$

Thus, the difference in expansion coefficients, at a particular temperature range, is equal to the unit difference in thermal output for the same change in temperature. This technique for measuring expansion coefficients is widely applicable, and often the most practical approach (Feng et al., 2010).

3.3.2 Reference Material

In principle, the reference material could be any substance for which the expansion properties are accurately known over the temperature range of interest. In practice, however, there are some factors to consider which can help to make measurements more feasible and convenient. Firstly, it is often advantageous to select a material with expansion properties as close to zero as possible. This will provide an output signal which closely corresponds to the "absolute" expansion coefficient of the test material, and permits a more straightforward test procedure. Secondly, the thermal expansion of the reference material should be highly repeatable, and stable with time at any constant temperature. Thirdly, the elastic modulus of the material should be high enough so that mechanical reinforcement by the strain gauge is negligible. An excellent example of reference material with these and other desirable properties is ULE™ Titanium Silicate Code 7972 (used in this work), available from Corning Glass Company, Corning, NY 14831 (Figure 3.7 (a)).

3.3.3 Selection of Strain Gauge

The type of strain gauge selected for use in measuring expansion coefficients is an important consideration. Gauge selection usually requires weighing a variety of factors which can directly or indirectly affect the suitability of a particular gauge type to a specified measurement task. Some of these factors are size, shape, and rigidness of the strain gauge within the desired temperature range. In this experimental set-up, a MM CEA-06-250UW-120 gauge was selected (Figure 3.7 (a)).

3.3.4 Gauge Installation

To install a strain gauge, the specimen surfaces were thoroughly cleaned and prepared for bonding. For best accuracy, a high-performance adhesive, MM AE-10 epoxy, was used. This adhesive forms a thin, hard "glue line" for maximum fidelity in transmitting strains from the specimen surface to the gauge. The adhesives are intended for use on relatively smooth, nonporous surfaces, and should not be used where the adhesive is required to fill surface irregularities or to seal pores. For the latter conditions, the recommended adhesive is M-Bond AE-15 (Fox, 1990). Large pores (vugs) were avoided when attaching the gauges to the Nisku samples; the effects of these features on the thermal properties of these samples are unknown.

While attaching lead wires to the gauge, solder terminals were made smooth, bright, and free of spikes or excess solder. The joints were made as uniform as possible, and the lead wires were installed the same way on both specimens. After lead wires had been attached, the gauge installations were thoroughly cleaned with resin solvent to remove all traces of soldering flux and residues. A photograph of samples and reference material with installed strain gauges are shown in Figure 3.6 and Figure 3.7 (a).

Two basic circuit arrangements can be used in measuring expansion coefficients. The arrangement is shown in Figure 3.8(a), used in this research, employs separate three wire quarter bridge circuits for the gauges on the reference and test specimens. With this arrangement, the gauge outputs are read individually and subsequently subtracted to determine the differential strain.

The second arrangement, shown in Figure 3.8 (b), uses the properties of a half-bridge circuit to perform the subtraction electrically. The two gauges in this circuit are connected to adjacent arms of the bridge circuit, and the instrument output is equal to the difference in the individual thermal

outputs. The circuit is obviously simpler in terms of both wiring and instrumentation and gives a direct reading. However it is difficult to isolate a malfunctioning gauge, so it was not used in this research.

Temperature measurement requires care to obtain accurate expansion data. Typically, a temperature-sensing probe is placed immediately adjacent to the gauge, and in contact with the specimen surface, to indicate the specimen/gauge temperatures.

Depending on personal preference, instrumentation availability and desired precision, temperatures can be measured either with thermocouples or with a resistive temperature device (RTD). In this testing, a RTD was employed for temperature measurement because it is more sensitive and precise for the range of interest than a thermocouple. A close up of a temperature sensor, reference material and strain gauge are shown in Figure 3.7 (a). A complete set up of linear thermal expansion coefficient experiment is shown in Figure 3.7 (b). Also, a temperature stabilizer (Figure 3.7 (b)) was used, as unacceptable fluctuations in temperature were observed when the oven's built-in thermostat was used.

3.3.5 Special Precautions for Minimizing Error

Sources of error in the experiment were identified in order that they could be removed or minimized. Each of the items in the following checklist were taken into account in this experimental design:

1. Ensure stable, accurate instrumentation, for both temperature and strain measurement.
2. Select high-quality strain gauges which exhibit negligible drift over the operating temperature range.
3. Maintain gauge excitation at a level low enough to avoid self-heating effects.
4. Ensure the thermal conditions of specimens, gauges and wiring are stable prior to making expansion measurements.
5. Avoid significant thermal stresses during heating and cooling.
6. Eliminate frictional effects preventing free expansion and contraction by placing samples on a rail in the oven.

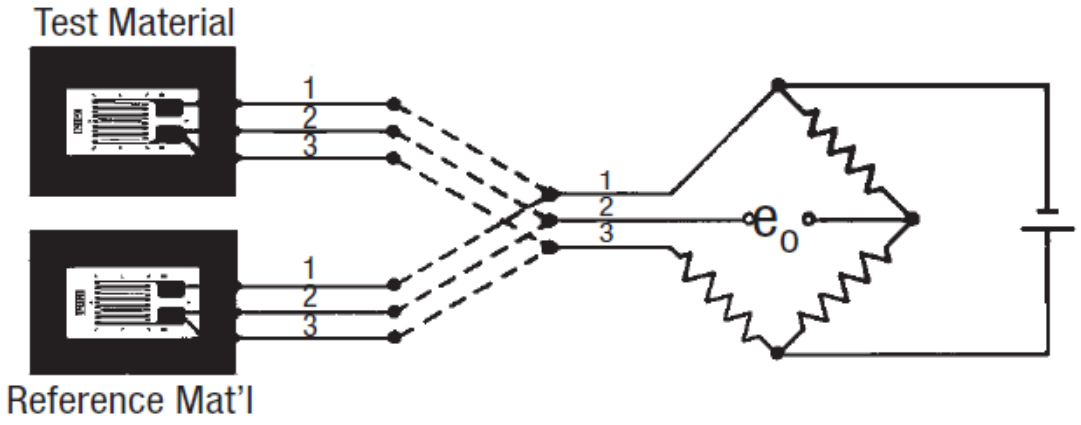

(a)

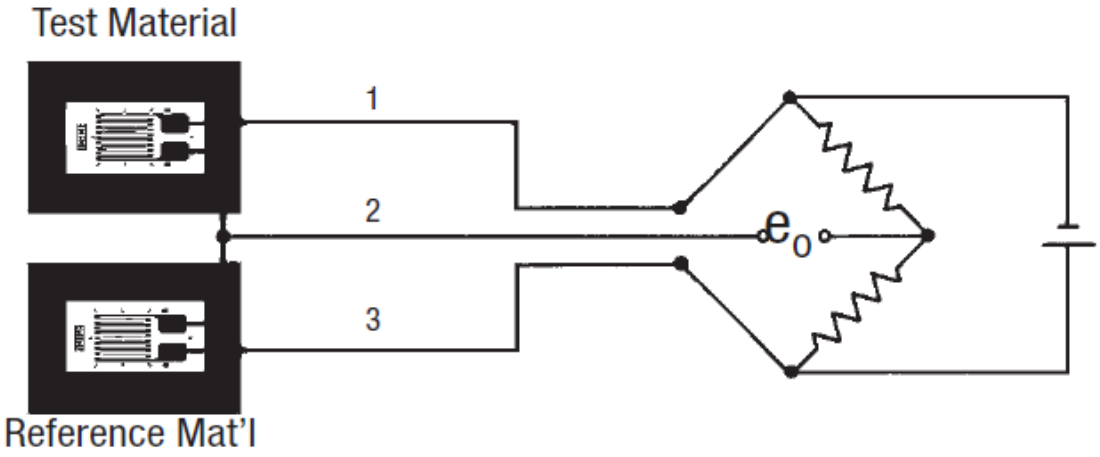

(b)

Figure 3.8. Strain gauge circuits for measuring linear thermal expansion coefficients: (a) separate quarter-bridge circuits, (upper diagram); (b) half-bridge circuit (lower diagram) (Poore et al., 1978).

3.3.6 Critical Control Points

Before performing actual measurements to determine the coefficient of expansion, the specimens and reference materials, with installed gauges, were stabilized by thermal cycling two to three times by heating to temperatures at least 5°C above the highest and below the lowest experimental temperatures. The purpose of thermal cycling was to relax and/or redistribute any residual stresses which might otherwise affect measurement during the test and impact on the repeatability of the measurement.

3.4 Measurement of Thermal Transport Properties

3.4.1 The Transient Plane Source (TPS) Technique

One of the most precise and convenient techniques for studying thermal transport properties, including thermal conductivity, thermal diffusivity and heat capacity per unit volume, is the Transient Plane Source (TPS) method (Gustafsson, 1991). The transient plane source consists of a spiral pattern of a thin layer of an electrically conducting material. The design of the TPS sensor has been made such that it can be brought into close thermal contact with the sample to be tested. A 10 μm thick nickel spiral is used as an element and is covered on both sides with a 25 μm thick insulating layer of Kapton. The TPS element used in this work, called a Hot Disk sensor, is shown in Figure 3.9 (a).

When performing a thermal transport measurement, one option is to choose two solid pieces of the same material and place the planar Hot Disk sensor such that each planar surface of sample material faces the sensor (e.g., as shown in Figure 3.9 (b) for rock sample pieces and Figure 3.10 (a), in which the thermal transport properties of stainless steel is being measured). Another option (which was used in this work) is to use one piece comprised of the material of interest (i.e., rock, in this research) and another piece comprised of polystyrene (e.g., as shown in Figure 3.10 (b)).

The Hot Disk sensor is used both as a heat source and as a dynamic temperature sensor. An electrical current is passed which is high enough to increase the temperature of the sensor from a fraction of a degree up to several degrees. At the same time, the resistance (temperature) increase is recorded as a function of time. The length of the current pulse is typically chosen to be sufficiently short so that the TPS element can be considered in contact with an infinite or semi-infinite solid throughout the transient recording. This means that the time of the transient recording

must be chosen so that those outer boundaries of the sample do not influence the temperature increase of the element to any measurable extent.

(a)

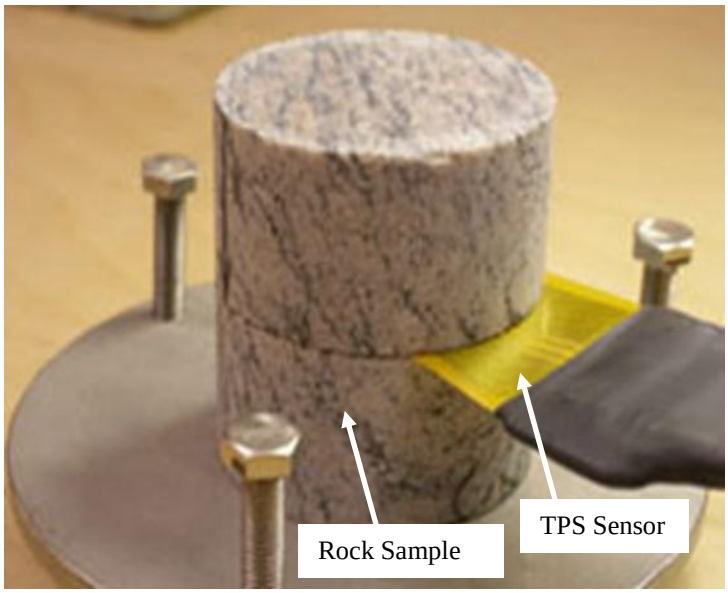

(b)

Figure 3.9. (a) Transient plane source sensor/Hot Disk Sensor, (b) Sensor is fitted between two pieces of the sample.

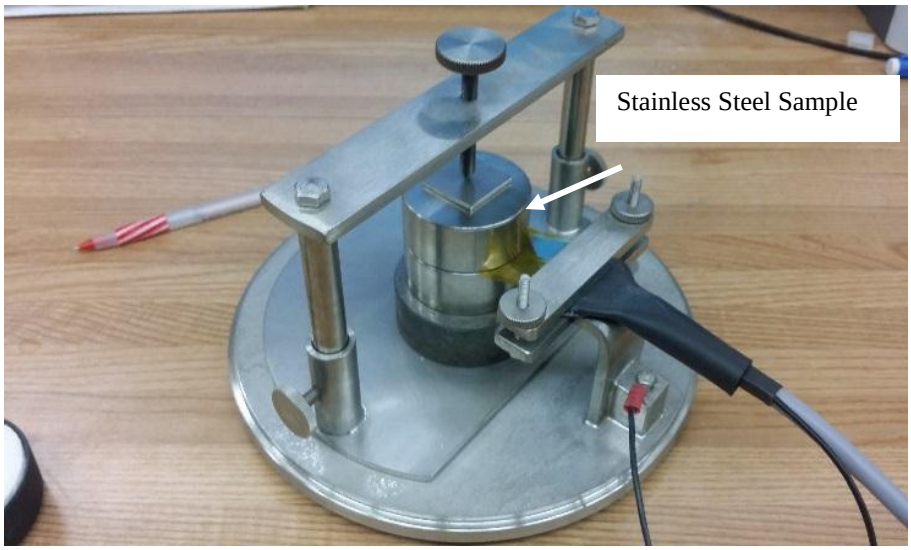

(a)

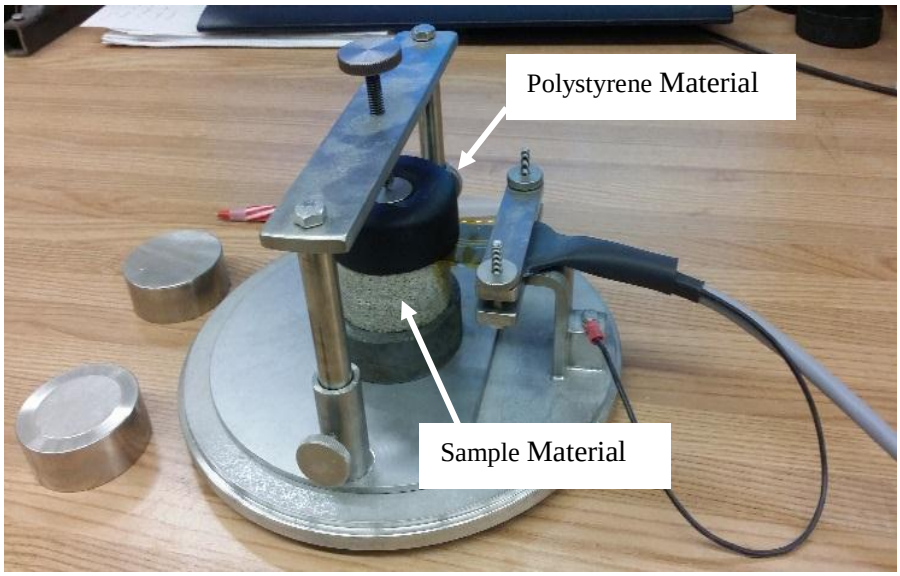

(b)

Figure 3.10. (a) The TPS sensor sandwiched between stainless steel sample pieces for calibration (b) The TPS sensor sandwiched between one of the rock sample and polystyrene material.

3.4.2 Calibration of Apparatus

The system was calibrated using a stainless steel sample provided by the Hot Disk system manufacturer. The thermal conductivity of this sample was measured three times using the TPS technique, and an average value of 14.4 $Wm^{-1}{}^{\circ}C^{-1}$ was obtained at room temperature. The reported value of stainless steel in the literature was found to be 14.8 $Wm^{-1}{}^{\circ}C^{-1}$ at room temperature. This indicated the discrepancy (i.e., 3 %) was less than the 5%, which was deemed acceptable by Gustafsson (1991).

3.4.3 Experimental Procedure

A brief description of procedures used is given here. For more details, refer to the Hot Disk Thermal Constant Analyzer manual (Hot Disk AB, 2014). Prior to performing the experiment, all the samples were dried in the oven at 105+5 $^{\circ}C$ for 2 hours, then they were allowed to cool at ambient temperature. Next, the TPS sensor was sandwiched between a sample of rock and the insulating material of polystyrene as shown in Figure 3.10 (b). A preselected constant current was supplied to the TPS element through the direct current (DC) power supply for a particular interval of time. The selected constant current and time interval are determined by considering sample dimensions, the type of sample material and the magnitude of the voltage applied so that the sample acts as a semi-infinite material for the TPS element. For these preselected parameters there was a list available in Hot Disk TPS 7 software (installed on the data acquisition computer) as initial recommendations, but the author did additional analyses to determine optimum values of the time interval and current for the samples tested in this work.

The voltage changes across the TPS sensor were recorded by a programmable digital multimeter which was connected to a computer. Two hundred data points were recorded per experiment, to obtain a smooth temperature-time curve from which occasional anomalous early-time or late-time readings were easily identified and removed manually. A typical temperature vs. time graph is shown in Figure 3.11.

The data from this graph was analyzed by the TPS program installed in the computer to interpret the thermal conductivity, specific heat (heat capacity per unit volume) and thermal diffusivity of the sample. The corresponding values of probing depth, temperature increment, and time correction are shown in Figure 3.12. The same procedure was performed five to six times for each

sample for varying time intervals and voltages (due to different dimensions of samples), and the thermal properties were calculated for each repetition (Figure 3.12). The values obtained were then averaged. The same procedure was adopted for all samples of Nisku and Calmar. The complete setup of TPS experiment technique is shown in Figure 3.13.

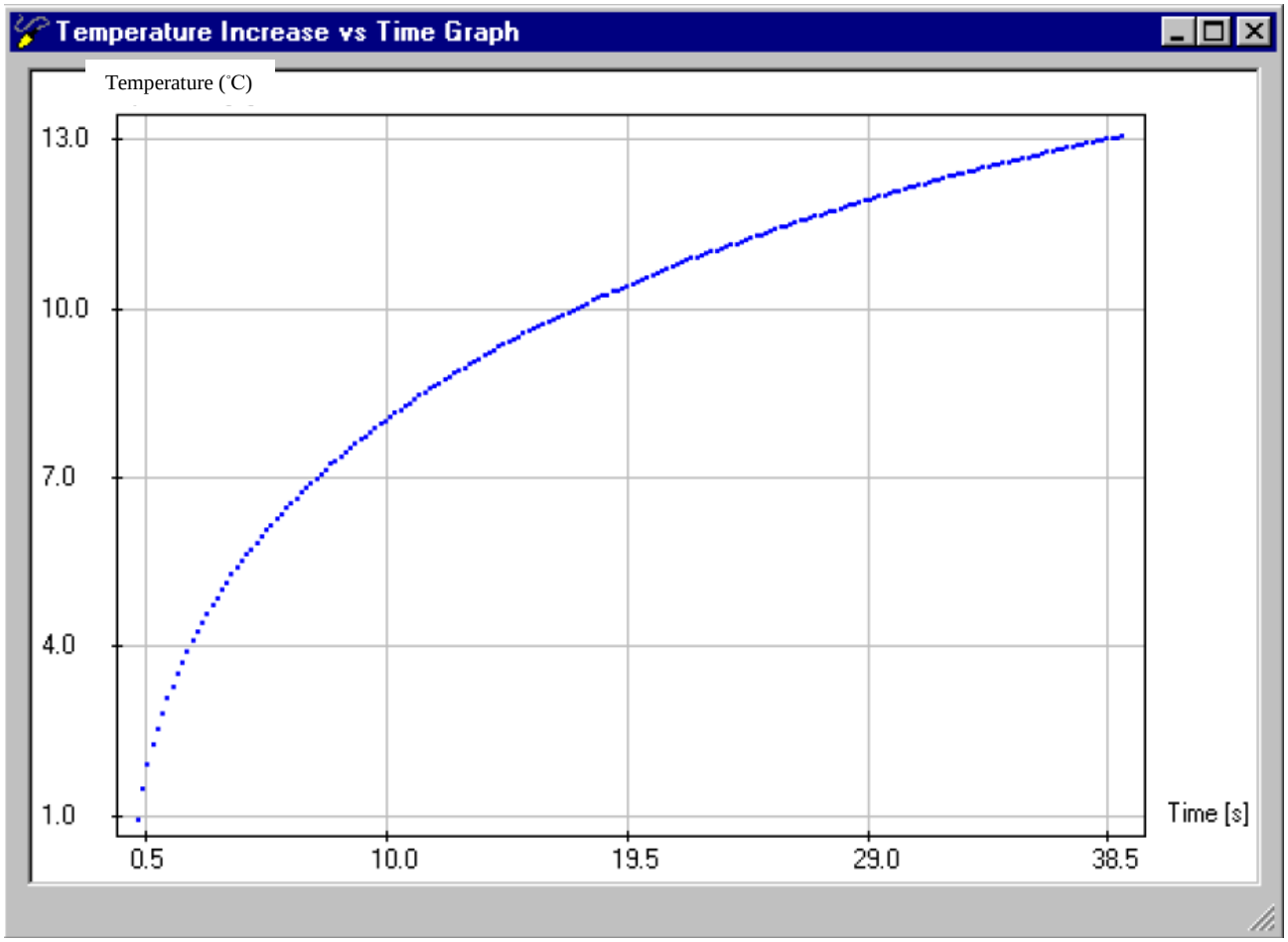

Figure 3.11. A typical temperature increase vs. time graph window of CMC3.

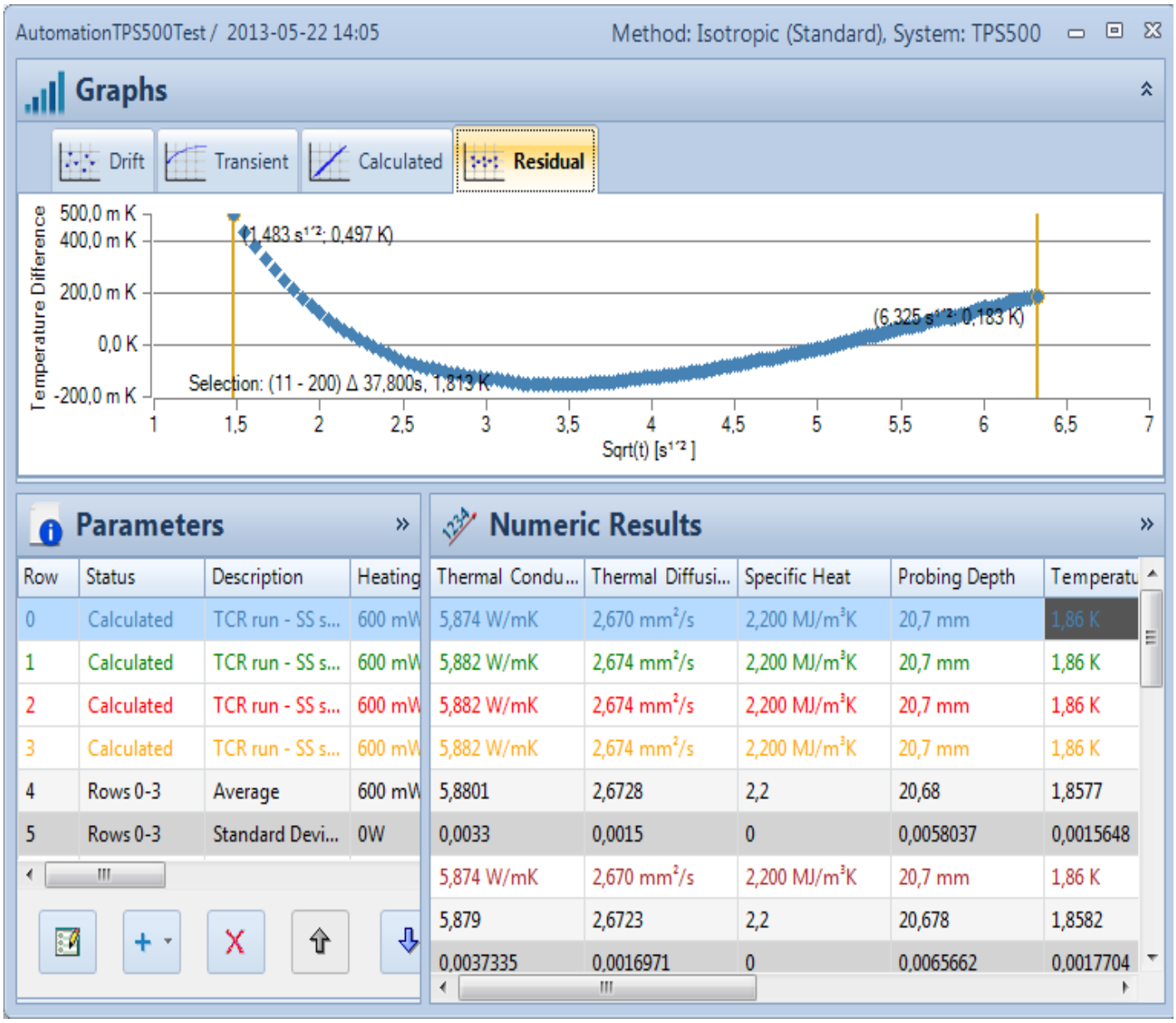

Figure 3.12. Data analysis and selection of data points and average results of thermal properties of CMR3.

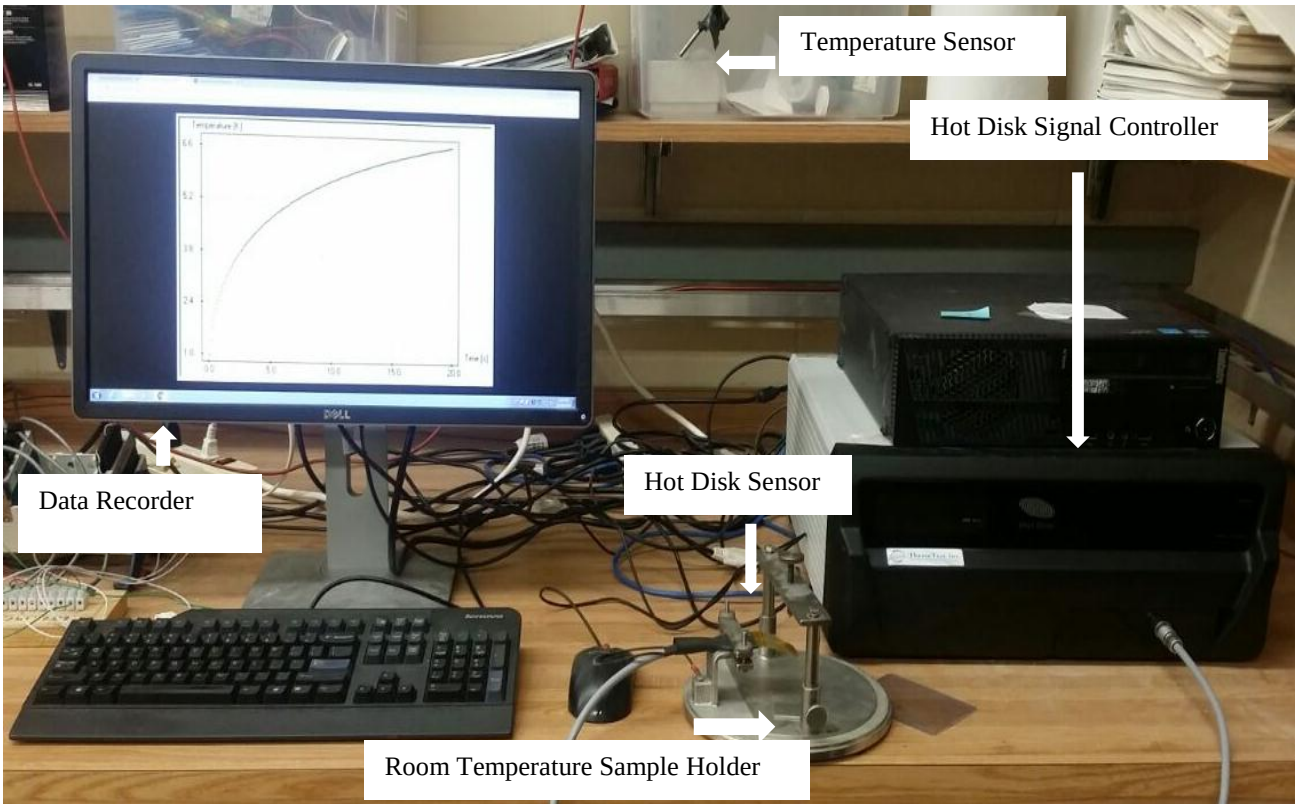

Figure 3.13. Hot Disk thermal contact analyzer (TPS) set up.

3.4.4 Precautions

The following precautions must be taken when using the experimental technique as described in section 3.4.1.

1. While performing the experiments, there should be a time interval of at least two hours between two successive measurements on any given sample so that the samples may revert to their equilibrium condition.
2. The electrical connections should be tight and the apparatus should not be disturbed during the transient recording.
3. The contact of the sample and the sensor should be as tight as possible using fingers.
4. It is important that the system be installed in a stable environment. The location should preferably be isothermal, free of vibrations and have a constant humidity.

5. The thermal measuring unit should be turned on 60 minutes before conducting an experiment.
6. It is advised that the diameter of the sample should be greater than twice that of the sensor and that the thickness of the sample should be greater than the radius of the sensor.

3.5 Matrix Reactivity Experiment

An experiment was designed and performed to measure the reactivity of the Calmar Formation caprock with CO_2-rich brine. A schematic diagram of the apparatus designed for this testing is shown in Figure 3.14, and the actual set up is shown in Figure 3.15.

3.5.1 Experimental Procedure

In this experiment, in situ conditions for temperature (70^oC) and pore fluid composition at the Project Pioneer site were replicated in a Parr model 4525 mixing reactor with a model 4848 controller. The fluid pressure inside the vessel was 10 MPa. This is lower than the in-situ pore pressure of 17 MPa but is greater than the critical pressure of CO_2 of 7.39 MPa. Thus, the free CO_2 present in the mixing reactor was a supercritical fluid, with a density and viscosity similar to in-situ values. No mechanical stress (confining pressure) was applied to the sample in this experiment.

As shown in Figure 3.14 and Figure 3.15, the fluid pressure was provided by syringe pump via an accumulator. This configuration protected the syringe pump (which is relatively expensive, compared to the accumulator) from the corrosive CO_2-rich brine. The CO_2 was provided by a 99.9 % pure CO_2 cylinder at a pressure of 800 psi (5.5 MPa). The pressure inside the vessel was then increased to 10 MPa by pumping brine into the vessel with Teledyne-Isco syringe pumps. The solubility of CO_2 in the brine, as a function of temperature and pressure, was estimated from Duan et al. (2006), and it was determined that sufficient CO_2 to saturate the brine was present in the vessel when this filling/pressurization method was used. A limited volume of free-phase CO_2 was likely present at the top of the mixing vessel throughout each experiment, but there was sufficient volume of CO_2-saturated brine and rock samples (discussed below) sat at the bottom of the vessel.

Inside the mixing vessel, two impellers were rotated in order to mix the brine and CO_2 (Figure 3.15). The rotation of these impellers was controlled by a magnetic motor which was run using the Parr 4848 controller. Two different pore water compositions were used in this experiment: one

representing native Nisku Formation brine before CO_2 injection, and another representing the predicted composition after 50 years of injection (Table 3.3). These brine compositions were taken from a WASP project report (Shevalier et al., 2010). The post-exposure brine showed a significant reduction in Ca^{+2}, a significant increase in Mg^{+2} and a minor increase in Cl^{-}. These changes are due to dolomite dissolution and calcite precipitation (Shevalier et al., 2010). No fluid samples were taken from the low-permeability Calmar Formation in the WASP project, so in this work, it was assumed that the Calmar Formation had the same brine composition as the Nisku Formation. These brines were prepared by mixing one liter of deionized water to the concentration of the compounds listed in Table 3.4.

One Calmar core sample (CMR3) was used for this testing and was cut into three almost equal size of pieces of approximately 2.5-5 cm in length, 1.5 cm in width, and 2.5 cm in height (Figure 3.16). One of the three pieces was used as a baseline, or reference sample piece, and the other two were exposed to the two aforementioned CO_2-rich brines in two separate experiments in which each sample was placed in the vessel for a period of two weeks. The three samples were then compared to each other by their visual surface textures, porosities and EDS analysis responses, in order to gain insights into the role of different minerals in reactions with the brine. This was done to help understand possible permeability changes with time upon exposure to CO_2-rich brine.

3.5.2 Precautions

1. Every effort was made to control the temperature and pressure changes during the experiment.
2. Possible leakage sources were removed because the testing system is extremely sensitive to it.

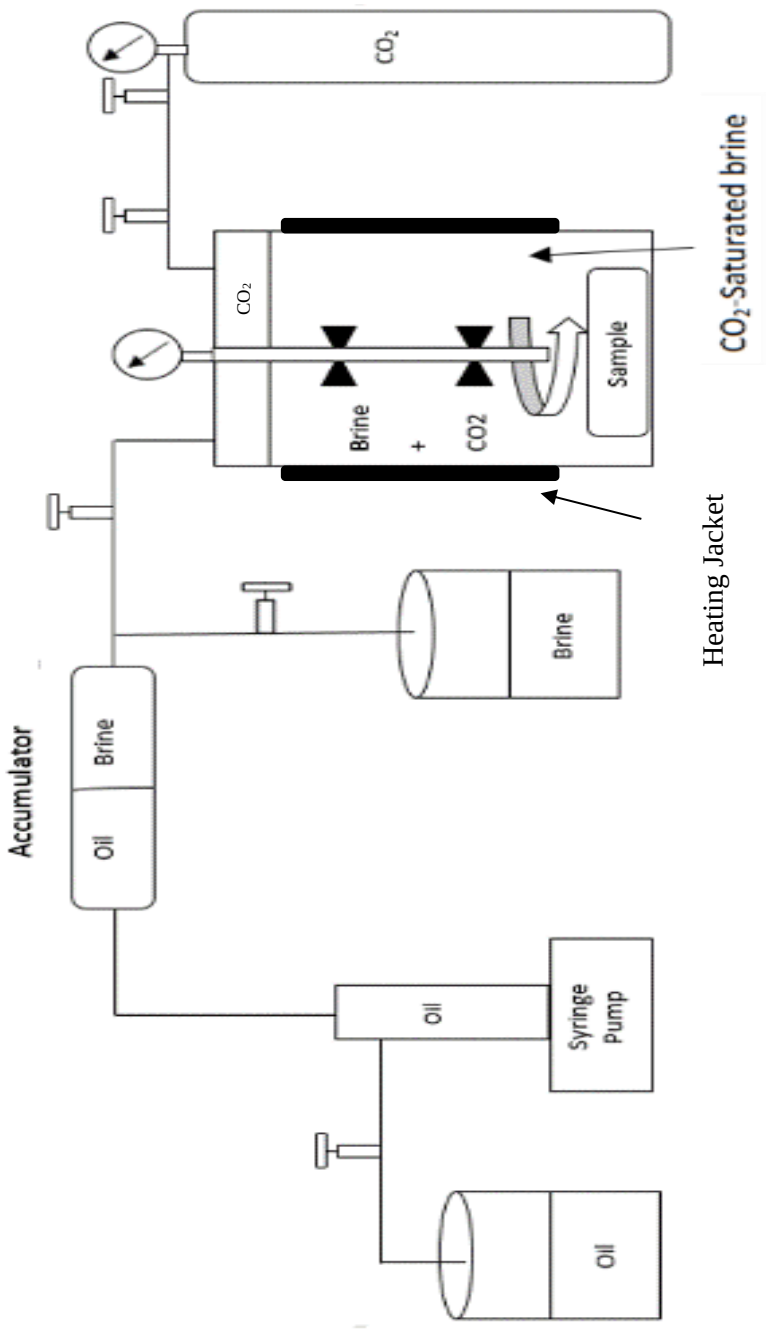

Figure 3.14. Schematic diagram of matrix reactivity testing apparatus.

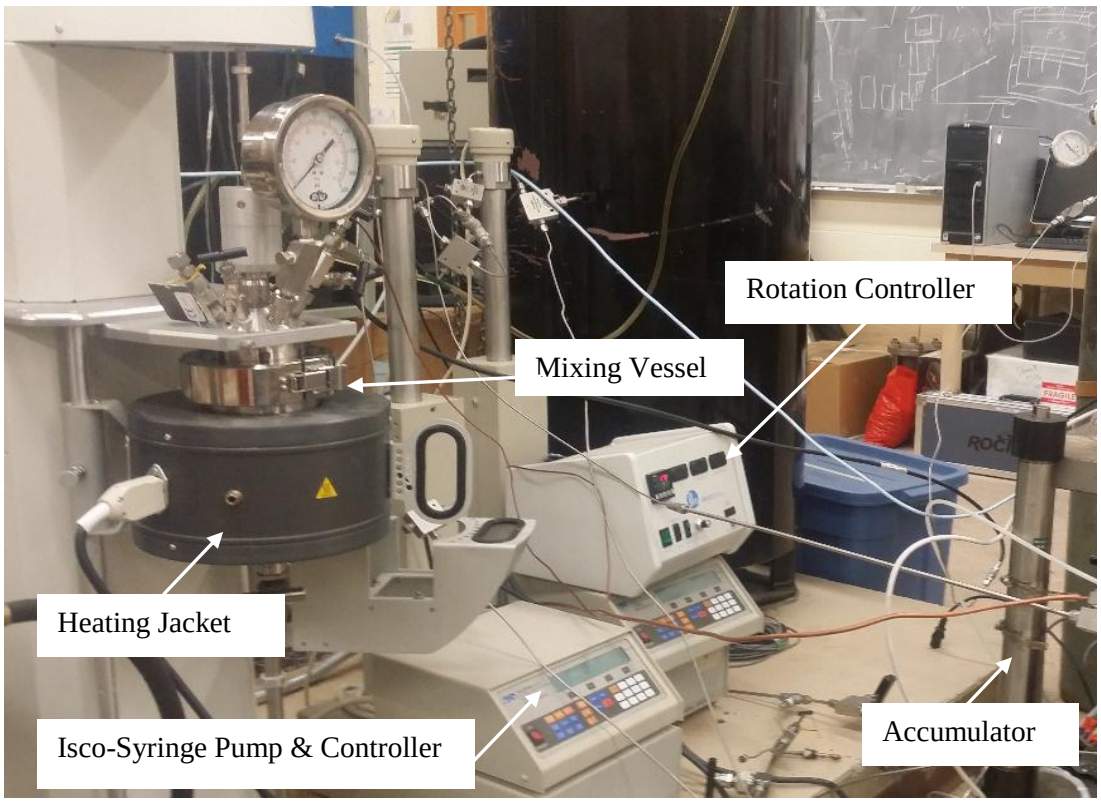

Figure 3.15. Actual set up of matrix reactivity testing apparatus.

Table 3.3. Water chemistry of : (I) Nisku Formation fluid samples obtained from well 100/11-29-045-02W5 in 2008; and (II) Nisku pore water chemistry after 50 years of CO_2 injection, as predicted by (Shevalier et al., 2010).

Ion	Fluid I concentration (mg/L)	Fluid II concentration (mg/L)	Difference (II – I) (mg/L)
Na^{+}	55150	55150	0
Ca^{+2}	15430	753	-14677
K^{+}	3720	3720	0
Mg^{+2}	2129	13736	+11607
Sr^{+2}	884	884	0
Cl^{-}	117743	130559	+12816
SO_4^{-2}	470	470	0

Table 3.4. Salt masses used for preparing representative pore fluids: Initial in situ brine (I); and (II) brine after 50 years of CO_2 injection in the Nisku Formation.

Compound	Fluid I mass (g)	Fluid II mass (g)	Difference (II – I) (g)
$NaHCO_3$	0.69	0.69	0
Na_2SO_4	0.70	0.70	0
NaCl	139.22	139.22	0
$CaCl_2$	42.82	2.09	-40.73
KCl	7.11	7.11	0
$MgCl_2.6H_2O$	18.01	116.18	+98.18
$SrCl_2.6H_2O$	2.69	2.69	0

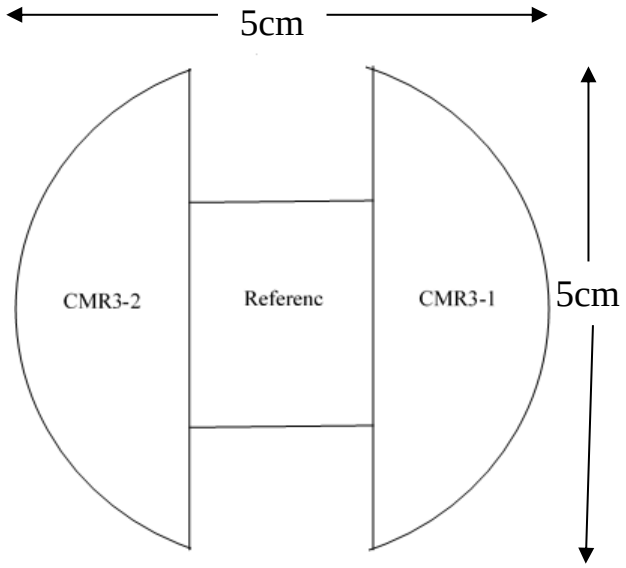

Figure 3.16. Schematic of three pieces of CMR3. Approximately 5 cm, 1.5 cm and 2.5 cm length, width and height, respectively for CMR3-1 and CMR3-2, whereas the reference sample has 2.5 cm, 1.5 cm and 2.5 cm length, width and height, respectively.

3.6 Permeability Experiment Including Fluid Sampling

A new experimental setup was designed (Figure 3.17 and Figure 3.18) to measure and investigate the permeability of intact and fractured caprock samples. The first sample tested (CMR2), was an intact core piece of Calmar Formation that was measured using the pressure pulse decay method (Brace et al., 1968). The second and third samples (CMR1 and CMR4) were fractured in the laboratory prior to testing, to investigate fractured permeability during the steady-state flow of CO_2-acidified brine. The brines used for these tests are given in Table 3.3. Brine I was used for the test on CMR4, and brine II was used for CMR1. This was done to simulate conditions when initial CO_2 reacts at the base of caprock during the initial stage of injection (brine I, sample CMR4), and when brine composition has changed after 50 years of residence time within the Nisku Formation (brine II, sample CMR1). The temperature, confining pressure and pore pressure used for these experiments were 70 °C, 40 MPa and 17 MPa (average) respectively. These values were used because they are representative of in-situ conditions at the Project Pioneer site.

3.6.1 Experimental Setup

The experimental setup (Figure 3.17) used an extension of the Matrix Reactivity apparatus, with the addition of a purpose-built hydrostatic pressure cell/vessel which was used to subject the sample to confining pressure provided by a Quizix Q6110 syringe pump. A temperature of approximately 70°C was successfully maintained inside the pressure cell by wrapping it in an adjustable heating jacket by Duda Energy (Figure 3.19) wrapped around it. Two Teledyne-Isco 260D syringe pumps (referred to as “syringe pumps”) were used through pressure accumulators to provide pressurized pore fluid to the upstream and downstream flow lines (Figure 3.18). The syringe pumps were connected to the pressure cell using high-pressure, 1/8” outer-diameter stainless steel tubing, rated for a pressure of 68.9 MPa.

The experiment setup was designed to have either a constant flow rate or a transient/constant pressure gradient with a predetermined upper limit of pressure for the upstream pore pressure. This upper limit was set to ensure that the pore pressure did not exceed the confining pressure of 40 MPa. It is important to note that the apparatus was designed and operated such that the CO_2-rich brine would remain pressurized at all times, in order to prevent the CO_2 from coming out of solution. Specifically, the average pressure in the sample was maintained close to 17.5 MPa, with a small differential pressure (~ 1MPa) applied to cause flow.

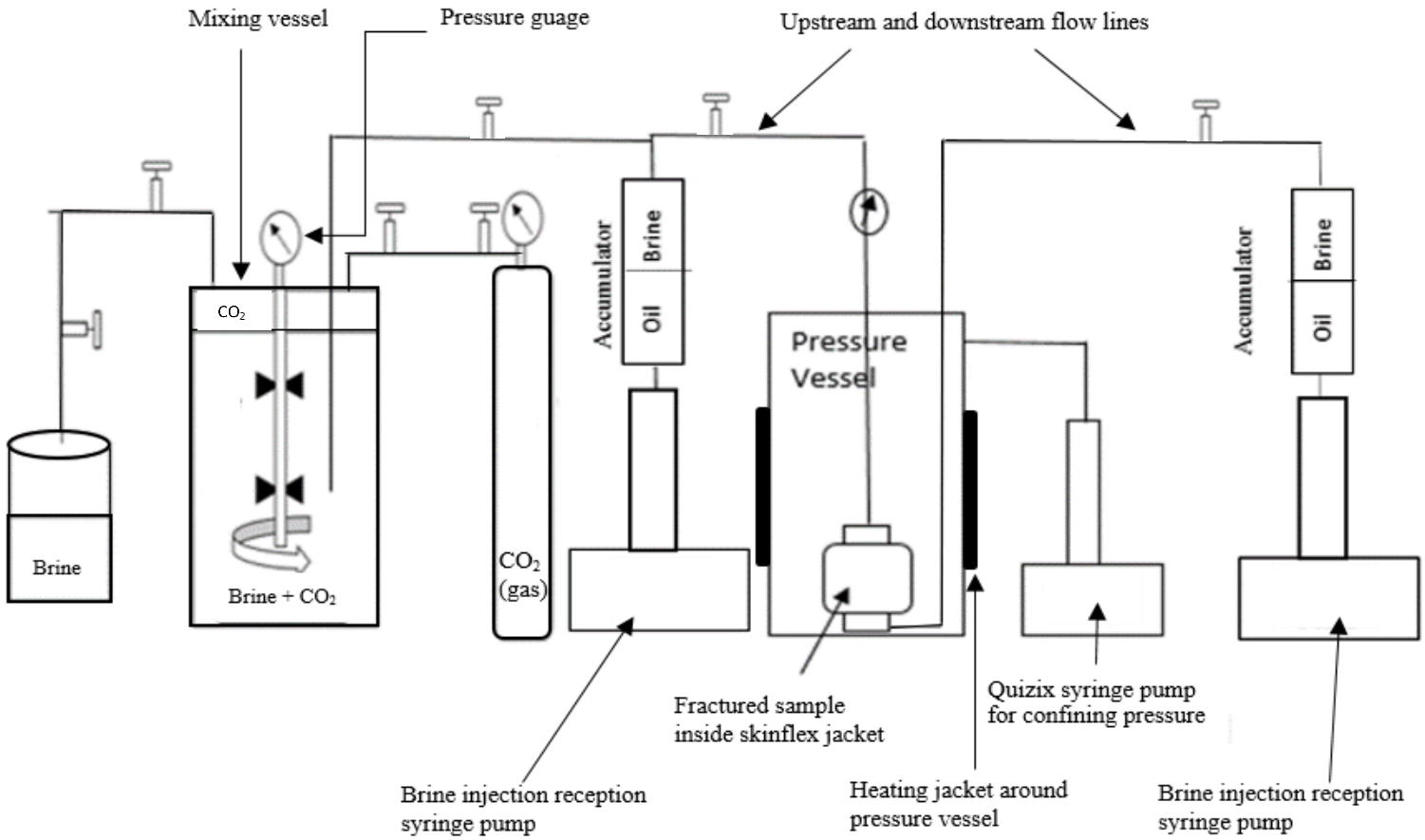

Figure 3.17. Schematic diagram of permeability testing apparatus.

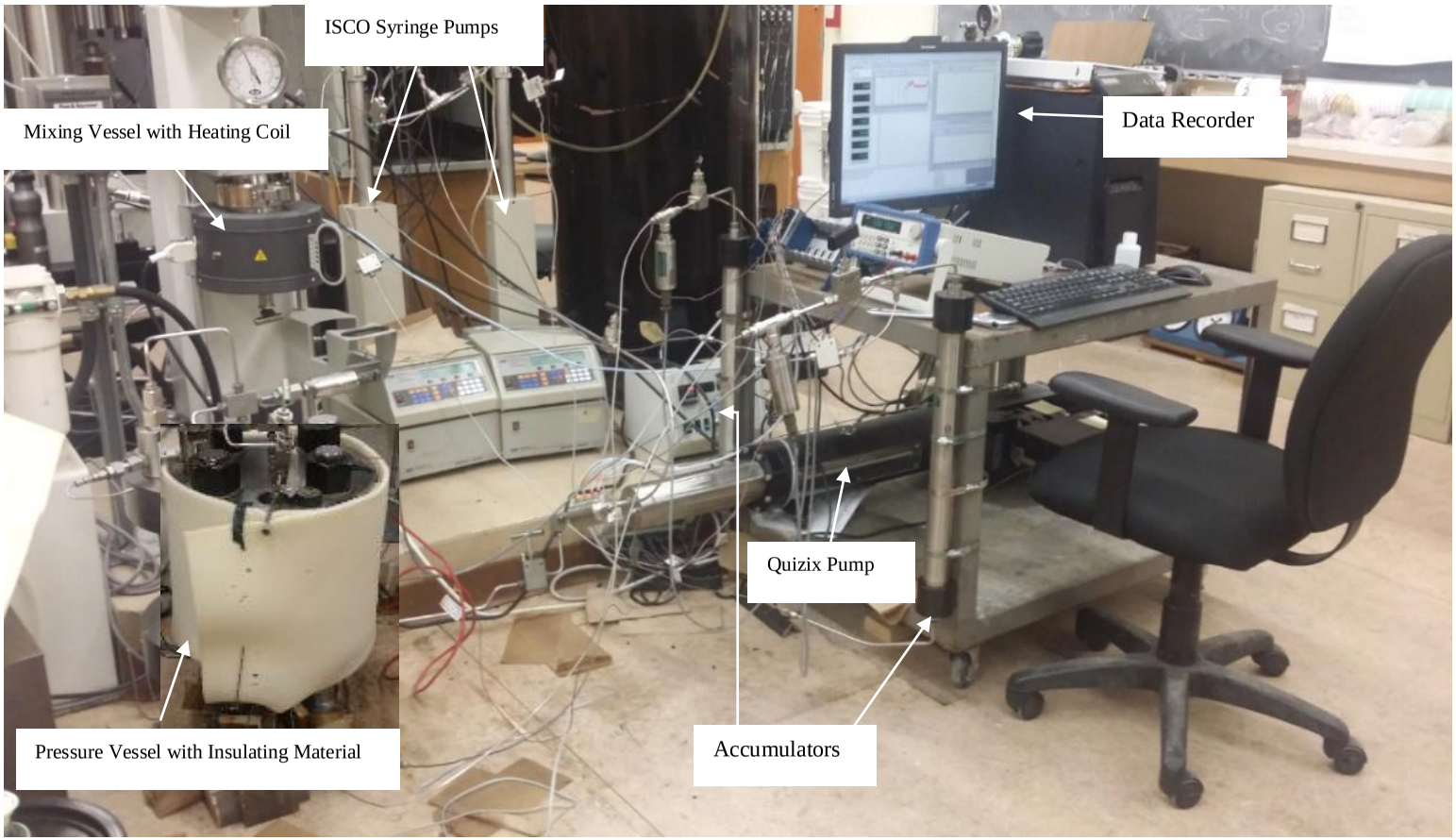

Figure 3.18. Actual Set-up of permeability testing apparatus.

Figure 3.19. Heating jacket (Duda Energy, Alabama USA) for the high-pressure vessel to keep the required temperature.

A key aspect of the experimental system was the selection of a sealing jacket that would surround the sample, porous Disks, and platens. The Disk and platens were required to provide a tight seal that prevented the penetration of confining oil into the sample and leakage of pore fluid from one end to the other along the sample-jacket interface. Lacking of published data prescribing the material to use as the membrane for experiments involving CO_2-rich brines, SkinFlex III ("SkinFlex") was used in this research (Figure 3.20), based on the advice of technical staff in the University of Saskatchewan Rock Mechanics Laboratory. The upstream and downstream "reservoirs" were created by the connection of accumulators to the stainless steel tubing,

associated fittings, and flow control and measurement devices to ports on the base of the pressure cell. The ports were internally plumbed so as to allow hydraulic communication with the ends of the sample. Each reservoir also included a pressure transducer connected to it via a T-junction fitting inserted in-line with the stainless steel tubing.

In the case of measuring intact caprock permeability using the pulse decay method, the total volume of each reservoir was minimized to yield faster pressure pulse decay during a permeability test. However, a downside of small reservoir volumes is an acute sensitivity to leakage. Also, the volumes of the upstream and downstream reservoirs relative to the pore volume of the sample play a major role in determining the appropriate approach to interpret the pulse decay test data.

For the fractured samples, permeability was measured continuously over the course of days to weeks. Pressures were set at constant values, with a slightly higher pressure at the upstream end of the sample, and flow rates were recorded. A pressure difference was selected in these experiments to increase the opportunity for the brine-rock interaction inside the fractured rock surface. When the upstream accumulator-pump became empty, the flow direction was reversed, and so on, until the end of the experiment. It was anticipated that permeability would increase initially, as the fluid reacts with the fracture surfaces. It was also expected that the fluid composition would change. In order to test the latter theory, fluid samples were taken periodically and sent to a geochemistry laboratory at the University of Calgary for compositional analysis. The fluid samples were intended to provide an indication of what kind of chemical reactions occurred, hence providing information on how and what factors played a role in permeability change.

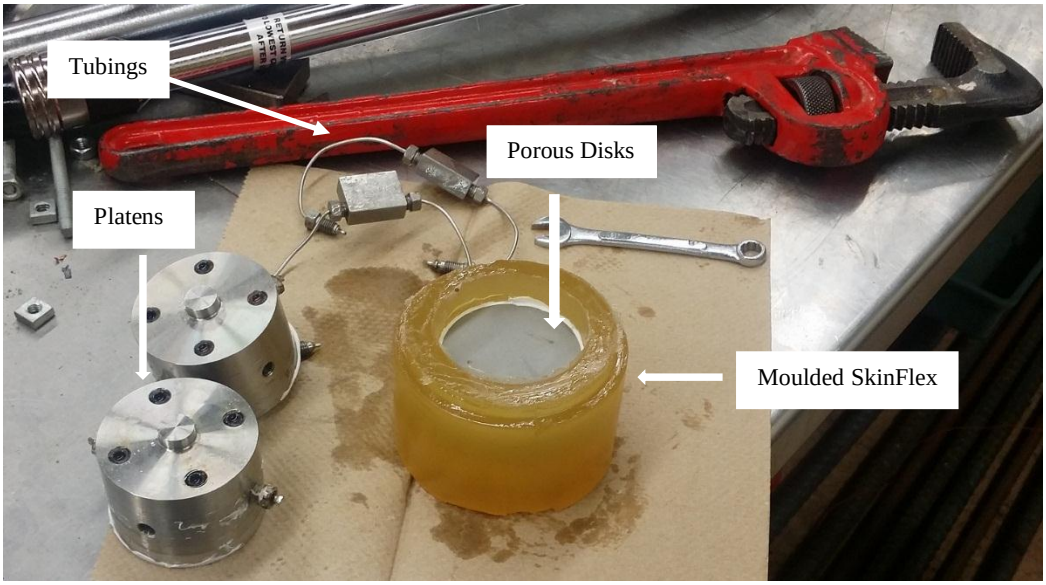

(a)

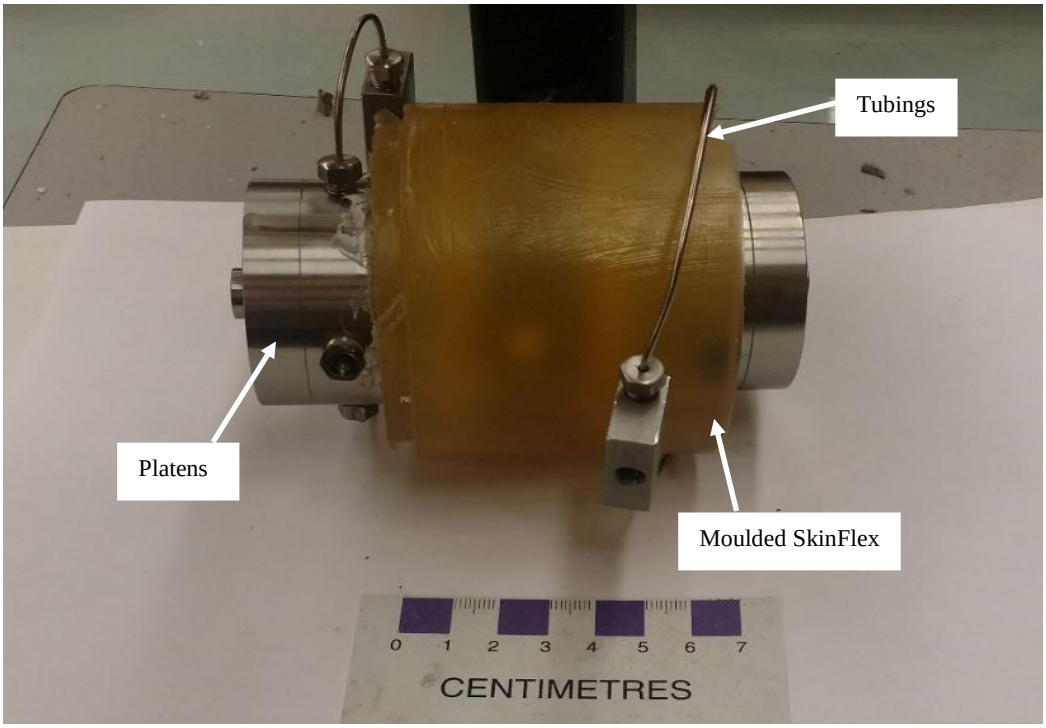

(b)

Figure 3.20. Sample, porous disks and platens inside moulded SkinFlex jacket and connecting tubes (a) during assembly, and (b) after assembly (prior to insertion into the pressure vessel).

3.6.2 Fracturing Technique for Samples CMR1 and CMR4

The following steps were followed to prepare fractured samples for permeability testing:

1. To fracture each sample and to encourage a single fracture to develop running parallel to the core axis, a groove along one side of the core was made. This was done using a circular rock saw, with a diamond-blade that was 2.3 mm in width. The depth of the cut was manually controlled and made as shallow as possible (≤ 1 mm depth).
2. Load was applied by modifying the procedures used for a Brazilian splitting tensile strength test (ASTM, 2008). For this work, the load was applied using one flat surface (on bottom) and a 4 mm diameter steel rod (on top). The sample was oriented in such a way that the groove was on top so that the steel rod could be placed in the groove (Figure 3.21 (a) and (b)). As such, the top platen's load was localized within the groove. The bottom loading method followed standard Brazilian procedure (i.e., the lower portion of the sample sat on a sheet of plywood, which in turn sat directly on the bottom loading platen) (ASTM, 2008).
3. Rather than using a servo-controlled load frame, a manually-operate load frame was used (a Carver Press). This made it easier for the operator to observe the sample up close without any mechanical background noise so that he could hear the fracture develop and stop loading immediately. Figure 3.22 shows sample CMR1 before and after fracturing, respectively.

(a)

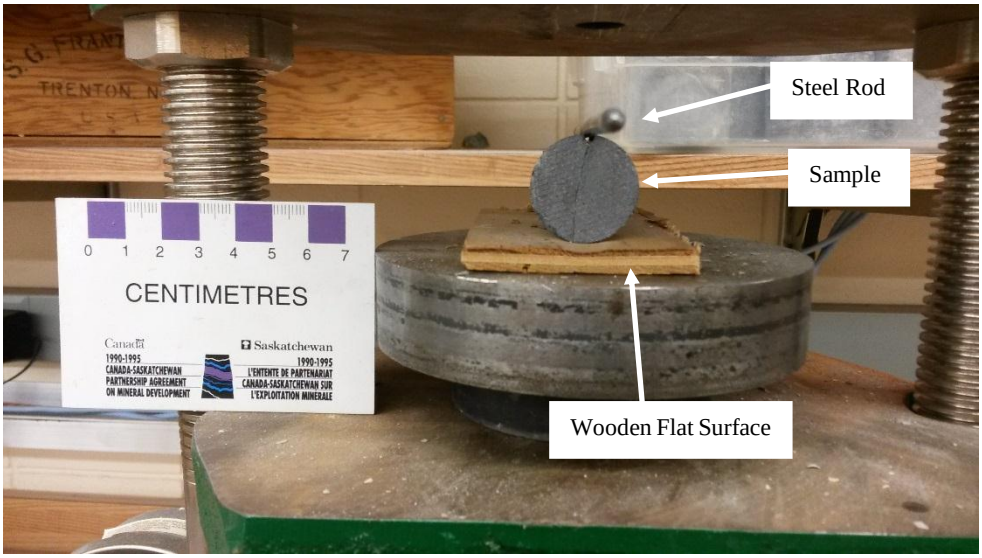

(b)

Figure 3.21. (a) A complete picture of Carver press with sample and rod in the groove and (b) close up view of a sample with groove and steel rod used to induce a fracture.

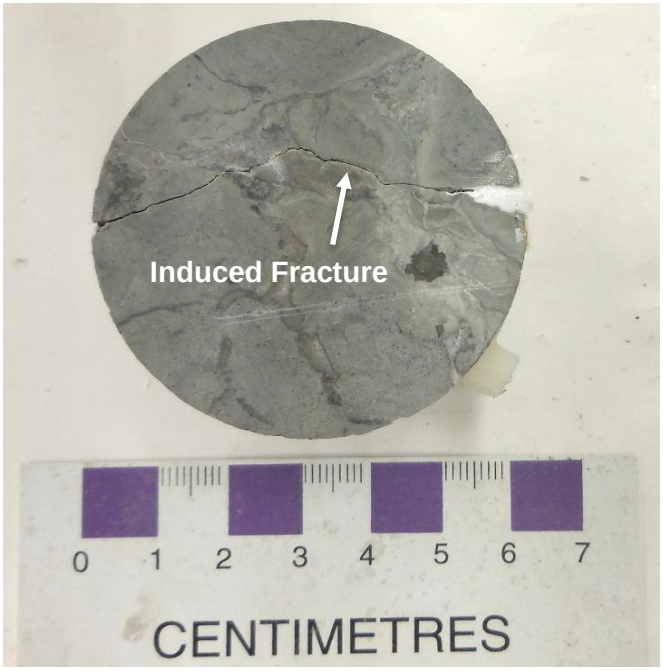

(a)

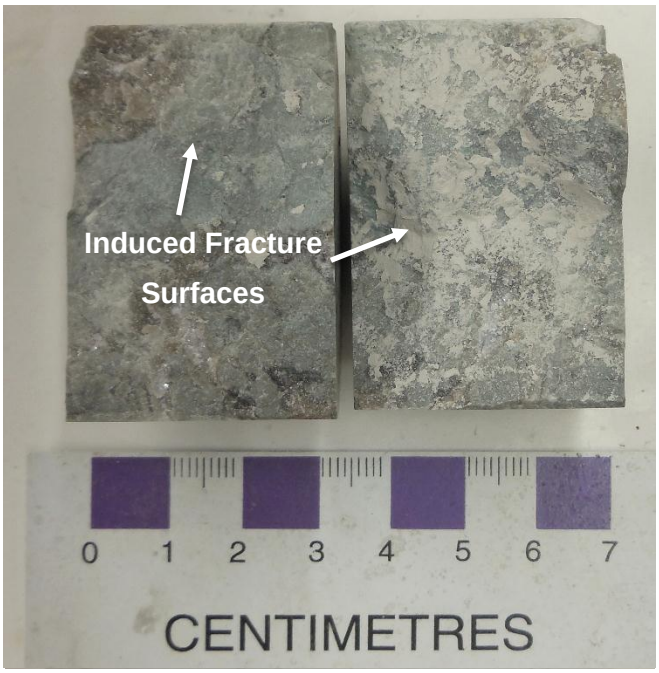

(b)

Figure 3.22. (a) Sample CMR1 with a fracture that was induced using a modified Brazilian splitting test. (b) Two opposing faces of the fractured sample. (Note: White substance at the right edge of the fracture in (a) is silicone sealant that was used to plug a void created where a corner of the fracture broke off).

3.6.3 Sample Preparation for All Samples Inserted into pressure Vessel

1. A mould was prepared by spreading vacuum grease inside it. The grease was spread as evenly as possible because clumps could lead to holes or thin spots in the Skinflex.
2. Length, diameter, and weight of the sample were measured.
3. The sample was placed between platens and sintered stainless steel porous plates.
4. The mould was carefully secured around the sample ensuring that no vacuum grease got on the sample. If that happened, then SkinFlex would not stick to the sample.
5. SkinFlex preparation:
    a. Measured one part of SkinFlex A to two parts of SkinFlex B.
    b. Mixed well for several minutes. Inadequate mixing would not allow the SkinFlex to set properly.
    c. Placed the mixed SkinFlex in a vacuum chamber to remove air bubbles.
    d. Poured SkinFlex into the mold.
    e. Let SkinFlex set overnight or for approximately 24 hours.
6. Placed sample into the pressure cell.
7. Adjusted the pressure cell cover and filled the cell with oil; tightened the bolts and screws of the cell.
8. Installed the pressure transducers and safety valve for the pressure vessel and connected the transducers to the computer through the control module.
9. Wrapped heating jacket around the pressure cell and inserted the temperature sensor between the heating jacket and outer surface of pressure cell and then connected the output of the temperature sensor to the computer through a data acquisition module.
10. Opened the valve between the Quizix pump and pressure cell and applied the confining pressure of 40 MPa using the Quizix pump.

11. Mixed the brine and CO_2 in the Parr mixing vessel as discussed in the Matrix Reactivity experiment; adjusted stirrer speed through its regulator and allowed at least 2 hours for CO_2 and brine to mix properly.

12. Filled the upstream accumulator (from the cell-connected end) with brine-CO_2 solution from the Parr mixing vessel, and filled the downstream accumulator (from the pump-connected end) with hydraulic oil. , while keeping the valve between each accumulator and pressure cell closed. For both accumulators, one end was connected to a Teledyne-Isco syringe pump. The volume in each Teledyne Isco syringe pump was measured and recorded by computer via an analog to digital converter (A-D converter) provided by Teledyne Isco. The A-D converter provided a signal ranging from 10 V to 0 V as volume changes from empty to full, respectively. As needed, oil could be pumped out of a syringe pump to displace brine out of its connected accumulator, or oil could be taken into the pump to allow brine to flow into its connected accumulator.

13. Connected pressure transducers to the upstream and downstream syringe pumps, and connected to a computer via data acquisition module to record pressure readings.

14. With the upstream accumulator filled with brine, equal pressures of 17.5 MPa were applied to both syringe pumps for a couple of hours until the system stabilized.

15. Data recording was started on the computer using a specially designed program created by the author and lab technician using the DaisyLab software.

3.6.4 Pressure Pulse Decay Test Method - for Intact Sample CMR2

Samples CMR2 was tested using a pressure pulse decay method as follows:

16. An increment of approximately 1 MPa pressure was applied to the upstream reservoir by pumping a small volume of hydraulic oil from the upstream syringe pump into the upstream accumulator, thus displacing brine from the accumulator into the upstream reservoir . All valves were closed and the pulse decay was monitored.

17. Monitored upstream and downstream pressure until they became ~ equal.

18. Stopped the experiment and collected the data for further analyses.

3.6.5 Steady-State Permeability Measurement-Procedure for Fractured Samples CMR1 and CMR4

Samples CMR1 and CMR4 were fractured as per section 3.7.2. Steady-state permeability measurements were taken as follows:

16. The pressure at the up-stream end of the sample was increased from 18-19.5 MPa while the 17.5 MPa was maintained at the downstream end of the sample by setting the desired pressure values in the syringe pumps and opening the valves between the accumulators and the pressure cell. This started the flow through the sample.
17. The differential pressure was increased or decreased across the sample to increase or decrease the flow rate in order to provide enough time for the brine to react with the fractured surface.
18. When the upstream accumulator-pump became empty, the flow direction was reversed, and so on until the end of the experiment.
19. Fluid samples were taken after every flow-through cycle from the fractured sample for chemical analysis. The effluent sampling protocol used for this step is in given in Appendix F.
20. To stop the experiment after the end of fracture permeability measurement, the computer data recording was first stopped, then data were saved and the equipment disassembled in reverse order following the steps mentioned above.

3.6.6 Precautions

1. When conducting the test every effort was made to control the temperature and pressure changes.
2. Possible leaks were removed because the testing system is extremely sensitive to leakage.

3.7 Fracture Surface Profiling

The fracture surfaces of samples CMR1 and CMR4 were profiled using a laser optical profiler mounted on a two-dimensional computer controlled traverse system on a horizontal plane (Figure 3.23) at the Hydrotechnical Laboratory of the University of Saskatchewan. This profiling was done on the samples before and after permeability testing to assess changes in surface morphology resulting from exposure to CO_2-rich brine.

3.7.1 Experimental Procedure:

The laser optical profiler used an optoNCDT 1700-500 model displacement and position sensor, and the accuracy of the sensor was 0.001mm. The traverse arrangement used a custom program designed in LabVIEW 5.5 from National Instruments. The operating distance of the profiler from the rock surface was 200 mm to 700 mm. Therefore each sample was placed within this range. Two motors were attached in the traverse arrangement to move the profiler in the *x* and *y*-direction respectively in the horizontal plane to gather the data using a 2 mm by 2 mm grid.

The LabVIEW program saved data collected from the profilometer in text file format. For each surface measurement, a single text file was created. The text files had elevations against the *x, y* positions of the grid points on the surface. However, the data saved in the text files were still "raw" and required to be processed "spatially." ArcGIS 10.2.2 software was utilized for the spatial processing of the collected data.

Initially, the text files acquired from laser profiling were exported into ArcGIS. The text files were then transformed to "Shapefiles", the file format in ArcGIS for examining spatial data. The shapefiles characterized each data point as a geometric point having spatial information (i.e., *x, y* and *z* value). However, the elevation or *z* value was measured from the base of the laser profiler to the sample surface points. A TIN file is essentially a digital representation of surface morphology, and each vertex of the TIN characterizes the actual point from which the TIN is generated. Therefore, the actual elevation data of the measured points are kept in TIN vertexes. The final output results, which show the comparison on the two surfaces (before and after flow through experiment), was obtained by combining both point shape files. For exact matching of the positions of the two shape files, four pegs were used around the sample as reference markers.

3.7.2 Precaution

1. The samples should be placed each time inside operating range of the profiler.
2. For accurate output results, comparing the surfaces before and after the permeability experiment, the four pegs of the two shape files need to be precisely aligned.

3.8 Summary

At the end of the testing, samples CMR1 to CMR4 were broken into small pieces and samples NSK1 to NSK5 were intact. All samples were returned to Earth Sciences laboratory, University of Calgary, Alberta, Canada. The results and discussion of all performed tests are given in chapter 4.

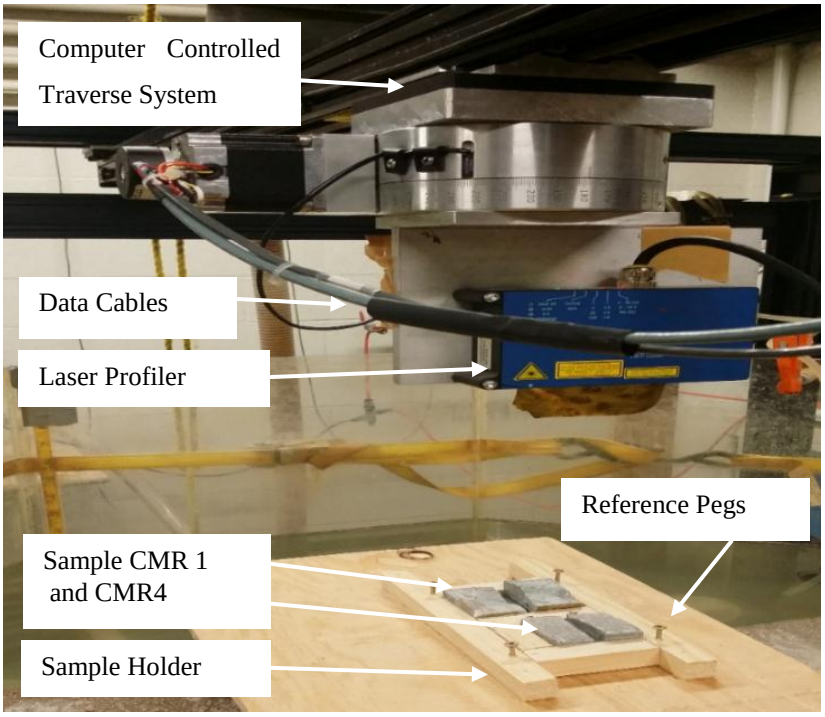

(a)

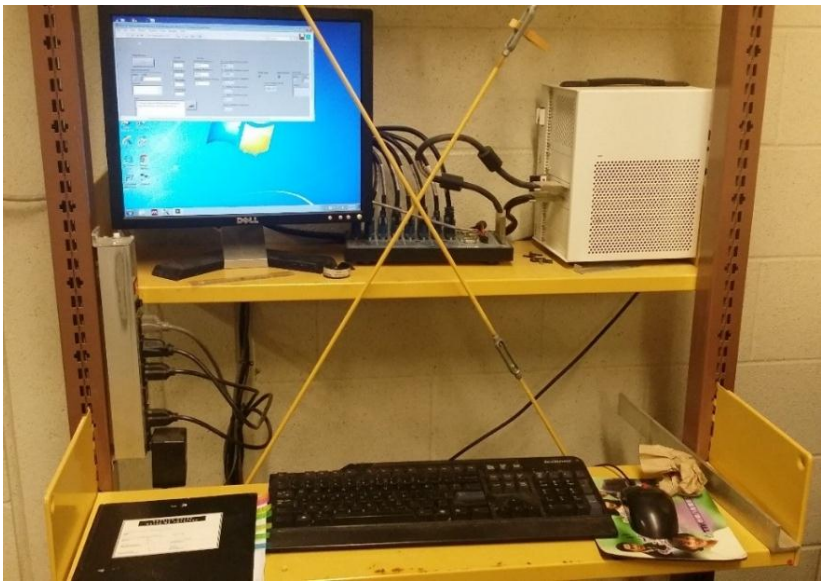

(b)

Figure 3.23. (a) Major components of profilometer and (b) data acquisition system.

4. RESULTS AND DISCUSSION

4.1 Quantitative Mineralogy

Results for the twelve samples analyzed with quantitative mineralogy were presented in Chapter 3 (Table 3.2). The average composition of the four Calmar Formation samples analyzed is: 34% quartz, 22% calcite, and 12% dolomite. Together, these minerals comprise greater than 60% of each bulk sample, with the remaining minerals consisting of a mixture of K-feldspar, clay, and pyrite. With the exception of samples NSK8 and NSK9, the Nisku samples were predominantly composed of dolomite (79.7% to 91.6%), with calcite as the second most abundant mineral (4.7 to 15.2%) present and minor amounts (a fraction of a percent to roughly 2%) of all other minerals analyzed. Nisku Sample NSK8 was found to contain 52.9% dolomite, 27.6% detrital quartz, and small amounts of feldspars (1.7% albite + 5.1% K-spar), mica (4.4%), calcite (3.8%) and pyrite (1.3%). Sample NSK9 was predominantly comprised of anhydrite (47.1%) and dolomite (44.4%).

Dominant matrix mineralogies of the Calmar samples, to the extent determinable from the limited sample sizes (~ 1.5 cm) examined, are calcareous dolomitic mudstones and dolostone. Pore types observed in the Calmar samples are matrix-hosted intercrystalline types. Their characteristics are as follows:

- Intercrystalline matrix porosity (mudstones) [0.2 to 1.0 microns] represents the majority of pores observed in the mudstone samples. Matrix-hosted pores are intercrystalline voids between matrix particles, such as clay flakes and cement microcrystals.
- Intercrystalline porosity (dolostone) [up to 10.0 microns] are relatively rare in the sample studied, planar gaps between interlocking dolomite crystals. These pores are isolated, widely dispersed, and are not significantly connected (Terratek, 2011).

4.2 Thermal Properties

Data for linear thermal expansion coefficient of Nisku 1 (NSK1) core plug is given in Table 4.1 and its values are calculated using equation 3.6 as follows:

$$\alpha_S - \alpha_R = (\varepsilon_1 - \varepsilon_2) / \Delta T \qquad (3.6)$$

The exemplary values used are highlighted in Table 4.1.

$$\alpha = \alpha_S - \alpha_{R = (\varepsilon_1 - \varepsilon_2)} / \Delta T$$

$$\alpha = (\varepsilon_1 - \varepsilon_2) / \Delta T$$

$$\alpha_{T\text{-axial}} = (89 - 43\ \mu\xi)/ (44.87 - 33.47\ ^{\circ}C)$$

$$\alpha_{T\text{-axial}} = 4.04\ \mu\xi\ ^{\circ}C^{-1}$$

Similar calculations were performed on all values and the average values of axial and radial linear thermal expansions are 4.02 (μξ/°C) and 2.73 (μξ/°C) respectively. This gives a final average linear thermal expansion coefficient of 3.37 (μξ/°C) in both directions. All samples tested were drilled vertically through rock possessing horizontal bedding; as such, the axial thermal expansion coefficients represent bedding-normal values, and the radial coefficients represent bedding-parallel values.

Table 4.1. Data for linear thermal expansion coefficient of Nisku 1 (NSK1) core plug. Red boxes denote values used in sample calculation.

Temperature (°C)	**NSK1 ξ Axial (μξ)**	**NSK1 ξ Lateral (μξ)**	**NSK1 $\alpha_{T\text{-axial}}$ (μξ/°C)**	**NSK1 $\alpha_{T\text{-radial}}$ (μξ/°C)**
27.12	18	5		
33.47	43	17	3.94	1.89
44.87	89	48	4.04	2.72
63.57	160	113	3.80	3.48
45.19	82	48	4.24	3.54
34.22	36	17	4.19	2.83
28.04	12	5	3.88	1.94
Average =			4.02	2.73
Final Average =			3.37	

A typical graph of transient temperature increase vs. time generated using Hot Disk are shown in Figure 4.1. The average measurements of thermal conductivity (λ), thermal diffusivity (κ), and heat capacity per unit volume (ρC_P) interpreted from graphs of this type for core samples from the Calmar and Nisku Formation are listed in Table 4.2. This table also lists linear thermal expansion coefficient α_T. The first three thermal property measurements were taken at room temperature (20 ± 5°C) and atmospheric pressure, whereas the fourth thermal property (linear thermal expansion coefficient) was measured at atmospheric pressure while increasing temperature from 25 ± 5°C to

65 ± 5°C. Taking into consideration the errors of the techniques each measurement of the thermal conductivity, thermal diffusivity volumetric heat capacity, and linear thermal expansion coefficient, contain errors of roughly 5%.

It is interesting that the thermal results seem roughly the same for both Calmar and Nisku rocks samples. The thermal conductivity of the Calmar and Nisku rocks ranges from 3.12 to 4.05 and 3.08 $Wm^{-1\circ}C^{-1}$ to 4.67 $Wm^{-1\circ}C^{-1}$ respectively, thermal diffusivity ranges from 1.24 to 3.01 mm^2sec^{-1} and 1.51 to 1.72 mm^2sec^{-1} respectively, and heat capacity per unit volume ranges from 1.35 to 3.23 $MJm^{-3\circ}C^{-1}$ and 2.29 to 2.74 $MJm^{-3}K^1$ respectively. Linear thermal expansion coefficient values for axial and radial measurements have the range 3.40 to 7.09 $\mu\xi\cdot{}^0C^{-1}$ for the Calmar and 3.60 to 4.04 $\mu\xi\cdot{}^0C^{-1}$ for the Nisku. Temperature-dependence of linear thermal expansion coefficient does not seem substantial over the temperature range investigated. However, CMC3 and CMC4 have slightly higher thermal properties which could be due to their different mineralogy. There are not overwhelming differences in the axial and radial values of linear thermal expansion coefficient for most of the Calmar and Nisku samples tested. This is similar to results obtained on Berea sandstone samples tested parallel and perpendicular to the bedding plane by Somerton (1992), and is consistent with the fact that the samples tested in this work did not show a strongly laminar bedding fabric.

The values measured for each thermal property are generally consistent, which is interpreted to reflect similar lithologies of the samples (Sass et al., 1971, Huotari and Kukkonen, 2004, Cooper and Simmons, 1977, Bergman and Winter, 1995, Collieu et al., 1975). Two notable exceptions are the radial measurements for linear thermal expansion coefficient values of CMR3 and NSK1 which are significantly smaller than their axial values (Table 4.2). This may be due to some anomalies in lithology of those rocks samples or it could be an experimental error due to flaws in the epoxy or strain gauges. More data is given in the Appendix B.

The thermal data estimated from literature (Clauser and Huenges, Côté and Konrad, 2005, Fjær, 1999, Collieu et al., 1975, Hickox et al., 1986, Yaws, 2008, Lorenz et al., 1991) compares favorably with this measured data. The literature values with similar lithologies are 4.15 $W\ m^{-1\circ}C^{-1}$, 1.22 mm^2sec^{-1}, 3.38 $MJm^{-3\circ}C^{-1}$, $1.52\cdot10^5\ {}^\circ C^{-1}$ for thermal conductivity λ, thermal diffusivity κ, specific heat ρc_p and linear thermal expansion coefficient α_T respectively.

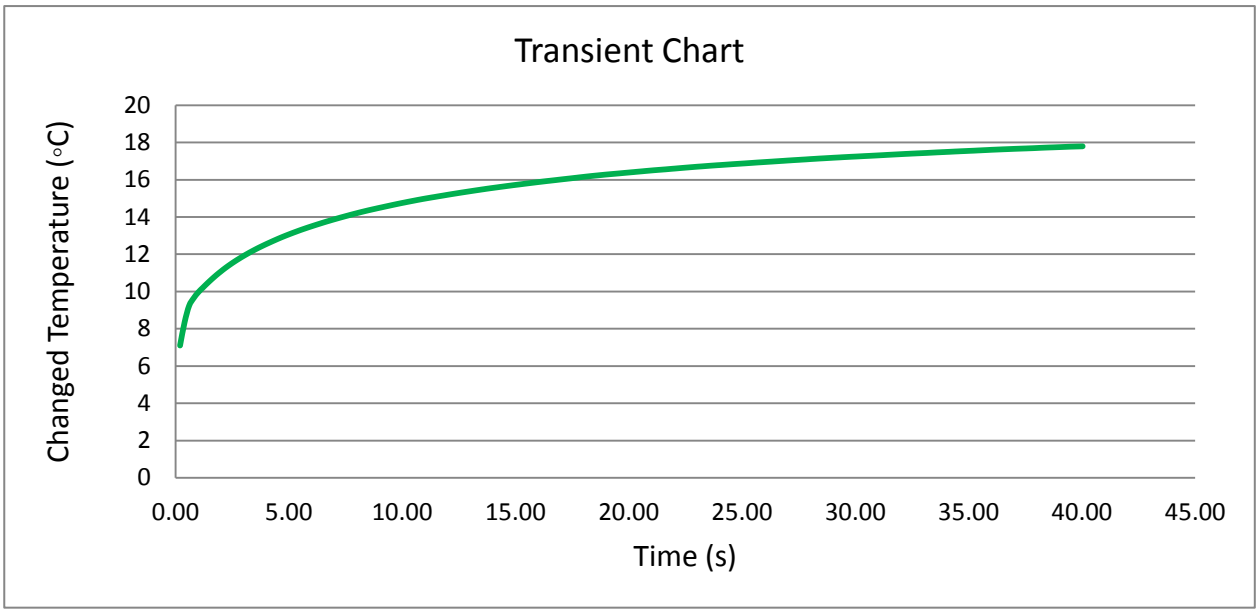

Figure 4.1. The transient temperature increase versus time window for CMR1.

Table 4.2. Experimental thermal conductivity (λ), thermal diffusivity (κ), and volumetric heat capacity (ρC_P) of specimens at normal temperature and pressure. The linear thermal expansion coefficient (α) values were measured while increasing and decreasing temperature from 25 ± 5°C to 65 ± 5°C. Porosity (ϕ), and Grain density (ρ_{gr}) were measured and reported previously by Schlumberger.

Sample	Depth (m)	λ ($W \cdot m \cdot {}^{\circ}C^{-1}$)	K ($m^2 \cdot s^{-1}$)	ρC_P ($J \cdot m^{-3} \cdot {}^{\circ}C^{-1}$)	$\alpha_{T\text{-axial}}$ ($\mu\xi \cdot {}^{\circ}C^{-1}$)	$\alpha_{T\text{-radial}}$ ($\mu\xi \cdot {}^{\circ}C^{-1}$)	$\alpha_{T\text{-average}}$ ($\mu\xi \cdot {}^{\circ}C^{-1}$)	Φ %	ρ_{gr} $kg \cdot m^{-3}$
CMR1	1789.00	3.55	$1.83 \cdot 10^{-6}$	$1.97 \cdot 10^{6}$	3.38	3.42	3.40	3.68	2830
CMR2	1791.97	3.12	$1.41 \cdot 10^{-6}$	$2.21 \cdot 10^{6}$	3.46	3.52	3.49	4.18	2801
CMR3	1792.86	4.02	$1.24 \cdot 10^{-6}$	$3.23 \cdot 10^{6}$	7.94	4.29	6.12	1.66	2803
CMR4	1793.19	4.05	$3.01 \cdot 10^{-6}$	$1.35 \cdot 10^{6}$	7.92	6.25	7.09	1.51	2834
NSK1	1796.22	4.09	$1.68 \cdot 10^{-6}$	$2.47 \cdot 10^{6}$	4.02	2.73	3.37	8.21	2820
NSK2	1805.00	3.98	$1.51 \cdot 10^{-6}$	$2.65 \cdot 10^{6}$	3.80	3.61	3.71	4.42	2820
NSK3	1807.92	4.67	$1.72 \cdot 10^{-6}$	$2.74 \cdot 10^{6}$	3.78	4.25	4.02	2.63	2810
NSK4	1839.73	4.00	$1.56 \cdot 10^{-6}$	$2.58 \cdot 10^{6}$	3.65	3.64	3.64	3.51	2810
NSK5	1844.94	3.80	$1.67 \cdot 10^{-6}$	$2.29 \cdot 10^{6}$	3.66	3.43	3.54	4.52	2810

4.3 Surface Deformation Due to Injection of Cold CO_2

4.3.1 Estimation of Temperature-Induced Displacements during CO_2 Injection:

To estimate temperature-induced displacements, temperature distribution around a CO_2 injection well is estimated using the analytical model described in section 2.8. Figure 4.2. Temperature distribution around a CO2 injection well as a function of radial distance. shows the temperature distribution around a CO_2 injection well as a function of radial distance as calculated using equation 2.9. Details pertaining to the calculation of this temperature distribution are given in Appendix E. In this modeling, it is assumed that CO_2 is injected at a rate of one megaton per year into 70 m thick reservoir for a period of 50 years. (This corresponds to injection at a volumetric rate of 1680672.3 m^3 per year, based on a CO_2 density of 857 $kg{\cdot}m^{-3}$, as determined for a temperature of 30°C and pressure of 30 MPa using the following website: http://www.peacesoftware.de/einigewerte/co2_e.html). Most of the mechanical properties used in this calculation are taken from commercial laboratory measurement of TerraTek (2011) and results are summarized in Table 4.3. The temperature induced vertical stress change within the reservoir can be calculated using equation (2.10) (Soltanzadeh et al., 2009):

$$\Delta\sigma_v = \left(\frac{1+\nu}{1-\nu}\right)\left(\frac{\pi e}{2}\right) 2s\,\eta\Delta T \tag{2.10}$$

Where eccentricity e = ½ reservoir height / plume radius = 35/350 = e = 0.1

$$\Delta\sigma_v = \left(\frac{1+\nu}{1-\nu}\right)\left(\frac{\pi e}{2}\right) 2s\,\eta\Delta T$$

$$\Delta\sigma_v = \left(\frac{1+0.2}{1-0.2}\right)\left(\frac{\pi \times 0.011}{2}\right) \times 2 \times (1.38 \cdot 10^{10}\text{Pa}) \times (3.65 \cdot 10^{-6}\text{°C}^{-1}) \times (-40\text{°C})$$

$$\Delta\sigma_v = -969454 \text{ Pa} \sim -0.97 \text{ MPa}$$

Where uniaxial compaction coefficient is:

$$C_v = \frac{(1-2\upsilon)(1+\upsilon)}{E(1-\upsilon)} \tag{2.11}$$

$$C_v = \frac{(1-2\times 0.2)(1+0.2)}{(6.15 \cdot 10^{10}\text{Pa}) \times (1-0.2)}$$

$$C_v = 1.46 \cdot 10^{-11} Pa^{-1}$$

Neglecting the effects of pressure-induced change (which are addressed in section 4.3.2), the magnitude of reservoir contraction (ΔH) due to cold CO_2 injection can be calculated as:

$$\Delta H = C_v \Delta \sigma_v H$$

$$\Delta H = (1.46 \cdot 10^{-11} Pa^{-1})(-969454\ Pa)(70\ m)$$

$$\Delta H = -0.00099\ m$$

$$\Delta H \sim -1\ mm$$

The magnitude of the maximum surface deformation (S) induced by cold CO_2 injection is:

Where as $$S = 2(1-\upsilon)\left[1 - \frac{1}{\sqrt{1+(R_c/D)^2}}\right] \times \Delta H$$

$$S = 2(1-0.2)\left[1 - \frac{1}{\sqrt{1+(350/1895)^2}}\right] \times -0.00099$$

$$S = -0.000027\ m \sim -0.03\ mm$$

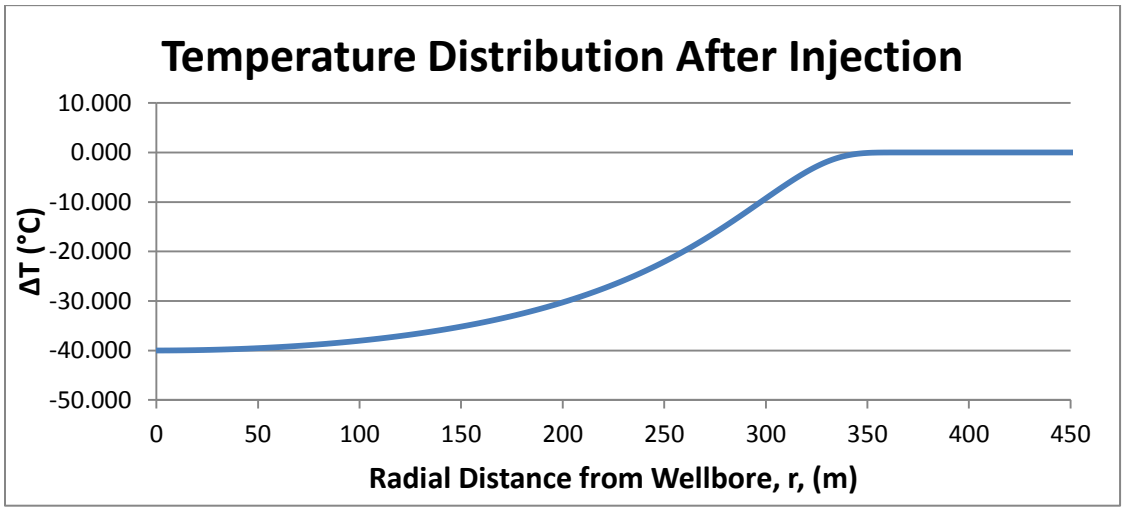

Figure 4.2. Temperature distribution around a CO_2 injection well as a function of radial distance.

4.3.2 Estimation of Pressure-Induced Displacements by Numerical Modeling:

As described in the previous section, the estimation of thermally-induced stresses and displacements can be conducted using analytical models, due to the relatively uniform temperature distribution within the temperature plume. The application of similar methods to analyzing pressure-induced stresses and displacements is problematic because pressure distributions tend to be more variable. In order to obtain a rough estimate of pressure-induced displacements, numerical modeling was conducted using RS2 (by Rocscience), a finite element-based application for analyzing coupled flow-geomechanical problems. In this modeling, it is assumed that CO_2 is injected at a rate of 1 Mt per year into a 70 m thick reservoir for a period of 50 years.

Based on results reported by Goodarzi et al. (2012), who conducted flow simulations using a multi-phase flow simulator, the maximum extent of the pressure plume was interpreted as approximately 73,000 m because no significant pressure change was observed beyond this distance. As such, an axisymmetric model with a radius of 73,000 m was developed in RS2, with a vertical injection well at its centre, as shown in Figure 4.3. The bottom of the model domain was fixed in the x and y (horizontal and vertical) directions, the left and right boundaries were fixed in the x direction, and ground surface was unconstrained (free surface). Pore pressures were initially hydrostatic throughout the model domain (increasing with depth on a 10 kPa/m gradient). For a 50 year period, injection well pressure in the Nisku Formation was set at 30,000 kPa (similar to the "below fracture pressure" scenario in Goodarzi et al., 2012).

RS2 can only model single-phase flow, hence the hydraulic conductivity was set at a value appropriate for CO_2, given that most of the flow (and the steepest pressure gradients) occur close to the injection well, where CO_2 saturation is greatest. More specifically, hydraulic conductivity (*K*) for the Nisku Formation was calculated as follows:

$$K = \frac{\rho \cdot g}{\mu} k = \frac{(856\ kg/m^3)(9.81\ m/s^2)}{(9.0 \cdot 10^{-5} Pa \cdot s)} (3.0 \cdot 10^{-14}\ m^2) = 2.8 \cdot 10^{-6}\ m/s$$

Where:

ρ = fluid density

g = gravitational acceleration

μ = viscosity

k = intrinsic permeability

Other input parameters used for the modeling as listed in Table 4.3. Properties for all overlying and underlying rocks were set equal to the values for the Calmar Formation in order to simplify the model. Sensitivity analyses showed that model outputs were not sensitive to these properties (Goodarzi et al., 2012).

Modeled pore pressure profiles at various time up to 50 years ($1.58 \cdot 10^9$ s) are shown in Figure 4.4. (These profiles illustrate afore-mentioned steep pressure gradients that exist near an injection well, which are poorly suited to analytical geomechanical models.) Predicted upwards displacement at the top of the Nisku Formation (point A on Figure 4.3) after 50 years of injection is 2.4 mm, and predicted ground surface uplift at the centre of the reservoir (point B) is 1.8 mm.

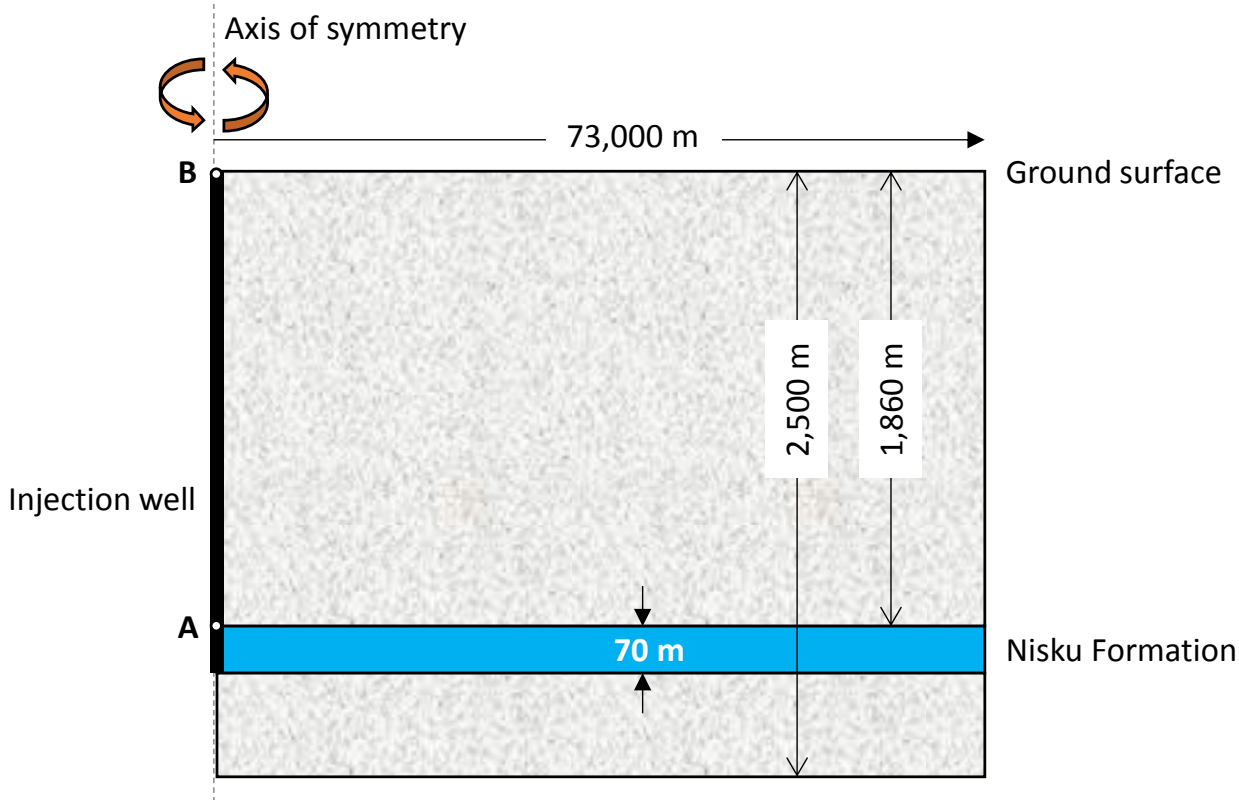

Figure 4.3. Geometry used to model pressure-induced stresses and displacements.

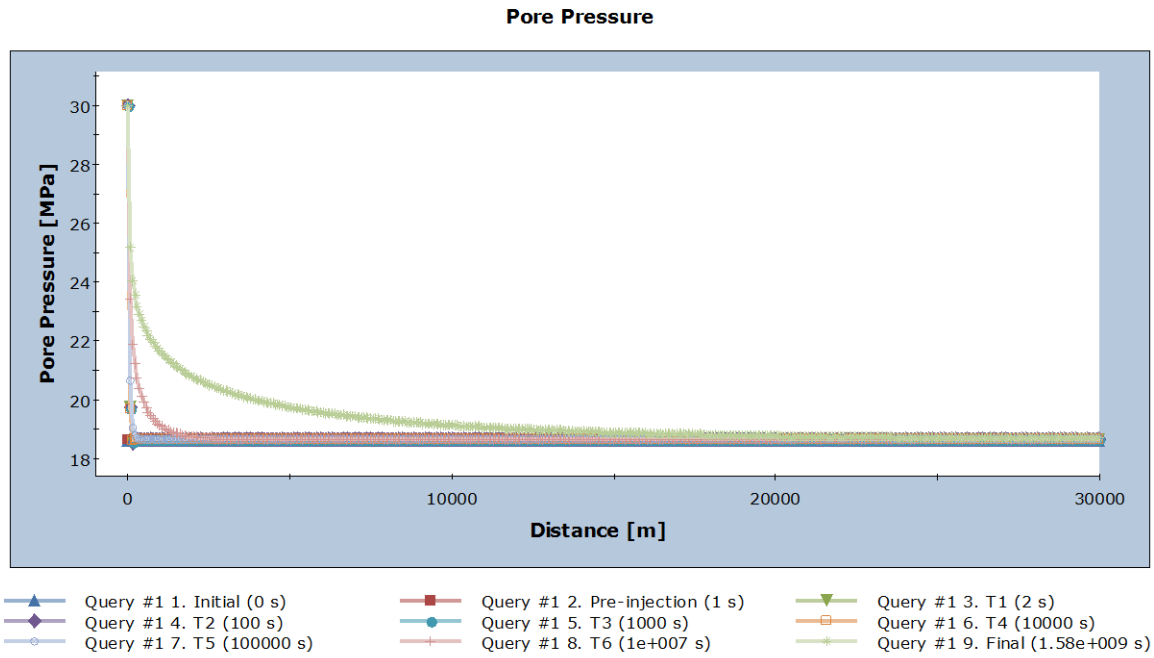

Figure 4.4. Predicted pore pressure profiles at times ranging up to 50 years ($1.58 \cdot 10^9$ s).

4.3.3 Discussion of Pressure and Temperature-Induced Displacements:

The combined total deformation effect of thermal and pressure in the well and on the surface due to cold injection of CO_2 is 1.4 mm expansion at the reservoir and 1.77 mm uplift at the surface. It can clearly be seen that the pressure-induced deformation is greater than the thermally-induced component, both at the reservoir level and at ground surface. An interesting aspect of these results is the fact that the magnitude of total ground surface uplift is greater than the magnitude of the reservoir expansion. This occurs because the thermal plume is much smaller than the pressure plume. As such, though the thermally-induced deformations are of notable magnitude in the reservoir (1 mm of contraction), the amount of thermally-induced deformation transmitted to ground surface is negligible because of the small size of thermal plume.

The total values of displacement calculated in this work (given in Table 4.4) are of the same order of magnitude (but smaller than) the values obtained by Goodarzi and Settari (2016), who obtained 2.8 and 6.5 mm of surface and reservoir uplift, respectively (Figure 4.5). The slight discrepancies in values could be due to the fact that the values calculated in this work are based on combination of a simple analytical model and axisymmetric numerical model whereas Goodarzi and Settari (2016) used a fully integrated 3D numerical model. Also this discrepancy could be due to different thermal plume sizes calculated in this study (350 m) and Goodarzi and Settari (2016) study (4.5 km). The negative value indicates subsidence and the measured millimeter range value can be monitored by InSAR and this measurable deformation could be an indication that CO_2 has migrated in the reservoir.

Table 4.3. Summary of key input parameters used in calculations for surface deformation (after Goodarzi and Settari, 2016; TerraTek, 2011).

Property	Values used in this study
General	
Vertical stress gradient (kPa m^{-1})	23
CO_2 injection temperature (ºC)	30
CO_2 density (kg·m^{-3})	857
Specific heat of injected CO_2, (J kg^{-1} ºC^{-1})	1847
Maximum end point CO_2 saturation (%)	58
Vertical stress gradient (kPa m^{-1})	23
CO_2 density (kg·m^{-3})	857
Salinity of formation water (mg $liter^{-1}$)	190,000
Density of formation water (kg m^{-3})	1,155
Viscosity of formation water (mPa s)	0.84
Nisku Formation	
Nisku reservoir top depth (m)	1860
Nisku thickness (m)	70
Initial pressure in Nisku reservoir (MPa)	Depth × 0.010
Maximum allowable bottom-hole pressure in Nisku (MPa)	30
Nisku reservoir temperature (ºC)	70
Nisku, carbonate young's modulus (kPa)	$61.5 \cdot 10^7$
Nisku, carbonate shear modulus (kPa)	$1.38 \cdot 10^7$
Nisku, carbonate bulk modulus (kPa)	$2.4 \cdot 10^7$
Nisku, carbonate density (kg m^{-3})	2673
Nisku porosity (%)	6.4
Effective Nisku porosity (%)	3.71
Nisku linear thermal expansion coefficient (ºC^{-1})	$3.65 \cdot 10^{-6}$
Specific heat of Nisku (J kg^{-1} ºC^{-1})	937.06
Thermal conductivity of Nisku (W m ºC^{-1})	3.50
Nisku minimum stress gradient (kPa m^{-1})	16.2
Nisku poisson's ratio	0.21
Nisku horizontal permeability (md)	43
Nisku vertical permeability (md)	6
Calmar Formation	
Calmar thickness (m)	43
Calmar, shale young's modulus (kPa)	$72.0 \cdot 10^7$
Calmar, shale shear modulus (kPa)	$1.38 \cdot 10^7$
Calmar, shale bulk modulus (kPa)	$2.4 \cdot 10^7$
Calmar density (kg m^{-3})	2718
Calmar linear thermal expansion coefficient (ºC^{-1})	$7.20 \cdot 10^{-5}$
Calmar minimum stress gradient (kPa m^{-1})	16.3
Calmar poisson's ratio	0.14
Thermal conductivity of Calmar (W m ºC^{-1})	3.69
Specific heat of Calmar (J kg^{-1} ºC^{-1})	777.96
Calmar horizontal permeability (nd)	30
Calmar vertical permeability (nd)	0.3

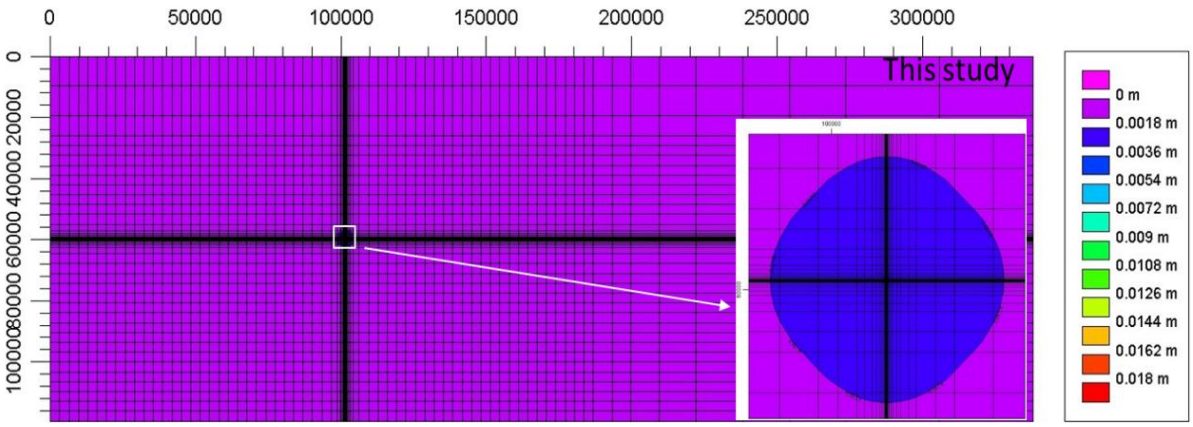

Figure 4.5. Vertical displacement (in meters) at the ground surface after 50 years of injection at 1 Mty^{-1}, below fracture pressure (Goodarzi and Settari, 2016).

Table 4.4.Output values from modeling calculation and Goodarzi and Settari (2016) values.

Displacement	Thermally-induced	Pressure induced	Total	Goodarzi and Settari (2016)
ΔH	-1 mm	2.4 mm	1.4 mm	6.5 mm
S	-.03 mm	1.8 mm	1.77 mm	2.8 mm

4.3.4 Temperature Induced Horizontal Stress Changes

The temperature induced horizontal stress changes were calculated using equation 2.6 as follows:

$$\Delta\sigma_{H1} = \Delta\sigma_{H2} = \left(\frac{1+\nu}{1-\nu}\right)\left(1-\frac{\pi e}{4}\right) 2s\,\eta\Delta T \qquad (2.6)$$

$$\Delta\sigma_{H1} = \Delta\sigma_{H2} = \left(\frac{1+0.21}{1-0.21}\right)\left(1-\frac{\pi\times\ 0.1}{4}\right)\times\ 2\ \times(\ 1.38\ \cdot\ 10^{10}\text{Pa})$$
$$\times\ (3.65\ \cdot\ 10^{-6}\text{°C}^{-1})\ \times\ (-40\text{°C})$$

$$\Delta\sigma_{H1} = \Delta\sigma_{H2} = -1324648\ \text{Pa}\ \sim\ -1.33\ \text{MPa}$$

Here $\Delta\sigma_{H1}$ and $\Delta\sigma_{H2}$ correspond to the changes in maximum and minimum horizontal stress, respectively. The value (-1.33 MPa) must be subtracted from both maximum and minimum horizontal stresses to get their final values. The decrease in minimum horizontal stress causes reduction of fracturing pressure and this reduction in fracturing pressure decreases the pressure differential available for injection, and therefore injectivity. In the case of injection at fracturing

conditions, the fracture propagation pressure will decrease and, if the same injection rate is used, this will accelerate fracture propagation. As relatively cold CO_2 (at approximately 30°C) will probably be injected into the Nisku formation (at 70°C), thermal effects of injection should be taken into consideration. It is not adequate to consider the operating pressure on the minimum in situ stress. This fact needs to be taken into account by operators and by regulatory agencies. If it is necessary to operate below fracturing, the variation of fracture pressure under injection condition can be determined using geomechanical modeling and its minimum value should be taken as the maximum operating pressure.

4.4 Matrix Reactivity Experiment

Front and back views of three sub-samples of Sample CMR3 are shown in Figure 4.6 and Figure 4.7, respectively. Sub-sample CMR3-1 was exposed to fluid I (i.e., original Nisku Formation Brine – see Table 3.2); sub-sample CMR3-2 was exposed to fluid II (i.e., Nisku Formation brine predicted after 50 years of CO_2 injection – see Table 3.2); and the sub-sample labeled "reference" was not exposed to any brine. In Figure 4.8 adjacent sides of the sub-samples are shown as follows: side A of CMR3-1 (right), side

B of CMR3-2 (left) and reference sample (middle) with A′ (adjacent to A) and B′ (adjacent to B). After visual examination of these sub-samples, it was quite clear that sub-sample CMR3-2 (with fluid II reaction) showed a higher degree of reaction with acidic brine as compared to sub-sample CMR3-1 (with fluid I reaction) because the subsample CMR3-2 surface was observed to be deeper yellow in colour and parts of its surface appeared to have dissolved. It was also observed that the brine in the mixing vessel after the experiment on sub-sample CMR3-2 was murkier than the brine after the experiment on sub-sample CMR3-1, and there were more powder-like grains deposited in the mixing vessel for the sub-sample CMR3-2 experiment. These observations are viewed as an indication of more mineral dissolution for sub-sample CMR3-2 than subsample CMR3-1, followed by re-precipitation of minerals in the mixing vessel.

To examine mineralogical alterations of the surfaces, the surfaces were sectioned and prepared for SEM imaging and analysis (images shown in Appendix C). Major mineral contents (in percentage) of sub-samples CMR3-1 and CMR3-2 before and after reaction with brine I and brine II (respectively) are shown in Table 4.4. In this table, it is obvious that the dolomite content is increasing in sub-sample CMR3-1 and decreasing for CMR3-2. The opposite is the case for calcite

content; i.e., it is increasing for sub-sample CMR3-2 and decreasing for sub-sample CMR3-1. This suggests that magnesium from the brine was replacing calcium in the rock for sub-sample CMR3-1 (fluid I), while the opposite was occurring (calcium replacing magnesium) with sub-sample CMR3-2. This is the opposite of what was expected, given that calcium concentration was high (and magnesium concentration low) in brine I, while the opposite was true for bine II.

In both cases, it is noted that NaCl content increased, which is interpreted to be a consequence of NaCl surface sorption on the sub-sample surfaces. Minor changes (of a few percent) were observed for the other minerals analysed; the biggest change is the increase in illite content (from 0% to 8%) observed in sub-sample A (fluid I). No obvious explanation for this is apparent, hence this could be due to experimental error. There was a porosity increase (from 3.2% to 4.4 %) observed in sub-sample CMR3-2 due to loss of mass but almost no porosity change observed in sub-sample CMR3-1.

Figure 4.6. Front view of samples pieces of CMR3, sample CMR3-1 (right), sample CMR3-2 (left) after matrix reactivity tests and reference sample (middle).

Figure 4.7. Back view of samples pieces of CMR3, sample CMR3-1 (right), sample CMR3-2 (left) after matrix reactivity tests and reference sample (middle).

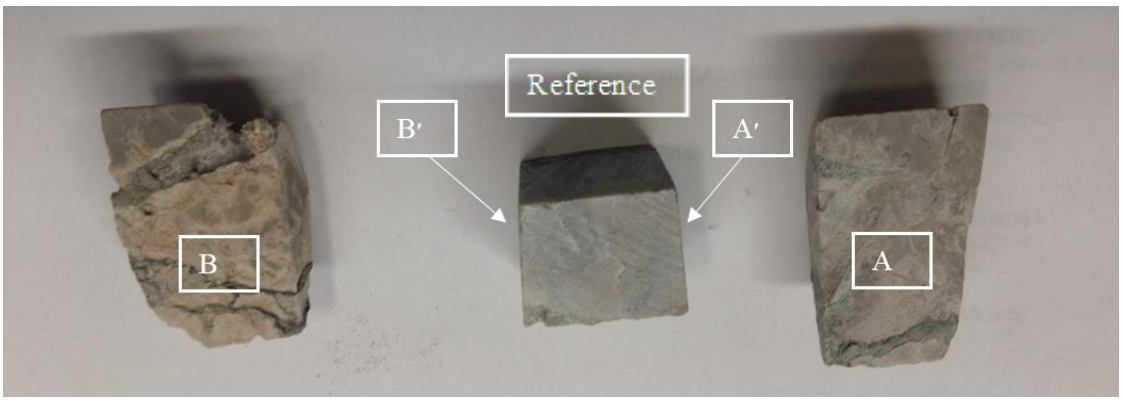

Figure 4.8. Adjacent sides of samples pieces of CMR3, side A (right), side B (left) and reference sample (middle) with A′ (adjacent to A) and B′ (adjacent to B) side.

Table 4.5. Major mineral contents in percentage of CMR3 sub-samples sides A, A′, B and B′ before and after reaction with brines I and II, respectively.

Minerals	A %	A′ %	B %	B′ %
Calcite	18	45	54	30
Dolomite	32	19	12	34
Fe-chloride	2	5	-	-
Fe-oxide	4	5	-	-
Illite	8	-	-	-
K-feldspar	4	-	4	3
Mg-calcite	2	-	-	-
Minor clay	4	5	-	7
NaCl	14	5	21	12
Pyrite	6	10	9	14
Quartz	6	6	-	-

4.5 Permeability of Intact Rock

4.5.1 Sample CMR2

Results of the pressure pulse permeability testing conducted on Calmar sample CMR2 are presented in Figure 4.9. When analyzing pressure pulse permeability test results, the easiest method of interpretation is to fit a straight line to the linear late-time portion of the ln (ΔP) versus time curve. The deviation in a linear late-time portion of the ln (ΔP) vs. time curve is probably due to temperature change during the experiment, see Figure 4.10. The permeability calculated for sample CMR2 is $3.03 \cdot 10^{-22}$ m^2 (approximately 0.3 nd). This value was calculated using equation 2.2, as follows:

$$k = \frac{-\alpha \mu L S S_u S_d}{A(S_u + S_d)} \tag{2.2}$$

Where:

a = $1.5 \cdot 10^{-5}$ s^{-1} (slope from Figure. 4.3)

μ = $640 \cdot 10^{-6}$ Pa·s (Grimes et al., 1979; Duan et al., 2006)

L = 0.03156 m

$S_u = 9.13 \cdot 10^{-6} \times 4.07 \cdot 10^{-9} = 3.72 \cdot 10^{-14}$ $m^3 \cdot Pa^{-1}$ (Fine and Millero, 1973)

$S_d = 9.05 \cdot 10^{-6} \times 4.07 \cdot 10^{-9} = 9.65 \cdot 10^{-14}$ $m^3 \cdot Pa^{-1}$ (Fine and Millero, 1973)

A = 0.002026 m^2

k = $3.03 \cdot 10^{-22}$ m^2 ~ 0.3 nd

The estimated value of viscosity from literature was a function of temperature, pressure and salinity. The compressive storage was approximated here for the upstream and downstream systems by multiplying the brine compressibility with the total void volume of the porous disks and inside the connecting tubes between the valves and the sample; this assumes that the compressibility of the stainless steel is negligible compared to the brine compressibility.

No additional permeability tests were conducted on intact samples because samples were available for a limited time and the test required long test duration. The expectation is that permeability for all intact Calmar samples would be very low, which emphasizes the practical value of investigating a comparative higher permeability value of fractured samples.

4.5.2 Comparison against Other Caprocks

The very low permeability value interpreted for sample CMR2 falls within the range of caprock permeabilities published previously by various authors (see Table 4.5). A similar experiment was done on the Calmar sample, but with slightly different depths, by TerraTek (2011) which measured approximately 75 nd, which is 2 orders of magnitude greater than the value obtained for sample CMR2 (although still very low). One reason for this discrepancy could be heterogeneity of the Calmar Formation. A second reason could be due to the fact that TerraTek used gas while measuring permeability, which should give a higher value than the liquid permeability due to the Klinkenberg (gas slippage) effect (Tanikawa, 2006). The Calmar Formation permeability value reported in the WASP study (2008), which was estimated using wireline logs, was 30 nd (Michael et al., 2008).

The effective gas permeability of anhydrite caprock measured by Li et al. (2005) ranged between 30 - 600 nd. Hildenbrand et al. (2002) studied Boom Clay caprocks and found effective

permeabilities ranging from $2.4 \cdot 10^{-21}$ to $1 \cdot 10^{-18}$ m^2 (2.4 nd to 1000 nd), though their samples' lithologies were somewhat different (sandstone, limestone and dolomite) from the caprock studied in this research. Permeabilities measured by Liu (2015) on mudstone caprock ranged from 1000 nd to10 nd, and permeability measured by Armitage et al. (2016) found 10 nd for Mercia Mudstone in the UK. The Mercia samples analyzed were either clay-rich (muddy) siltstones or relatively clean siltstones cemented by carbonate and gypsum. These literature values are close to the value measured in this research on caprock samples.

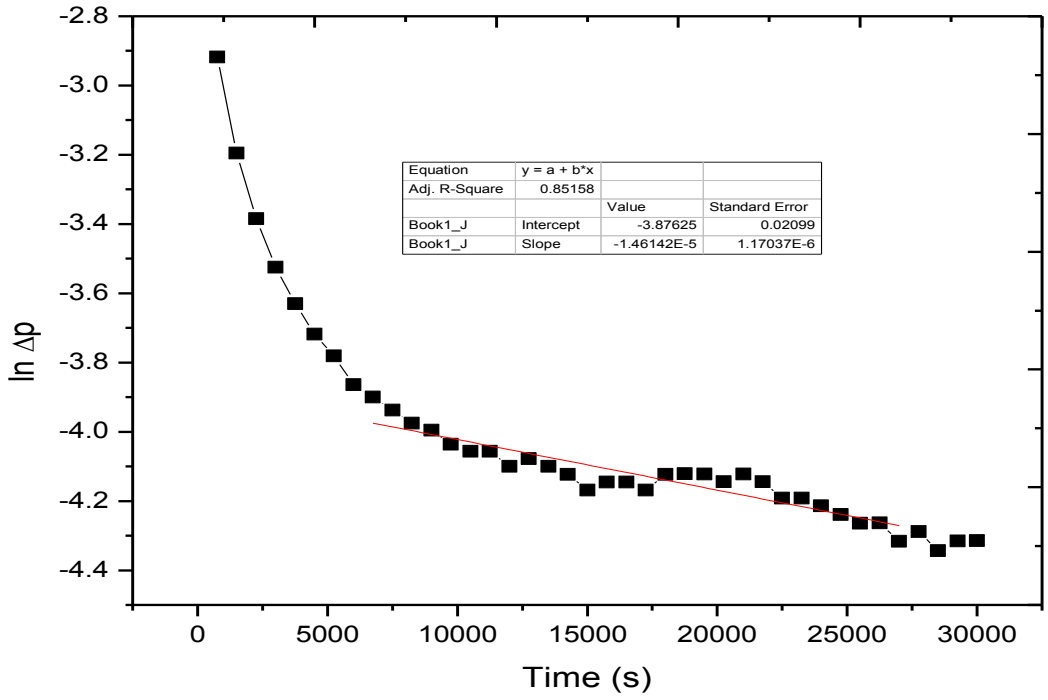

Figure 4.9. Pressure pulse permeability results for sample CMR2.

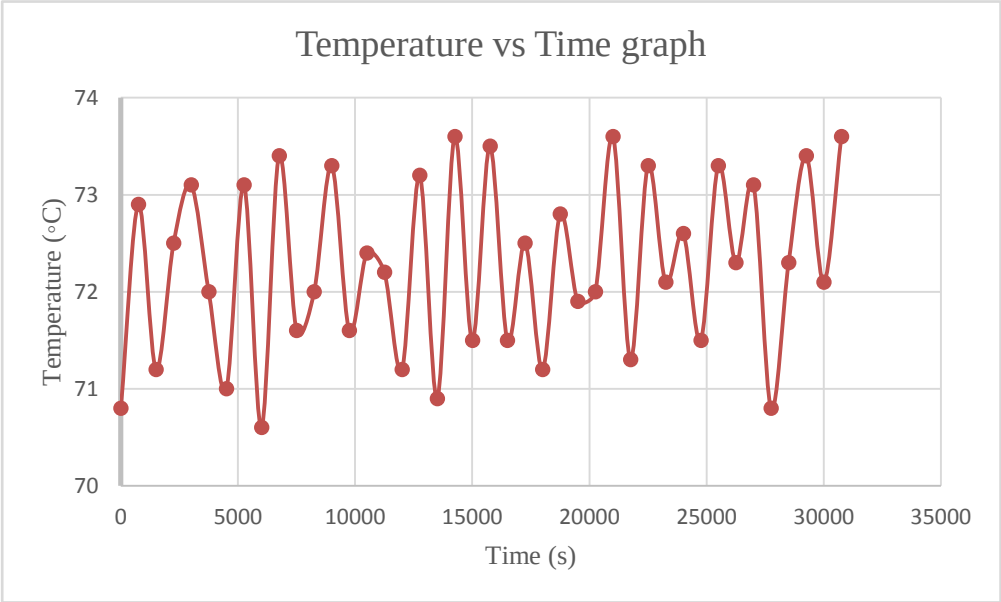

Figure 4.10. Temperature vs. time graph of the system while running the pulse permeability experiment for samples CMR2.

4.5.3 Evaluation of Error Associated with Permeability Determination

As mentioned in Section 2.1, the error associated with calculating permeability using Equation 2.1 is mostly based on the ratio of the effective sample pore volume and the reservoir volume. The criterion established by Trimmer (1981) to obtain an error less than 10% is as follows:

$$\frac{AL}{S_u+S_d} \cdot \frac{1}{M} \leq 0.25$$

Where:

A = cross-sectional area of the sample (CMR2)

L = length of the sample (m)

S_u = compressive storages for the upstream ($m^3 \cdot Pa^{-1}$)

S_d = downstream reservoirs ($m^3 \cdot Pa^{-1}$)

M is a parameter related to the compressive storage of the sample, defined as follows:

$$M^{-1} = nC_f + [\beta(1 + n) - n] C_b$$

Where:

n = porosity of the sample,

C_f = compressibility of the pore fluid (Pa^{-1})

β = Biot's coefficient

C_b = bulk compressibility of the rock (Pa^{-1})

Using rock and water compressibilities of $3.98 \cdot 10^{-11}$ and $4.4 \cdot 10^{-14}$ Pa^{-1}, respectively (Dake, 1978), with a porosity of 3%, the value for M^{-1} for CMR2 is approximately $5.3 \cdot 10^{-11}$ Pa^{-1}. Using the sample CMR2 dimensions given above, Trimmer's compressive storage ratio for sample CMR2 is calculated to be 0.025, which is significantly lower than the recommended value of 0.25. In reality, the greater potential for error is likely due to uncertainty in defining exactly which data points in Figure 4.9 represent "late time" data and the effects of temperature fluctuations on pressure. Even if these factors result in errors of the order of several tens of percent, the impact would have limited practical significance; the measured permeability is very low compared to reservoir permeability, regardless of some error in the slope fitting.

Table 4.6. Permeability values for some caprock after (Larsen, 2011).

Author and Year	Rock Type	Test Type	Location	Permeability (nd)
Katsube et al., 1996	Shale	Lab	Beaufort-Mackenzie Basin	0.2 to 19
Katsube et al., 1998	Shale	Lab	Scotian Shelf Beaufort-Mackenzie Basin Western Canada Sedimentary Basin	0.9 to 23.9 0.2 to 14.8 0.82 to 3.1
Horsrud et al., 1998	Shale	Lab	North Sea	3 to 317
Katsube et al., 1991	Shale	Lab	Scotian Shelf	0.1 to 16
Bredehoeft et al., 1983	Pierre Shale	Lab	Local	500
Bredehoeft et al., 1983	Pierre shale	Field	Regional	6,000
Neuzil et al., 1984	Pierre Shale	Lab	Local (pulse testing)	30 to 300
Neuzil et al., 1984	Pierre Shale	Field	Regional (in situ testing)	300 to 3000
Chan 2005 (unpublished)	Lea Park Shale	Lab	Weyburn, SK	0.1 to 1
Li et al., 2005	Midale anhydrite	Lab	Weyburn, SK	30-600
Larsen, 2011	Colorado Shale	Lab	Rocanville, SK	8 to 46
	LeaPark Shale		Weyburn, SK	14 to 35
Wei Liu et al., 2015	Jintan mudstone	Lab	Jintan China	10-1000
Armitage et al., 2016	Mercia mudstone	Lab	East Midlands Nottingham UK	10

4.6 Permeability of Fractured Samples and Effluent Chemistry

A sample of the data collected for fractured sample CMR1 is given in Table 4.7, as well as the calculated permeability. More detailed data is provided in Appendix D. Following is a sample calculation conducted on one row of data highlighted in Table 4.7:

For steady state flow, permeability is calculated using equation 2.1 as:

$$k = \frac{L \cdot \mu \cdot Q}{A \cdot \Delta P} \tag{2.1}$$

Where:

μ = fluid viscosity = $640 \cdot 10^{-6}$ Pa·s (Duan et al., 2006, Grimes et al., 1979)

Q = fluid flow rate at steady-state condition = $1.3 \cdot 10^{-9}$ $m^3 \cdot s^{-1}$

L = length of the specimen = 0.03349 m

A = cross-sectional area of the specimen = 0.002026 m^2

ΔP = pressure drop across the sample = 1785742.14 Pa

$$k = \frac{0.03349 \cdot 640 \cdot 10^{-6} \cdot 1.3 \cdot 10^{-9}}{0.002026 \cdot 1785742.14}$$

$$k = 7.77 \cdot 10^{-18} m^2 \sim 78\ \mu d$$

This permeability represents the permeability of an intact sample that would achieve the same flow rate as the fractured sample when subjected to the same pressure gradient.

Table 4.7. A sample data collected during permeability measurement of fractured sample CMR1. The highlighted row of data was used in the sample calculation given in the text.

Time (sec)	Cell pressessure ($10^6 \cdot$ Pa)	Cell Temperature (°C)	Room Temperature (°C)	Flow Rate m^3/sec	Pressure Difference ($10^6 \cdot$ Pa)	k (μd)	k (m^2)
1805	17.49	62.7	22.41	2.17E-09	1.78	1.30E+01	1.30E-17
1865	17.49	57.14	22.45	2.17E-09	1.78	1.30E+01	1.30E-17
1925	17.49	53.28	22.51	2.17E-09	1.78	1.29E+01	1.29E-17
1985	17.49	50.71	22.39	1.3E-09	1.78	7.77E+00	7.77E-18
2045	17.49	72.45	22.33	2.17E-09	1.78	1.29E+01	1.29E-17
2105	17.49	66.88	22.41	1.73E-09	1.78	1.04E+01	1.04E-17
2165	17.49	60	22.37	1.3E-09	1.78	7.77E+00	7.77E-18
2225	17.49	55.28	22.42	2.17E-09	1.78	1.29E+01	1.29E-17
2285	17.49	52.18	22.36	1.73E-09	1.78	1.04E+01	1.04E-17
2345	17.49	74.02	22.3	1.3E-09	1.78	7.77E+00	7.77E-18
2405	17.49	67.33	22.3	2.17E-09	1.78	1.29E+01	1.29E-17
2465	17.49	60.32	22.34	8.67E-10	1.78	5.18E+00	5.18E-18
2525	17.49	55.43	22.39	1.3E-09	1.78	7.77E+00	7.77E-18
2585	17.49	63.14	22.35	2.17E-09	1.78	1.29E+01	1.29E-17
2645	17.49	75.52	22.33	8.67E-10	1.78	5.18E+00	5.18E-18
2705	17.49	66.74	22.35	2.17E-09	1.78	1.29E+01	1.29E-17
2765	17.49	59.69	22.39	8.67E-10	1.78	5.20E+00	5.20E-18
2825	17.49	54.96	22.31	1.3E-09	1.79	7.74E+00	7.74E-18
2885	17.49	72.19	22.38	8.67E-10	1.78	5.18E+00	5.18E-18
2945	17.49	71.74	22.41	2.17E-09	1.78	1.30E+01	1.30E-17
3005	17.49	63.55	22.28	1.3E-09	1.78	7.77E+00	7.77E-18
3065	17.49	57.58	22.3	8.67E-10	1.78	5.18E+00	5.18E-18
3125	17.49	56.68	22.3	1.3E-09	1.78	7.77E+00	7.77E-18
3185	17.49	78.93	22.29	1.73E-09	1.79	1.03E+01	1.03E-17
3245	17.49	69.91	22.25	1.3E-09	1.79	7.74E+00	7.74E-18
3305	17.49	61.79	22.42	8.67E-10	1.79	5.20E+00	5.20E-18
3365	17.49	56.25	22.44	1.3E-09	1.79	7.77E+00	7.77E-18
3425	17.49	67.44	22.39	2.17E-09	1.79	1.29E+01	1.29E-17
3485	17.49	73.42	22.33	8.67E-10	1.79	5.18E+00	5.18E-18
3545	17.49	64.89	22.42	1.3E-09	1.79	7.77E+00	7.77E-18
3605	17.49	58.3	22.41	8.67E-10	1.79	5.18E+00	5.18E-18
3665	17.49	55.76	22.22	8.67E-10	1.79	5.16E+00	5.16E-18
3725	17.49	76.37	22.18	1.3E-09	1.79	7.80E+00	7.80E-18
3785	17.49	68.08	22.34	2.17E-09	1.78	1.30E+01	1.30E-17

The permeabilities interpreted for fractured samples CMR1 and CMR4 are shown in Figure 4.11 and Figure 4.12, respectively. Based on these results neither of the fractured samples showed significant permeability changes and no definitive trend of changing permeability with time is seen. Permeability might show a weak upwards trend with time for CMR1 in the presence of brine I (initial brine) and a weak downwards trend for CMR4 with brine II (brine after 50 years of CO_2 injection). For reactive flows, changes in fracture permeability can be primarily attributed to three possible mechanisms: the dissolution of critical fracture asperities, particle clogging along the fracture pathway, and mineral precipitation (Ellis, 2011).

Step changes observed in the calculated permeabilities are likely due to poorly chosen resolution of pressure gauges and flow measurement devices used in the experiment. Stick-slip movement of the piston in the accumulator (moving back and forth keeping the pressure difference constant) and the presence of salt and grain particles in the brine hindering flow might also have been a factor.

Based on the results presented in Table 4.7 the effluent electrical conductivity increased from 31.8 to 35.9 mS/cm in the experiment on CMR1, whereas for the experiment on CMR4 conductivity decreased from 28.3 to 26.3 mS/cm. These changes in measured conductivities are opposite to the weak trends possibility observed in their corresponding permeabilities. The pH values remained the same (5.5) during both the experiments of CMR1 and CMR4.

Effluent brine chemistries of samples taken after every flow cycle (i.e., after all brine in the upstream accumulator has flowed through the sample into the downstream accumulator, the flow direction has been reversed, then the brine has flowed back into the upstream accumulator – a cycle that generally took 3 to 4 days to complete) during permeability testing are also shown in Table 4.7. The observed initial drop in salt concentrations is likely because significant precipitation occurred in the tubing between the syringe pumps and the test cell, because this tubing was not heated and the brine cooled significantly as it flowed from the pumps to the cell. Salt precipitation was observed in the accumulator and the tubing after the experiments on both samples. As such, the actual brine salinity was lower than intended; to interpret meaningful trends (if present), the initial concentrations should be ignored. To overcome this problem in the future, all components of the experiment should be placed inside a temperature controlled chamber, or the accumulator should be heated and the tubing should be insulated to better maintain the desired temperature.

It seems there was oxidation of pyrite in the rock samples when they interacted with the brine, resulting in slight increases of SO_4 and Fe in the effluents. The oxidation of pyrite also caused the reduction in pH (production of H^+) from an initial value and might have resulted in the further dissolution of carbonate minerals such as calcite and dolomite in the rock samples, resulting in the observed slight increase in Ca and Mg in the effluent. Dissolution of dolomite produced an increase in Ca^{2+} and Mg^{2+} ions in the effluent samples and precipitation of calcite decreased Ca^{2+} and CO_3^{-2} ions in the effluent samples or the net increase or decrease of both of these ions.

In Table 4.7, in the first few days of CMR1 reaction with Brine (I), calcium actually decreased but over the next few days, it increased. These increases and decreases of ions are observed in the effluent samples but they are not reaching a steady state value. Therefore it can be concluded that the system had not yet reached its equilibrium state and it needed more time to reach equilibrium. Hence it is always better to collect many data points with longer reaction time. The fluctuations of major ion concentrations in the effluent samples are shown in Figures 4.11 to 4.14.

The following are the observations made from chemical analysis of effluent data:

1. In some ions (e.g., SO_4^{-2}, Na^{+1}, K^{+1}, Mg^{2+}, Cz^{+1}, Ba^{2+}, Sr^{+2}, Fe^{2+}, Mn^{+2} and Li^{+1}), there is a decreasing trend in concentration for the first few days and then increasing trend in the next days.
2. Silicon and chloride contents are found to be continuously increasing.

The most probable reason for these changes in ion concentrations is that these ions have not yet attained equilibrium between ions present in the rock and those of the brine solution. To achieve equilibrium, more time is required for ions to move from rock to brine solution or vice versa. Therefore, there should be longer tests completed to get more reliable results to make predictions.

The Calmar caprocks studied in this research work are composed mostly of carbonate minerals, whereas most shales caprocks are typically dominated by clay silicate minerals. Clay silicate minerals are present but are minor components in the Calmar caprocks. Therefore, the experimental results on the hebaviour of silicate minerals established in this study could be extrapolated to typical shales and could have broader implications, although additional experiments of fractured permeability with clay-rich caprock/shales are needed to confirm these effluent sample results.

In particular, the clay silicate minerals such as illite and chlorite appear to act quite differently in acidic and alkaline solutions. Acids solutions cause interlayer hydration with illite and effect would be enhanced by the presence of high-hydration cations (Ca^{2+}, Mg^{2+}) in acid solution. Swelling and/or detachment are evident possibilities with permeability reduction in result. Strongly alkaline solutions attack illite at least as effectively as acids, even though seemingly by quite a different mechanism that requires further research to unravel (Hughes et al., 1989).

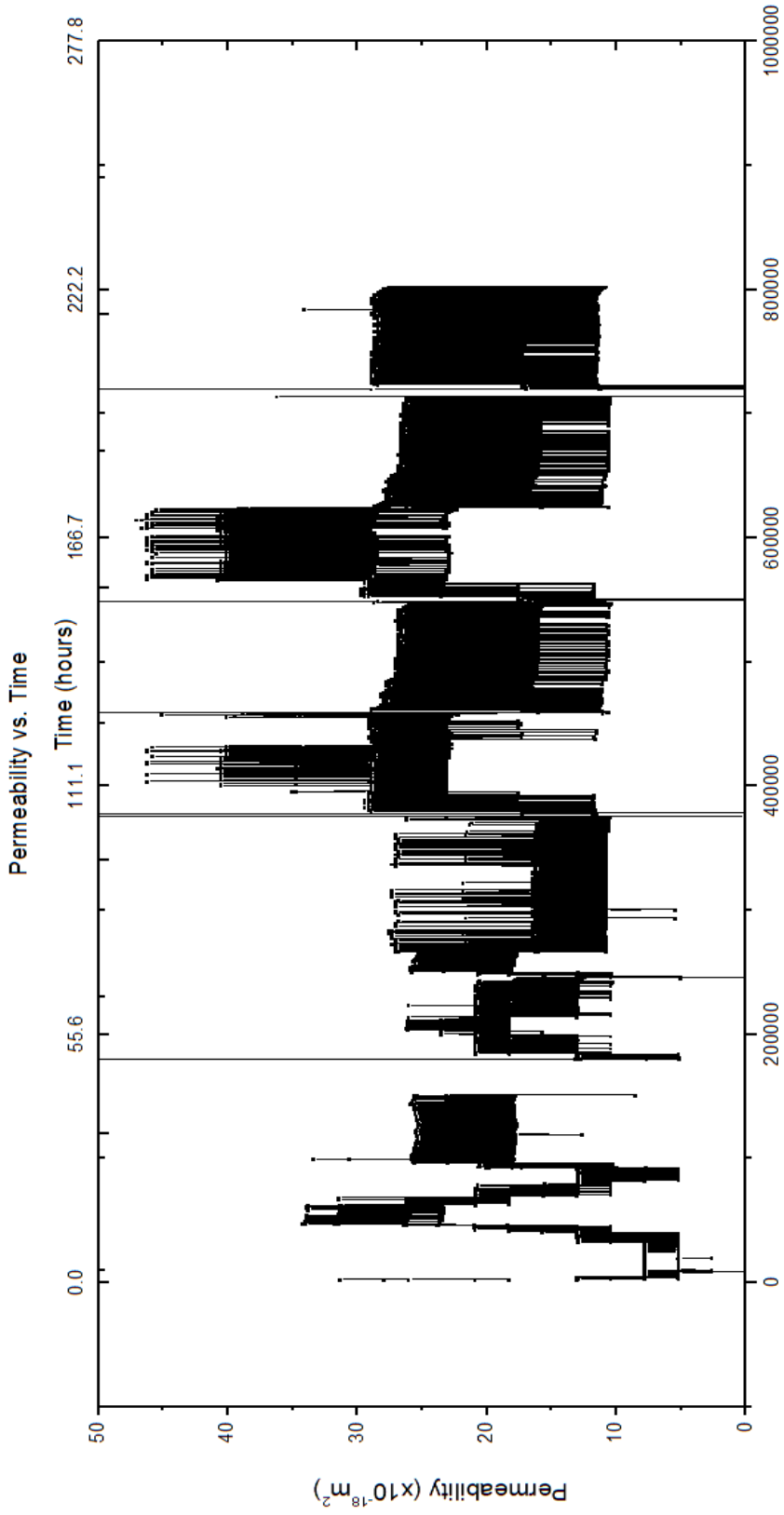

Figure 4.11. Permeability testing results for fractured sample CMR1.

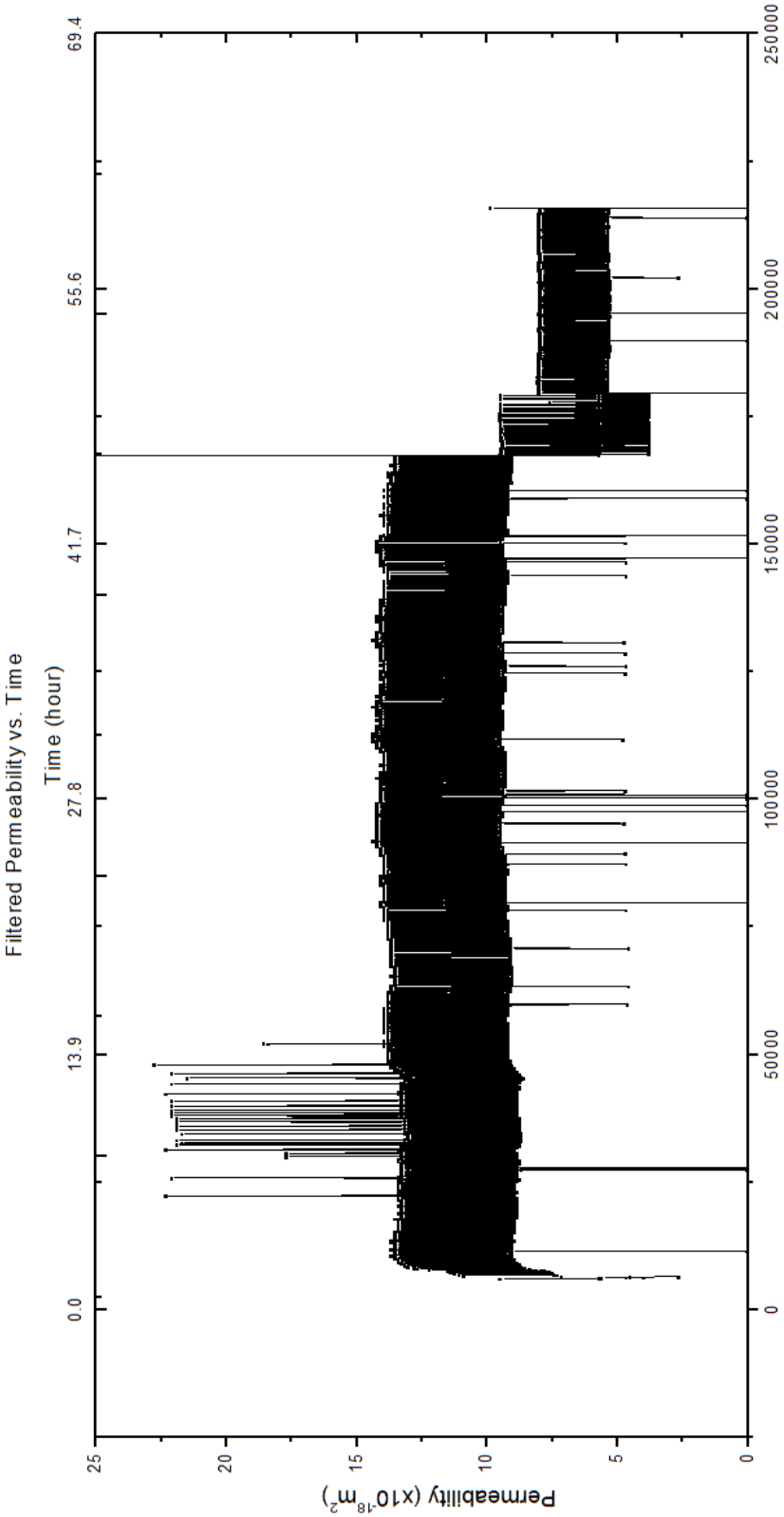

Figure 4.12. Permeability testing results for fractured sample CMR4.

Table 4.8. Effluent brine chemical compositions after every flow cycle during permeability testing of fractured samples CMR1 and CMR4[1]**.**

Analyzed Parameter	Brine (I)	Parameters of CMR1 after interaction with brine (I)			Brine (II)	Parameters of CMR4 after interaction with brine (II)		
		1st cycle	2nd cycle	3rd cycle		1st cycle	2nd cycle	3rd cycle
EC (mS/cm)	206	31.8	35.6	35.9	192.7	28.3	28.5	26.2
ΔEC (mS/cm)		-174.2	3.8	0.3		-164.4	0.2	-2.3
pH	6.1	5.6	5.6	5.6	6.4	5.6	5.6	5.6
ΔpH		-0.5	0	0		-0.8	0	0
RW (ohm-m)	0.05	0.31	0.28	0.28	0.05	0.35	0.35	0.38
ΔRW (ohm-m)		0.26	-0.03	0		0.3	0	0.03
Cl (mg/L)	116090.4	11284.3	12340.9	12575.5	108703.7	9850.6	9349.8	8217.7
ΔCl (mg/L)		-104806	1056.6	234.6		98853.1	-500.8	-1132.1
SO4 (mg/L)	1022.2	91.3	87.7	102.9	978.3	87.4	89.3	74.9
ΔSO4 (mg/L)		-930.9	-3.6	15.2		-890.9	1.9	-14.4
Na (mg/L)	54829.6	5924.2	3279.9	5622.8	54438.9	4645.9	4951.9	4868.3
ΔNa (mg/L)		-48905.4	-2644.3	2342.9		-49793	306	-83.6
K (mg/L)	3896.1	421.6	231.5	352.6	3862.3	335.6	314	348.3
ΔK (mg/L)		-3474.5	-190.1	121.1		-3526.7	-21.6	34.3
Mg (mg/L)	2347.7	271.7	142.4	237.4	7047.9	567.5	630.2	606.4
ΔMg (mg/L)		-2076	-129.3	95		-6480.4	62.7	-23.8
Ca (mg/L)	13031.2	1505.4	912.3	1470.1	640.9	72.8	89.3	83.4
ΔCa (mg/L)		-11525.8	-593.1	557.8		-568.1	16.5	-5.9
Ba (mg/L)	0.02	0.03	0.02	0.05	0.01	0.01	0.01	0.01
ΔBa (mg/L)		0.01	-0.01	0.03		0	0	0
Sr (mg/L)	1006.3	90.2	51.9	84	493.4	46.5	50.9	49.4
ΔSr (mg/L)		-916.1	-38.3	32.1		-446.9	4.4	-1.5
Fe (mg/L)	ND	5.7	4.7	10.7	ND	9.3	11.3	11.6
ΔFe (mg/L)		5.7	-1	6		9.3	2	0.3
Mn (mg/L)	0.03	0.1	0.07	0.13	0.13	0.06	0.08	0.08
ΔMn (mg/L)		0.07	-0.03	0.06		-0.07	0.02	0
Si (mg/L)	ND	0.41	0.46	0.6	ND	0.35	0.36	0.4
ΔSi (mg/L)		0.41	0.05	0.14		0.35	0.01	0.04
Li (mg/L)	0.11	0.02	0.01	0.06	0.03	0.02	0.05	0.04
ΔLi (mg/L)		-0.09	-0.01	0.05		-0.01	0.03	-0.01
TDS (mg/L)	191217.2	19498.5	16994.7	20361.3	175672	15559.8	15424.5	14199
ΔTDS (mg/L)		-171719	-2503.8	3366.6		-160112	-135.3	-1225.5

[1] Effluent brine samples taken after every flow cycle during fractured permeability testing. The observed initial drop in salt concentrations is likely because tubing was not heated, hence salts precipitated in the tubing. ND = Not detected.

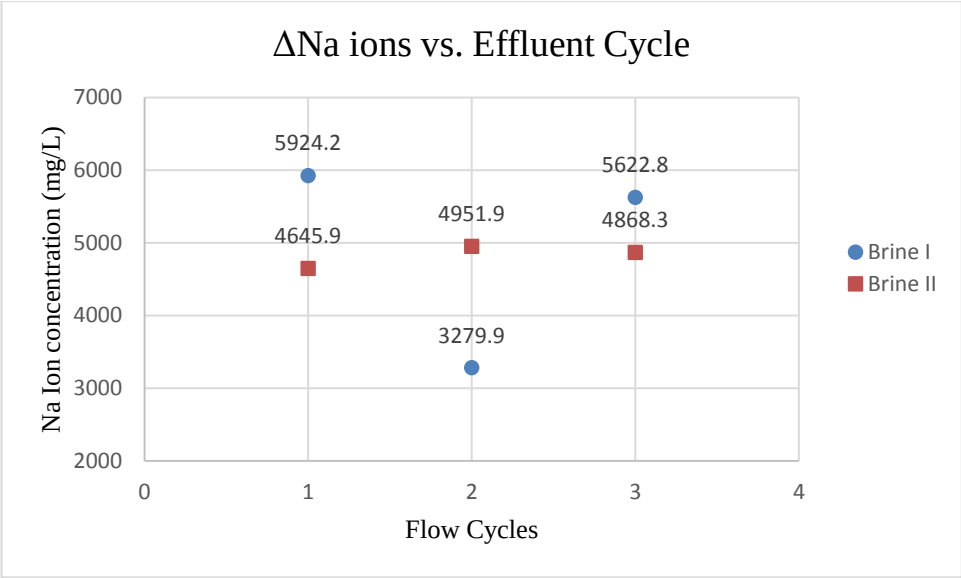

Figure 4.13. Na ion concentrations measured in effluent samples taken after each flow cycle. Brine I was used for sample CMR4; Brine II was used for sample CMR1.

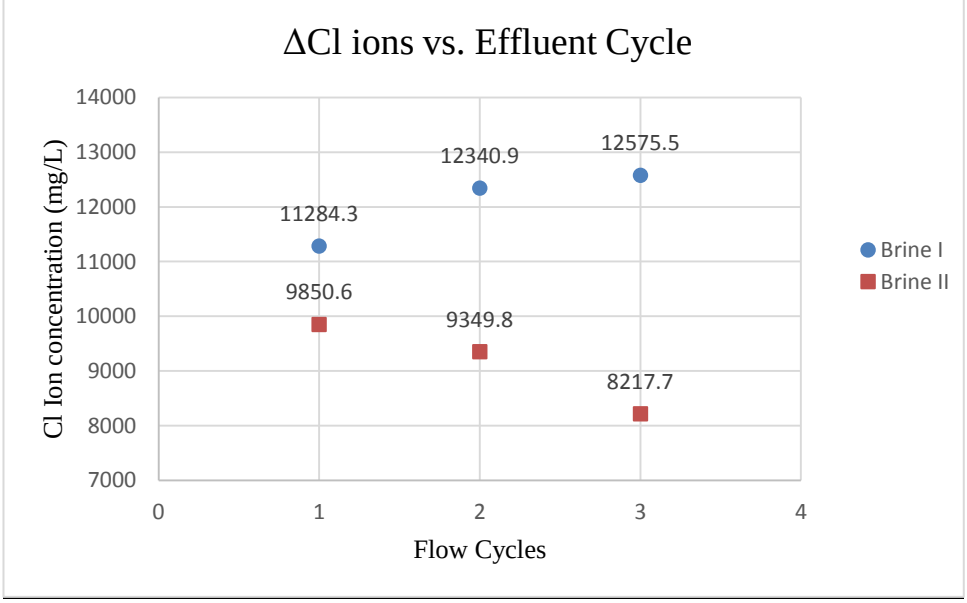

Figure 4.14. Cl ion concentrations measured in effluent samples taken after each flow cycle. Brine I was used for sample CMR4; Brine II was used for sample CMR1.

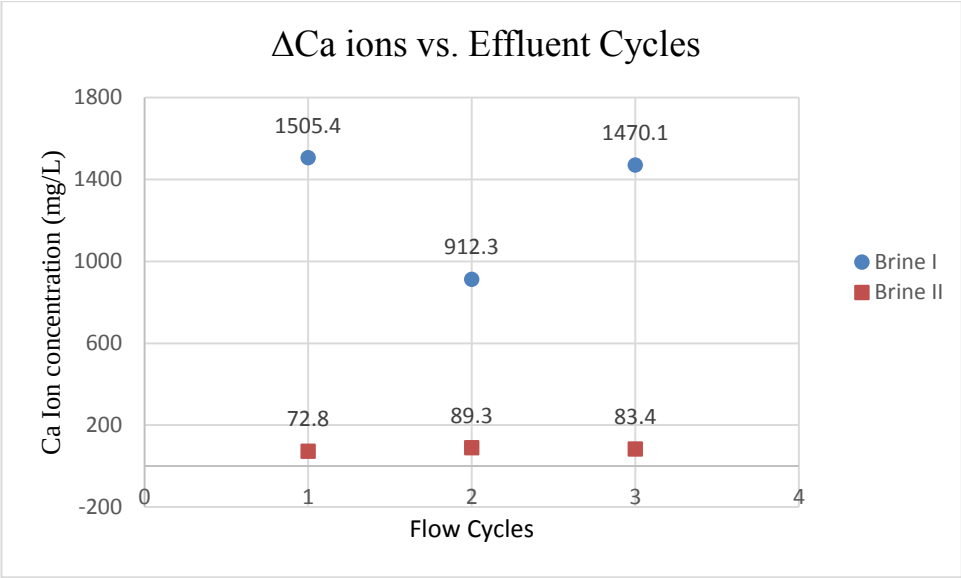

Figure 4.15. Ca ion concentrations measured in effluent samples taken after each flow cycle. Brine I was used for sample CMR4; Brine II was used for sample CMR1

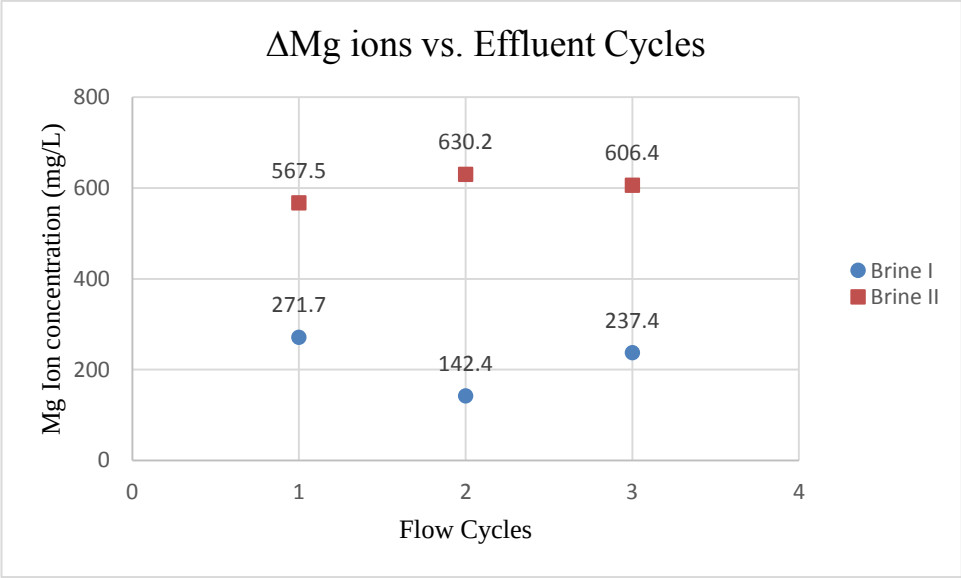

Figure 4.16. Mg ion concentrations measured in effluent samples taken after each flow cycle. Brine I was used for sample CMR4; Brine II was used for sample CMR1.

4.7 Fracture Surface Profiling

The author used a laser profilometer to digitize the topography of the fracture surfaces for sample CMR1 and CMR4 before and after exposure to two brines I and II during permeability experiments. There were no noticeable differences in surface topography. One of the challenges was to get the exact same position for samples and holder before and after for profiling the sample which was not easy to get accurately. This could be due to the fact that the bottom of the laser was not exactly parallel to the base of sample holder which could have produced 1-2 mm error in the laser beam and profile measurements. The outcome of the profiling of two adjacent fractured surfaces of CMR1 and CMR4 (one before interaction (purple) and other after interaction with brines (green)) are given in Figure 4.13.

The major issue with this profiling method is that the two surfaces (before and after interaction with brine) overlap at many places with each other, making it difficult to precisely compare the two surfaces to know changes in the surface through these images. Therefore, better profiling techniques should be used for similar experiments in the future.

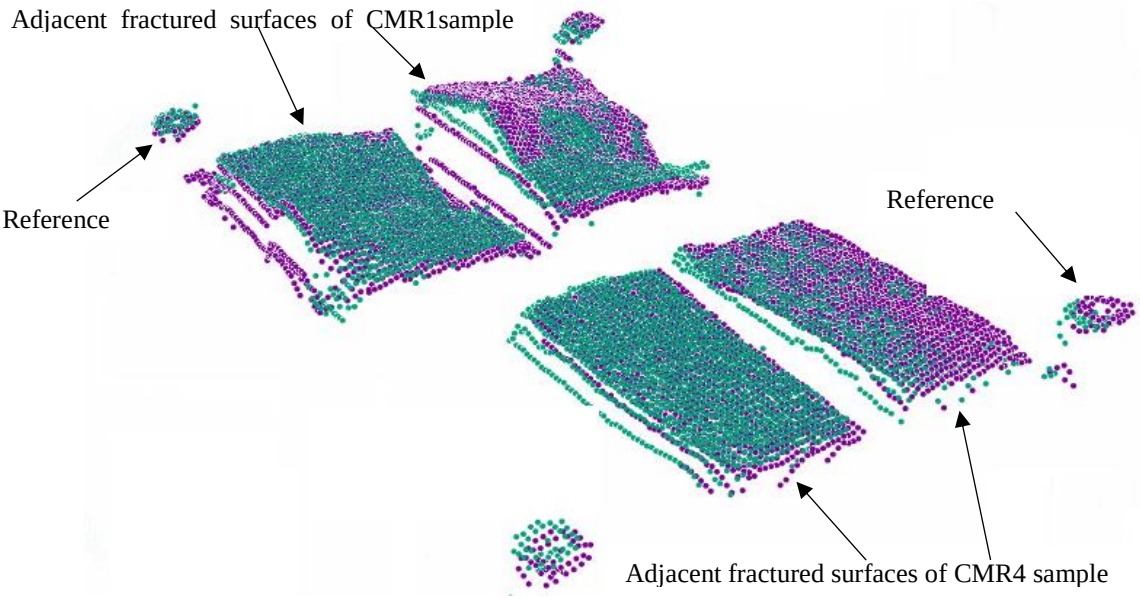

Figure 4.17. Two surface profiles, one before interaction (purple) and other after interaction (green) with brine through fractures of CMR1 and CMR4 are shown.

4.8 Estimation of In-situ Leakage Rates

To generate rough estimates of potential leakage rates of CO_2 through the caprock at the Project Pioneer site, calculations were conducted assuming steady-state, single-phase flow. A uniform caprock thickness of 43 m was assumed, and caprock permeability was assumed to be constant through the entire thickness of the reservoir. Under such conditions, the leakage rate can be calculated based on Darcy's law by re-arranging equation 2.1 as follows:

$$Q = \frac{k \cdot A \cdot \Delta P}{\mu \cdot L} \tag{2.1}$$

Where:

Q = fluid flow rate at steady-state condition in $m^3 \cdot s^{-1}$

k = intrinsic permeability of caprock in m^2

μ = fluid viscosity = $83.85 \cdot 10^{-6}$ Pa·s (http://www.peacesoftware.de)

L = length of flow path = 43 m

A = area (in plane view) covered by CO_2 plume (350 m radius) = $\pi \times (350)^2$

= 384845 m^2

ΔP = pressure drop from base to top of caprock; upper-bound scenario = reservoir fracture pressure – native pore pressure above caprock

= 40 MPa – 17 MPa = 23 MPa = $23 \cdot 10^6$ Pa.

Using this approach, leakage rates for two scenarios were considered: (1) Intact caprock; and (2) caprock in which a tensile fracture extending the full height of the caprock has been created, which extends (laterally) across the full extent of the CO_2 plume.

4.8.1 Intact Caprock Leakage

For this scenario, permeability (k) has a value of $3.03 \cdot 10^{-22}$ m^2 (~ 0.3 nd), based on intact rock permeability reported in section 4.5. The resultant leakage rate is calculated using equation 4.1, as follows:

$$Q = \frac{3.03 \cdot 10^{-22} \text{m}^2 \cdot 384845 \text{ m}^2 \cdot 23 \cdot 10^6 \text{Pa}}{83.85 \cdot 10^{-6} \text{Pa·s} \cdot 43 \text{ m}}$$

$$Q = 7.44 \cdot 10^{-7} \text{ m}^3 \cdot \text{s}^{-1}$$

At this leakage rate, approximately 990 tonnes would leak through the intact caprock after 50 years of injection of CO_2 (which represents 0. 002% of the 50 Mt total injection over this time interval).

4.8.2 Fractured Caprock Leakage

For this scenario, permeability (k) has a value of $7.77 \cdot 10^{-18}$ (~ 7.8 μd), based on fractured rock permeability reported in section 4.6. The resultant leakage rate is calculated using equation 4.1, as follows:

$$Q = \frac{7.8 \cdot 10^{-18}\text{m}^2 \cdot 384845\ \text{m}^2 \cdot 23 \cdot 10^6\ \text{Pa}}{83.85 \cdot 10^{-6}\text{Pa·s} \cdot 43\ \text{m}}$$

$$Q = 1.91\ \cdot 10^{-2}\ \text{m}^3\text{·s}^{-1}$$

At this leakage rate, approximately 25.8 Mt would leak through the fractured caprock after 50 years of injection of CO_2 (which represents 51.6 % of the 50 Mt total injection over this time interval).Though this represents an unacceptable leakage rate, it is important to consider that this calculation represents an extreme situation, for several reasons: (1) This calculation assumes that the fracture transects the full thickness of the caprock, whereas numerical simulations conducted by Goodarzi and Settari (2016) suggest that only the lower portion of the caprock would fracture; (2) pore pressure in the reservoir would drop below 40 MPa (the assumed, constant rate in this calculation) as leakage occurred; (3) leakage rates under transient conditions will be lower than those calculated for steady-state conditions, during the early stages of leakage – at least; and (4) effective permeability to CO_2 under 2-phase flow conditions will be lower than the intrinsic permeability (single-phase flow) used in these calculations Nevertheless, these calculations do suggest the potential for significant leakage rates, if caprock fracturing is not mitigated during injection.

5. CONCLUSION

The Project Pioneer site was previously chosen for CO_2 storage in the Wabamun area of Alberta. Caprock integrity at the site (i.e., the effectiveness of the primary seal) was investigated in this research. This study determined the mineralogical and chemical composition, along with thermal properties, of the caprock and saline formation. These measurements are key factors in determining the effectiveness of storage of CO_2.

The average mineralogical composition of four Calmar samples analyzed during this research was found to be 34 % quartz, 22 % calcite, and 12 % dolomite k-spar, 2.7% albite, and 1.5% pyrite. For the Nisku saline Formation, the composition reported in the literature is mostly dolomite (up to 91.6%), with a small quantity of calcite (up to 15.2%). The thermal properties measured during this research were thermal conductivity, thermal diffusivity, the heat capacity per unit volume and linear thermal expansion coefficient. Values measured for the Calmar were 3.69 **(**$W \cdot m^{-1} \cdot {}^{\circ}C^{-1}$), 1.87 ($mm^2 \cdot sec^{-1}$), 2.19 ($MJ \cdot m^{-3} \cdot {}^{\circ}C^{-1}$) and 5.03 ($\mu\xi \cdot {}^{\circ}C^{-1}$), and for the Nisku were 4.11 ($W \cdot m^{-1} \cdot {}^{\circ}C^{-1}$), 1.63 ($mm^2 \cdot sec^{-1}$), 3.70 ($MJ \cdot m^{-3} \cdot {}^{\circ}C^{-1}$) and 3.70 ($\mu\xi \cdot {}^{\circ}C^{-1}$) respectively.

The injection of relatively cold (approximately 30 ˚C) CO_2 in the Nisku saline Formation (below or at fracture pressure) is likely to cause only negligible surface heave, which is not likely to have any environmental impact due to surface deformations. To estimate deformation in the reservoir and surface uplift due to change in reservoir temperature and pressure, the measured thermal data, including conductivity, thermal diffusivity, the heat capacity per unit volume and linear thermal expansion coefficient have been used in the geomechanical model. The reservoir expansion (ΔH) ~ 1.4 mm and surface uplift (S) ~ 1.77 mm were estimated using simple analytical and numerical models in this research.

It is seen that relatively cold injection of CO_2 in the storage formation will reduce the fracture pressure significantly and produce a tensile fracture in the reservoir and caprock. This reduction in fracturing pressure decreases the pressure differential available for injection, and therefore injectivity. The variation of fracture pressure under injection condition can be determined using geomechanicaly model and its minimum value should be taken as the maximum operating pressure.

A testing system was developed in this research to provide a suitable means of measuring permeabilities of tight rocks, such as caprock; however, the system is extremely sensitive to small temperature fluctuations which could affect the fluid composition through salt precipitation. Modifications required are described in the Section 6 (Recommendations).

The permeability of intact rock samples was measured using a pressure pulse decay technique which resulted in a value of 0.3nd ($0.3 \cdot 10^{-21}$ m^2). The permeability estimated on fractured caprock samples ranged between 10 to 40 µd ($10 \cdot 10^{-18}$ to $40 \cdot 10^{-18}$ m^2). In permeability experiments, two types of pore water compositions were used. One representing the native Nisku saline reservoir brine before CO_2 injection to test its effect on sample CMR1 and the other representing the predicted composition after 50 years of injection to test its effect on sample CMR4. The change in permeability as a function of time for these two samples (CMR1 and CMR4) was not significant during tests, and their values remained in the same range of micro darcys.

Using chemical analysis data collected on different samples taken during permeability testing of fractured samples, it can be concluded that the ions have not yet attained equilibrium. In reaching equilibrium, some ions may move from the rock to brine solution or vice versa and that could be the reason for slight increase and decrease of ions in effluent samples. Also, the laboratory investigation of matrix reactivity enabled the prediction of the effects of geochemical and geomechanical (thermoelastic) processes on caprock samples.

It is concluded that Calmar caprock at the Project Pioneer site should serve as an effective seal if caprock fracturing is mitigating, which in turn requires that the effects of thermally-induced stresses on fracturing pressures are taken into account.

6. RECOMMENDATIONS

The following is a list of recommendations based on this study:

- When conducting pressure-pulse decay permeability experiments of intact samples, and permeability experiments of fractured samples, every effort should be made to reduce temperature fluctuations.
- Permeability testing of fractured samples was only three weeks long because samples had to return to the client. In the future, testing should run for longer periods. For example, the testing in this study ideally would have been run for three to four months.
- SEM and EDS analyses of the samples should be taken before and after the every permeability test on fractured samples to measure and quantify possible changes in mineralogy.
- To avoid precipitation of salts in the tubing during permeability testing, it is highly recommended to put all components inside a temperature controlled environment. In this study, the tubing was exposed to room temperature.
- The effluent sample should be analyzed immediately after testing is complete. This is to help in decision making regarding further testing or to make changes to the experimental set-up.
- In this study, only three fluid flow samples were collected for each CMR1 and CMR4 after each cycle of passing fluid through fractured surfaces of these samples (it was approximately one week long in this study). In future testing, the number of collected effluent samples should increase along with the duration of testing. This may show a clear equilibrium trend in analyzed ions.
- The measured surface deformations could be used in conjunction with the knowledge of mechanical properties to back calculate deformations of the Nisku Formation. It can help to plan for the location of the instrumentation and surface monitoring.
- Further investigations and developments at the Project Pioneer site are recommended if economics are favourable because the site is technically viable option.

REFERENCES

ANDREANI, M., GOUZE, P., LUQUOT, L. & JOUANNA, P. 2008a. Changes in seal capacity of fractured claystone caprocks induced by dissolved and gaseous CO2 seepage. *Geophysical Research Letters,* 35.

ANDREANI, M., GOUZE, P., LUQUOT, L. & JOUANNA, P. 2008b. Changes in seal capacity of fractured claystone caprocks induced by dissolved and gaseous CO2 seepage. *Geophysical Research Letters,* 35**,** n/a-n/a.

ASTM D3967-08. 2008. Standard test method for splitting tensile strength of intact rock core specimens, ASTM, Philadelphia, Pennsylvania, USA.

BACHU, S. 2008. CO2 storage in geological media: Role, means, status and barriers to deployment. *Progress in Energy and Combustion Science,* 34**,** 254-273.

BACHU, S. & STEWART, S. 2002. Geological Sequestration of Anthropogenic Carbon Dioxide in the Western Canada Sedimentary Basin: Suitability Analysis.

BATEMAN, K., TURNER, G., PEARCE, J., NOY, D., BIRCHALL, D. & ROCHELLE, C. 2005. Large-scale column experiment: study of CO2, porewater, rock reactions and model test case. *Oil & Gas Science and Technology,* 60**,** 161-175.

BERGMAN, P. D. & WINTER, E. M. 1995. Disposal of carbon dioxide in reservoir in the U.S. *Energy Conversion and Management,* 36**,** 523-526.

BERKOWITZ, B. 2002. Characterizing flow and transport in fractured geological media: A review. *Advances in water resources,* 25**,** 861-884.

BOSSIE-CODREANU, D. 2008. The CO2-EOR sequestration equation: recovery, dynamic monitoring, and co-optimization. *First Break* 26.

BRACE, W.F., WALSH, J.B., FRANGOS, W.T. 1968. Permeability of granite under high pressure. Journal of Geophysical Research, 73(6): 2225-2236.

BROWN, S., CAPRIHAN, A. & HARDY, R. 1998. Experimental observation of fluid flow channels in a single fracture. *Journal of Geophysical Research: Solid Earth,* 103**,** 5125-5132.

BRUANT, R. G., JR., GUSWA, A. J., CELIA, M. A. & PETERS, C. A. 2002. Safe storage of CO2 in deep saline reservoir. *Environ Sci Technol,* 36**,** 240a-245a.

BRUNO, M. S. 1992. Subsidence-Induced Well Failure. Society of Petroleum Engineers.

BUSCH, A., ALLES, S., GENSTERBLUM, Y., PRINZ, D., DEWHURST, D. N., RAVEN, M. D., STANJEK, H. & KROOSS, B. M. 2008. Carbon dioxide storage potential of shales. *International Journal of Greenhouse Gas Control,* 2**,** 297-308.

CAVANAGH, A. & RINGROSE, P. 2011. Simulation of CO2 distribution at the In Salah storage site using high-resolution field-scale models. *Energy Procedia,* 4**,** 3730-3737.

CELIA, M. A. & NORDBOTTEN, J. M. 2009. Practical modeling approaches for geological storage of carbon dioxide. *Groundwater,* 47**,** 627-638.

CHAN, A. W. & ZOBACK, M. D. 2007. The role of hydrocarbon production on land subsidence and fault reactivation in the Louisiana coastal zone. *Journal of Coastal Research***,** 771-786.

CHIQUET, P., BROSETA, D. & THIBEAU, S. 2007. Wettability alteration of caprock minerals by carbon dioxide. *Geofluids,* 7**,** 112-122.

CLAUSER, C. & HUENGES, E. 2013. Thermal conductivity of rocks and minerals. *Rock physics & phase relations: a handbook of physical constants***,** 105126.

COLLIEU, A. M., POWNEY, D., GIRIFALCO, L. & HERMAN, H. 1975. The mechanical and thermal properties of materials and statistical physics of materials. *Physics Today,* 28**,** 51.

COOPER, H. & SIMMONS, G. 1977. The effect of cracks on the thermal expansion of rocks. *Earth and Planetary Science Letters,* 36**,** 404-412.

CÔTÉ, J. & KONRAD, J.-M. 2005. A generalized thermal conductivity model for soils and construction materials. *Canadian Geotechnical Journal,* 42**,** 443-458.

DAKE, L. 1978. *Fundamentals of Reservoir Engineering." Developments in Petroleum Science.* , Elsevier Scientiflc Publishing Company.

DAMEN, K., FAAIJ, A. & TURKENBURG, W. 2006. Health, safety and environmental risks of underground CO 2 storage–overview of mechanisms and current knowledge. *Climatic Change,* 74**,** 289-318.

DAVISON, J. 2007. Performance and costs of power plants with capture and storage of CO2. *Energy,* 32**,** 1163-1176.

DETWILER, R. L. 2010. Permeability alteration due to mineral dissolution in partially saturated fractures. *Journal of Geophysical Research: Solid Earth,* 115.

DICKER, A. & SMITS, R. 1988. A practical approach for determining permeability from laboratory pressure-pulse decay measurements. International Meeting on Petroleum Engineering, 1988a. Society of Petroleum Engineers.

DICKER, A. I. & SMITS, R. M. 1988b. A Practical Approach for Determining Permeability From Laboratory Pressure-Pulse Decay Measurements. Society of Petroleum Engineers.

DIJK, P. E., BERKOWITZ, B. & YECHIELI, Y. 2002. Measurement and analysis of dissolution patterns in rock fractures. *Water resources research,* 38.

DOVE, P. M. & CRERAR, D. A. 1990. Kinetics of quartz dissolution in electrolyte solutions using a hydrothermal mixed flow reactor. *Geochimica et Cosmochimica Acta,* 54**,** 955-969.

DU, J. & OLSON, J. E. 2001. A poroelastic reservoir model for predicting subsidence and mapping subsurface pressure fronts. *Journal of Petroleum Science and Engineering,* 30**,** 181-197.

DUAN, Z., SUN, R., ZHU, C. & CHOU, I. M. 2006. An improved model for the calculation of CO2 solubility in aqueous solutions containing Na+, K+, Ca2+, Mg2+, Cl−, and SO42−. *Marine Chemistry,* 98**,** 131-139.

DUSSEAULT, M. B., BRUNO, M. S. & BARRERA, J. 2002. Casing Shear: Causes, Cases, Cures.

EISINGER, C. J., J. 2011. Reservoir Characterization for CO2 Sequestration: Assessing the Potential of the Devonian Carbonate Nisku Formation of Central Alberta. *Oil Gas Sci. Technol. – Rev. IFP Energies nouvelles,* 66**,** 47-65.

EISINGER, C. L. & JENSEN, J. L. 2009. Data integration, petrophysics, and geomodelling, Wabamun Area CO2 Sequestration Project (WASP). Energy and Environmental System Group internal report, 2009.

ELLIS, B., PETERS, C., FITTS, J., BROMHAL, G., MCINTYRE, D., WARZINSKI, R. & ROSENBAUM, E. 2011. Deterioration of a fractured carbonate caprock exposed to CO2-acidified brine flow. *Greenhouse Gases: Science and Technology,* 1**,** 248-260.

ELLIS, B. R., CRANDELL, L. E. & PETERS, C. A. 2010. Limitations for brine acidification due to SO 2 co-injection in geologic carbon sequestration. *International Journal of Greenhouse Gas Control,* 4**,** 575-582.

EMBERLEY, S., HUTCHEON, I., SHEVALIER, M., DUROCHER, K., MAYER, B., GUNTER, W. & PERKINS, E. 2005. Monitoring of fluid– rock interaction and CO 2 storage through produced fluid sampling at the Weyburn CO 2-injection enhanced oil recovery site, Saskatchewan, Canada. *Applied Geochemistry,* 20**,** 1131-1157.

ENNIS-KING, J. & PATERSON, L. 2002. Engineering Aspects of Geological Sequestration of Carbon Dioxide. Society of Petroleum Engineers.

FALKOWSKI, P., SCHOLES, R. J., BOYLE, E., CANADELL, J., CANFIELD, D., ELSER, J., GRUBER, N., HIBBARD, K., HOGBERG, P., LINDER, S., MACKENZIE, F. T., MOORE, B., 3RD, PEDERSEN, T., ROSENTHAL, Y., SEITZINGER, S., SMETACEK, V. & STEFFEN, W. 2000. The global carbon cycle: a test of our knowledge of earth as a system. *Science,* 290**,** 291-6.

FAROKHPOOR, R., BJØRKVIK, B. J. A., LINDEBERG, E. & TORSÆTER, O. 2013. CO2 Wettability Behavior During CO2 Sequestration in Saline Reservoir -An Experimental Study on Minerals Representing Sandstone and Carbonate. *Energy Procedia,* 37**,** 5339-5351.

FENG, X., SUN, C., ZHANG, X. & ANSARI, F. 2010. Determination of the coefficient of thermal expansion with embedded long-gauge fiber optic sensors. *Measurement Science and Technology,* 21**,** 065302.

FINE, R. A. & MILLERO, F. J. 1973. Compressibility of water as a function of temperature and pressure. *The Journal of Chemical Physics,* 59**,** 55295536.

FJÆR, E. 1999. Static and dynamic moduli of weak sandstones.

FLIN, D. Can sequestration help industry beat pollution? IEE Power Engineer, October/November, 25-28., 2004.

FOX, J. N. 1990. Measurement of thermal expansion coefficients using a strain gauge. *American Journal of Physics,* 58**,** 875-877.

GAUS, I., AUDIGANE, P., ANDRÉ, L., LIONS, J., JACQUEMET, N., DURST, P., CZERNICHOWSKI-LAURIOL, I. & AZAROUAL, M.

2008. Geochemical and solute transport modelling for CO2 storage, what to expect from it? *International Journal of Greenhouse Gas Control,* 2**,** 605-625.

GEERTSMA, J. 1957. The Effect of Fluid Pressure Decline on Volumetric Changes of Porous Rocks.

GHADERI, S., LEONENKO, Y., 2009. Reservoir Modeling Wabamun Area CO2 Sequestration project (WASP). Energy and Environmental Systems Group Institute for Sustainable energy, environment and economy (ISEEE), University of Calgary, Calgary, AB, Canada.

GOODARZI, S. & SETTARI, A. 2016. CO2 Storage in the Nisku Reservoir in the Wabamun Lake Area, Canada - The Effect of Site Characterization Data on Caprock Integrity Modeling. Society of Petroleum Engineers.

GOODARZI, S., SETTARI, A. & KEITH, D. 2012. Geomechanical modeling for CO2 storage in Nisku reservoir in Wabamun Lake area in Canada. *International Journal of Greenhouse Gas Control,* 10**,** 113-122.

GOULTY, N. 2003. Reservoir stress path during depletion of Norwegian chalk oilfields. *Petroleum Geoscience,* 9**,** 233-241.

GOUZE, P., NOIRIEL, C., BRUDERER, C., LOGGIA, D. & LEPROVOST, R. 2003a. X-ray tomography characterization of fracture surfaces during dissolution. *Geophysical Research Letters,* 30**,** n/a-n/a.

GOUZE, P., NOIRIEL, C., BRUDERER, C., LOGGIA, D. & LEPROVOST, R. 2003b. X- ray tomography characterization of fracture surfaces during dissolution. *Geophysical Research Letters,* 30.

GRIMES, C. E., KESTIN, J. & EZZAT KHALIFA, H. 1979. Viscosity of aqueous KCl solutions in the temperature range 25 to 150/sup 0/C and the pressure range 0 to 30 MPa. *J. Chem. Eng. Data;(United States),* 24.

GUNTER, W. D., BACHU, S. & BENSON, S. 2004. The role of hydrogeological and geochemical trapping in sedimentary basins for secure geological storage of carbon dioxide. *Geological Society, London, Special Publications,* 233**,** 129-145.

GUNTER, W. D., BACHU, S., LAW, D. H. S., MARWAHA, V., DRYSDALE, D. L., MACDONALD, D. E. & MCCANN, T. J. 1996. Technical and economic feasibility of CO2 disposal in reservoir within the Alberta sedimentary basin, Canada. *Energy Conversion and Management,* 37**,** 1135-1142.

GUNTER, W. D., PERKINS, E. H. & HUTCHEON, I. 2000. Reservoir disposal of acid gases: modelling of water–rock reactions for trapping of acid wastes. *Applied Geochemistry,* 15**,** 1085-1095.

GUREVICH, A. E. & CHILINGARIAN, G. V. 1993. Subsidence over producing oil and gas fields, and gas leakage to the surface. *Journal of Petroleum Science and Engineering,* 9**,** 239-250.

GUSTAFSSON, S. E. 1991. Transient plane source techniques for thermal conductivity and thermal diffusivity measurements of solid materials. *Review of Scientific Instruments,* 62**,** 797-804.

HANGX, S., BAKKER, E., BERTIER, P., NOVER, G. & BUSCH, A. 2015. Chemical–mechanical coupling observed for depleted oil reservoirs subjected to long-term CO2-exposure – A case study of the Werkendam natural CO2 analogue field. *Earth and Planetary Science Letters,* 428**,** 230-242.

HASKETT, S. E., NARAHARA, G. M. & HOLDITCH, S. A. 1988. A Method for Simultaneous Determination of Permeability and Porosity in LowPermeability Cores.

HAWKES, C., MCLELLAN, P., ZIMMER, U. & BACHU, S. 2004. Geomechanical factors affecting geological storage of CO2 in depleted oil and gas reservoirs: risks and mechanisms. Gulf Rocks 2004, the 6th North America Rock Mechanics Symposium (NARMS),. American Rock Mechanics Association.

HENSCHEL, M., SHEN, L., SHIPMAN, T., LEHRBASS, B. & AUBE, G. 2014. Remotely Monitoring of SAGD Operations with Satellite Based InSAR. Society of Petroleum Engineers. Society of Petroleum Engineers.

HEPPLE, R. P. & BENSON, S. M. 2005. Geologic storage of carbon dioxide as a climate change mitigation strategy: performance requirements and the implications of surface seepage. *Environmental Geology,* 47**,** 576-585.

HERMANSEN, H., LANDA, G. H., SYLTE, J. E. & THOMAS, L. K. 2000. Experiences after 10 years of waterflooding the Ekofisk Field, Norway. *Journal of Petroleum Science and Engineering,* 26**,** 11-18.

HICKOX, C., MCVEY, D., MILLER, J., OLSON, L. & SILVA, A. 1986. Thermal conductivity measurements of pacific illite sediment. *International Journal of Thermophysics,* 7**,** 755-764.

HILDENBRAND, A. S., S. SCHLOMER, AND B. M. KROOSS (2002), Gas break-through experiments on fine grained sedimentary rocks, Geofluids, 2(1), 3–23.

HITCHON, B., GUNTER, W. D., GENTZIS, T. & BAILEY, R. T. 1999. Sedimentary basins and greenhouse gases: a serendipitous association. *Energy Conversion and Management,* 40**,** 825-843.

HOLLOWAY, S. 2001. Storage of fossil fuel-derived carbon dioxide beneath the surface of the earth. *Annual Review of Energy and the Environment,* 26**,** 145-166.

HOLT, R., FLORNES, O., LI, L. & FJÆR, E. Consequences Of DepletionInduced Stress Changes On Reservoir Compection And Recovery. Gulf Rocks 2004, the 6th North America Rock Mechanics Symposium (NARMS), 2004. American Rock Mechanics Association.

HUGHES, C. R., DAVEY, R. C. &. CURTIS, C. D., 1989. Chemical reactivity of some reservoir illites; implications for petroleum production. *Clay Minerals*, 24, 445-458.

HUOTARI, T. & KUKKONEN, L. 2004. Thermal fxpansion Properties of

Rocks: literature Survey and fstimation of Thermal fxpansion Coefficient for Olkiluoto Mica Gneiss.

IPCC, I. P. O. C. 2007. IPCC. *Climate change*.

IZGEC, O., DEMIRAL, B., BERTIN, H. & AKIN, S. 2008. CO2 injection into saline carbonate reservoir formations I: laboratory investigation. *Transport in Porous Media,* 72**,** 1-24.

J. ARMITAGE, P., FAULKNER, D., WORDEN, R., C. APLIN, A., BUTCHER, A. & ILIFFE, J. 2011. Experimental measurement of, and controls on, permeability and permeability anisotropy of caprocks from the CO2 storage project at the Krechba Field, Algeria.

JI, L., SETTARI, A., SULLIVAN, R.B., 2006. A new approach to hydraulic fracturing modeling-fully coupled with geomechanical and reservoir simulation. In: SPE 2006, Paper No. 99428, Presented at the SPE Europec/EAGE Annual Conference and Exhibition, 12–15 June 2006, Vienna, Austria.

JONES, S. 1997. A technique for faster pulse-decay permeability measurements in tight rocks. *SPE Formation Evaluation,* 12**,** 19-25.

KASZUBA, J. P., JANECKY, D. R. & SNOW, M. G. 2003. Carbon dioxide reaction processes in a model brine reservoir at 200 C and 200 bars: implications for geologic sequestration of carbon. *Applied Geochemistry,* 18**,** 1065-1080.

KASZUBA, J. P., JANECKY, D. R. & SNOW, M. G. 2005. Experimental evaluation of mixed fluid reactions between supercritical carbon dioxide and NaCl brine: Relevance to the integrity of a geologic carbon repository. *Chemical Geology,* 217**,** 277-293.

KEITH, D. & LAVOIE, R. 2009. Final Report of the Wabamun Area CO2 Sequestration Project (WASP).

https://www.ucalgary.ca/wasp/reports.+

KONING, E. J. L. 1988. Waterflooding under fracturing conditions. Delft Technical University.

KREY, V. & RIAHI, K. 2009. Implications of delayed participation and technology failure for the feasibility, costs, and likelihood of staying below temperature targets—Greenhouse gas mitigation scenarios for the 21st century. *Energy Economics,* 31, Supplement 2**,** S94-S106.

LAGIOS, E., SAKKAS, V., PAPADIMITRIOU, P., PARCHARIDIS, I., DAMIATA, B., CHOUSIANITIS, K. & VASSILOPOULOU, S. 2007. Crustal deformation in the Central Ionian Islands (Greece): results from DGPS and DInSAR analyses (1995–2006). *Tectonophysics,* 444**,** 119-145.

LARSEN, A. 2011. *Laboratory Investigation of the Sealing Properties of the Lea Park Shale with Respect to Carbon Dioxide.* Master.

LE GUEN, Y., RENARD, F., HELLMANN, R., BROSSE, E., COLLOMBET, M., TISSERAND, D. & GRATIER, J. P. 2007. Enhanced deformation of limestone and sandstone in the presence of high fluids. *Journal of Geophysical Research: Solid Earth,* 112.

LENEVEU, D. 2008. CQUESTRA, a risk and performance assessment code for geological sequestration of carbon dioxide. *Energy Conversion and Management,* 49**,** 32-46.

LEWICKI, J. L., BIRKHOLZER, J. & TSANG, C.-F. 2007. Natural and industrial analogues for leakage of CO2 from storage reservoirs: identification of features, events, and processes and lessons learned. *Environmental Geology,* 52**,** 457.

LI, S., DONG, M., LI, Z., HUANG, S., QING, H. & NICKEL, E. 2005. Gas breakthrough pressure for hydrocarbon reservoir seal rocks: implications for the security of long-term CO2 storage in the Weyburn field. *Geofluids,* 5**,** 326-334.

LIU, R., JIANG, Y., LI, B. & WANG, X. 2015. A fractal model for characterizing fluid flow in fractured rock masses based on randomly distributed rock fracture networks. *Computers and Geotechnics,* 65**,** 4555.

LORENZ, J. C., TEUFEL, L. W. & WARPINSKI, N. R. 1991. Regional Fractures I: A Mechanism for the Formation of Regional Fractures at Depth in Flat-Lying Reservoirs (1). *AAPG bulletin*, 75**,** 1714-1737.

LOVE, A. E. H. 1944. *A treatise on the mathematical theory of elasticity*, Dover: New York, NY.

LUFFEL, D., HOPKINS, C. & SCHETTLER JR, P. 1993. Matrix permeability measurement of gas productive shales. SPE Annual Technical Conference and Exhibition. Society of Petroleum Engineers.

LUQUOT, L., ANDREANI, M., GOUZE, P. & CAMPS, P. 2012. CO 2 percolation experiment through chlorite/zeolite-rich sandstone (Pretty Hill Formation–Otway Basin–Australia). *Chemical Geology*, 294**,** 75-88.

LUQUOT, L. & GOUZE, P. 2009. Experimental determination of porosity and permeability changes induced by injection of CO 2 into carbonate rocks. *Chemical Geology*, 265**,** 148-159.

MATERIALS. A. S. F. T. A. 2005. Standard Test Method for Splitting Tensile Strength of Intact Rock Core Specimens. ASTM Standards.

MATHIESON, A., MIDGLEY, J., DODDS, K., WRIGHT, I., RINGROSE, P. & SAOUL, N. 2010. CO 2 sequestration monitoring and verification technologies applied at Krechba, Algeria. *The Leading Edge*, 29**,** 216-222.

MCCOLPIN, G. R. 2009. Surface Deformation Monitoring As a Cost Effective MMV Method. *Energy Procedia*, 1**,** 2079-2086.

MICHAEL, K., BACHU, S., BUSCHKUEHLE, B.E., HAUG, K., GROBE, M., AND LYTVIAK, A.T.,, & . Comprehensive characterization of a potential site for CO2 geological storage in central Alberta, Canada:. Proceedings, CO2SC Symposium,, 2006 Berkeley, California,. 4

MICHAEL, K., BACHU, S., BUSCHKUEHLE, M., HAUG, K., AND S. TALMAN. IN PRESS. 2008. Comprehensive Characterization of a Potential Site for CO2 Geological Storage in Central Alberta, Canada. *AAGP Special Publication on Carbon Dioxide Sequestration*.

MORRIS, J. P., HAO, Y., FOXALL, W. & MCNAB, W. 2011. In salah CO2 storage JIP: hydromechanical simulations of surface uplift due to CO2 injection at in salah. *Energy Procedia,* 4**,** 3269-3275.

MULDERS, F. M. M. 2003. *Modelling of stress development and fault slip in and around a producing gas reservoir.* Ph.D., Delft University of Technology: Netherlands.

NAGEL, N. B. 2001. Compaction and subsidence issues within the petroleum industry: From wilmington to ekofisk and beyond. *Physics and Chemistry of the Earth, Part A: Solid Earth and Geodesy,* 26**,** 3-14.

NOIRIEL, C., BERNARD, D., GOUZE, P. & THIBAULT, X. 2005. Hydraulic properties and microgeometry evolution accompanying limestone dissolution by acidic water. *Oil & gas science and technology,* 60**,** 177192.

NOIRIEL, C., MADÉ, B. & GOUZE, P. 2007a. Impact of coating development on the hydraulic and transport properties in argillaceous limestone fracture. *Water Resources Research,* 43**,** n/a-n/a.

NOIRIEL, C., MADÉ, B. & GOUZE, P. 2007b. Impact of coating development on the hydraulic and transport properties in argillaceous limestone fracture. *Water resources research,* 43.

NORDBOTTEN, J. M., CELIA, M. A. & BACHU, S. 2005. Injection and Storage of CO2 in Deep Saline Reservoir: Analytical Solution for CO2 Plume Evolution During Injection. *Transport in Porous Media,* 58**,** 339360.

ONUMA, T., OKADA, K. & OTSUBO, A. 2011. Time series analysis of surface deformation related with CO2 injection by satellite-borne SAR interferometry at In Salah, Algeria. *Energy Procedia,* 4**,** 3428-3434.

PACALA, S. & SOCOLOW, R. 2004. Stabilization Wedges: Solving the Climate Problem for the Next 50 Years with Current Technologies. *Science,* 305**,** 968-972.

PARRY, M.L., CANZIANI, O.F., PALUTIKOF, J.P., VAN DER LINDEN P.J., 2007. HANSON, C.E., *Contribution of Working Group II to the Fourth Assessment Report of the Intergovernmental Panel on Climate Change*. Cambridge University Press, Cambridge, United Kingdom and New York, NY, USA.

PASSEY, Q. R., BOHACS, K., ESCH, W. L., KLIMENTIDIS, R. & SINHA, S. 2010. From oil-prone source rock to gas-producing shale reservoir-geologic and petrophysical characterization of unconventional shale gas reservoirs. International oil and gas conference and exhibition in China. Society of Petroleum Engineers.

POLAK, A., ELSWORTH, D., YASUHARA, H., GRADER, A. & HALLECK, P. 2003. Permeability reduction of a natural fracture under net dissolution by hydrothermal fluids. *Geophysical Research Letters,* 30.

POORE, M. W., AND K. F. KESTERSON, 1978. Measuring the Thermal Expansion of Solids with Strain Gages, Journal of Testing and Evaluation, ASTM, Vol. 6, No. 2 (March 1978), pp. 98-102.

PRESTON, C., MONEA, M., JAZRAWI, W., BROWN, K., WHITTAKER, S., WHITE, D., LAW, D., CHALATURNYK, R. & ROSTRON, B. 2005. IEA GHG Weyburn CO2 monitoring and storage project. *Fuel Processing Technology,* 86**,** 1547-1568.

ROSENBAUER, R. J., KOKSALAN, T. & PALANDRI, J. L. 2005.

Experimental investigation of CO 2–brine–rock interactions at elevated temperature and pressure: implications for CO 2 sequestration in deepsaline reservoir. *Fuel processing technology,* 86**,** 1581-1597.

RUDNICKI, J. 1999. Alteration of regional stress by reservoirs and other inhomogeneities: stabilizing or destabilizing? 9th ISRM Congress. International Society for Rock Mechanics.

RUTQVIST, J., BIRKHOLZER, J. T. & TSANG, C.-F. 2008. Coupled reservoir–geomechanical analysis of the potential for tensile and shear failure associated with CO2 injection in multilayered reservoir–caprock systems. *International Journal of Rock Mechanics and Mining Sciences,* 45**,** 132-143.

SASS, J. H., LACHENBRUCH, A. H. & MUNROE, R. J. 1971. Component parts of the World Heat Flow Data Collection. PANGAEA.

SCHRAG, D. P. 2007. Preparing to Capture Carbon. *Science,* 315**,** 812-813.

SETTARI, A., WARREN, G.M., 1994. Simulation and Field Analysis of Waterflood Induced Fracturing. SIMTECH Consulting Services Ltd., Calgary, AB, Canada.

SEGALL, P. 1985. Stress and subsidence resulting from subsurface fluid withdrawal in the epicentral region of the 1983 Coalinga earthquake. *Journal of Geophysical Research: Solid Earth,* 90**,** 6801-6816.

SEGALL, P. & FITZGERALD, S. D. 1998. A note on induced stress changes in hydrocarbon and geothermal reservoirs. *Tectonophysics,* 289**,** 117-128.

SHAO, H., RAY, J. R. & JUN, Y.-S. 2010. Dissolution and precipitation of clay minerals under geologic CO2 sequestration conditions: CO2− brine− phlogopite interactions. *Environmental science & technology,* 44**,** 59996005.

SHEVALIER, M., NIGHTINGALE, M., MAYER, B., 2010. Geochemistry Wabamun Area CO2 Sequestration Project (WASP).

SHI, J.-Q., SINAYUC, C., DURUCAN, S. & KORRE, A. 2012. Assessment of carbon dioxide plume behaviour within the storage reservoir and the lower caprock around the KB-502 injection well at In Salah. *International Journal of Greenhouse Gas Control,* 7**,** 115-126.

SHIPTON, Z. K., EVANS, J. P., KIRSCHNER, D., KOLESAR, P. T., WILLIAMS, A. P. & HEATH, J. 2004. Analysis of CO2 leakage through 'low-permeability'faults from natural reservoirs in the Colorado Plateau, east-central Utah. *Geological Society, London, Special Publications,* 233**,** 43-58.

SHIRAKI, R. & DUNN, T. L. 2000. Experimental study on water–rock interactions during CO 2 flooding in the Tensleep Formation, Wyoming, USA. *Applied Geochemistry,* 15**,** 265-279.

SHUKLA, R., RANJITH, P., HAQUE, A. & CHOI, X. 2010. A review of studies on CO2 sequestration and caprock integrity. *Fuel,* 89**,** 2651-2664.

SINHA, S., BRAUN, E. M., DETERMAN, M. D., PASSEY, Q. R., LEONARDI, S. A., BOROS, J. A., WOOD III, A. C., ZIRKLE, T. & KUDVA, R. A. 2013. Steady-State Permeability Measurements on Intact Shale Samples at Reservoir Conditions - Effect of Stress, Temperature, Pressure, and Type of Gas. Society of Petroleum Engineers.

SMITH, J., DURUCAN, S., KORRE, A. & SHI, J.-Q. 2011. Carbon dioxide storage risk assessment: Analysis of caprock fracture network connectivity. *International Journal of Greenhouse Gas Control,* 5**,** 226240.

SNOW, D. T. 1969. Anisotropie permeability of fractured media. *Water Resources Research,* 5**,** 1273-1289.

SOLOMON, S. 2007. Carbon dioxide storage: Geological security and environmental issues–Case study on the sleipner gas field in Norway.

SOLTANZADEH, H., HAWKES, C., MCLELLAN, P. & SMITH, S. 2009. Poroelastic modelling of production and injection-induced stress changes in a pinnacle reef.

SOLTANZADEH, H. & HAWKES, C. D. 2008. Semi-analytical models for stress change and fault reactivation induced by reservoir production and injection. *Journal of Petroleum Science and Engineering,* 60**,** 71-85.

SOLTANZADEH, H., HAWKES, C. D. & SHARMA, J. S. 2007. Poroelastic model for production-and injection-induced stresses in reservoirs with elastic properties different from the surrounding rock. *International Journal of Geomechanics,* 7**,** 353-361.

SOMERTON, W. H. 1992. Thermal Properties and Temperature-Related Behavior of Rock Fluid Systems. *In:* SOMERTON, W. H. (ed.) *Thermal Properties and Temperature-Related Behavior of Rock Fluid Systems.* Elsevier.

SONDERGELD, C. H., AMBROSE, R. J., RAI, C. S. & MONCRIEFF, J. 2010. Micro-structural studies of gas shales. SPE Unconventional Gas Conference. Society of Petroleum Engineers.

SURVEY, A. G. 2015. *Alberta Table for Formations* [Online]. Alberta Energy Regulator. Available: http://ags.aer.ca/document/Table-of Formations.pdf. Accessed June 1, 2017.

SWITZER S.B., H. W. G., CHRISTIE D.S., GRAF G.C., HEDINGER A.S., MCAULEY R.J., WIERZBICKI R.A., PACKARD J.J. 1994. Devonian Woodbend - Winterburn Strata of the Western Canada Sedimentary Basin in Geological Atlas of the Western Canada Sedimentary Basin, Mossop G.D., Shetsen I. (comps.).

TAKENOUCHI, S. & KENNEDY, G. C. 1964. The binary system H 2 O-CO2 at high temperatures and pressures. *American Journal of Science,* 262**,** 1055-1074.

TERRATEK, 2011, Integrated tight rock analysis whole core Highvale 08-17051-03 W5M well, Report TR11-105-1207, Prepared for Schlumberger Carbon Services.

TANIKAWA, W. & SHIMAMOTO, T. 2006. Klinkenberg effect for gas permeability and its comparison to water permeability for porous sedimentary rocks. Hydrol. Earth Syst. Sci. Discuss., 2006, 1315-1338.

THOMAS, D. C. & BENSON, S. M. 2005. *Carbon Dioxide Capture for Storage in Deep Geologic Formations - Results from the CO2 Capture Project: Vol 1 - Capture and Separation of Carbon Dioxide from Combustion, Vol 2 - Geologic Storage of Carbon Dioxide with Monitoring and Verification,* Elsevier Science.

TRANSALTA, C. 2013. Final Report of Project Pioneer.

TRIMMER, D. 1981. Design criteria for laboratory measurements of low permeability rocks. *Geophys. Res. Lett.;(United States),* 8.

VASCO, D., RUCCI, A., FERRETTI, A., NOVALI, F., BISSELL, R., RINGROSE, P., MATHIESON, A. & WRIGHT, I. 2010. Satellite- based measurements of surface deformation reveal fluid flow associated with the geological storage of carbon dioxide. *Geophysical Research Letters,* 37.

VASCO, D. W. 2004. Estimation of flow properties using surface deformation and head data: A trajectory-based approach. *Water Resources Research***,** Medium: X; Size: vp.

VISWANATHAN, H. S., PAWAR, R. J., STAUFFER, P. H., KASZUBA, J. P., CAREY, J. W., OLSEN, S. C., KEATING, G. N., KAVETSKI, D. & GUTHRIE, G. D. 2008. Development of a hybrid process and system model for the assessment of wellbore leakage at a geologic CO2 sequestration site. *Environmental Science & Technology,* 42**,** 7280-7286.

WIGAND, M., KASZUBA, J. P., CAREY, J. W. & HOLLIS, W. K. 2009. Geochemical effects of CO 2 sequestration on fractured wellbore cement at the cement/caprock interface. *Chemical Geology,* 265**,** 122-133.

WILSON, E. J., KLASS, A. B. & BERGAN, S. 2009. Assessing a Liability Regime for Carbon Capture and Storage. *Energy Procedia*, 1**,** 4575-4582.

WRIGHT, G. N., MCMECHAN M.E., AND POTTER, D.E.G., 1994. Structure and architecture of the Western Canada Sedimentary Basin in Geological Atlas of the Western Canada Sedimentary Basin, G.D.Mossop and I. Shetsen (comp.).

XU, T., APPS, J. A. & PRUESS, K. 2004. Numerical simulation of CO2 disposal by mineral trapping in deep reservoir. *Applied Geochemistry*, 19**,** 917-936.

YAWS, C. L. 2008. *Thermophysical properties of chemicals and hydrocarbons*, William Andrew.

ZHANG, Y., OLDENBURG, C. M. & FINSTERLE, S. 2010. Percolation-theory and fuzzy rule-based probability estimation of fault leakage at geologic carbon sequestration sites. Environmental Earth Sciences, 59, 1447-1459.

APPENDIX A . PETROGRAPHIC IMAGES DATA

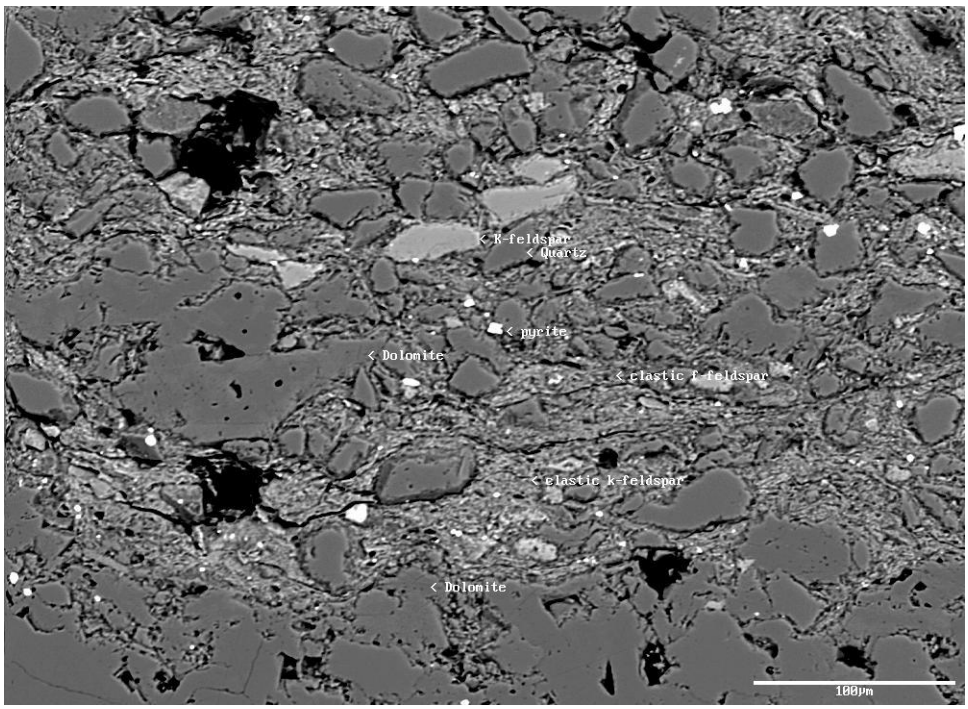

A. 2. SEM whole view image for sample CMR1. EDS identifies in this sample image as quartz, dolomite, pyrite and k-feldspar.

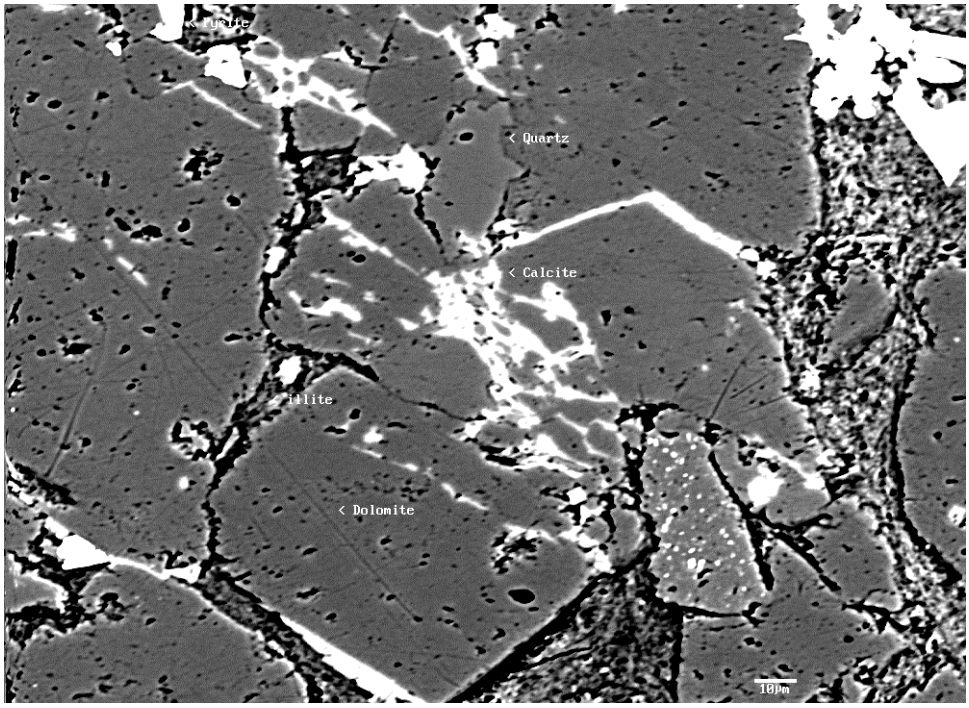

A.2. SEM whole view image for sample CMR2. EDS identifies in this sample image has quartz, dolomite, pyrite and calcite.

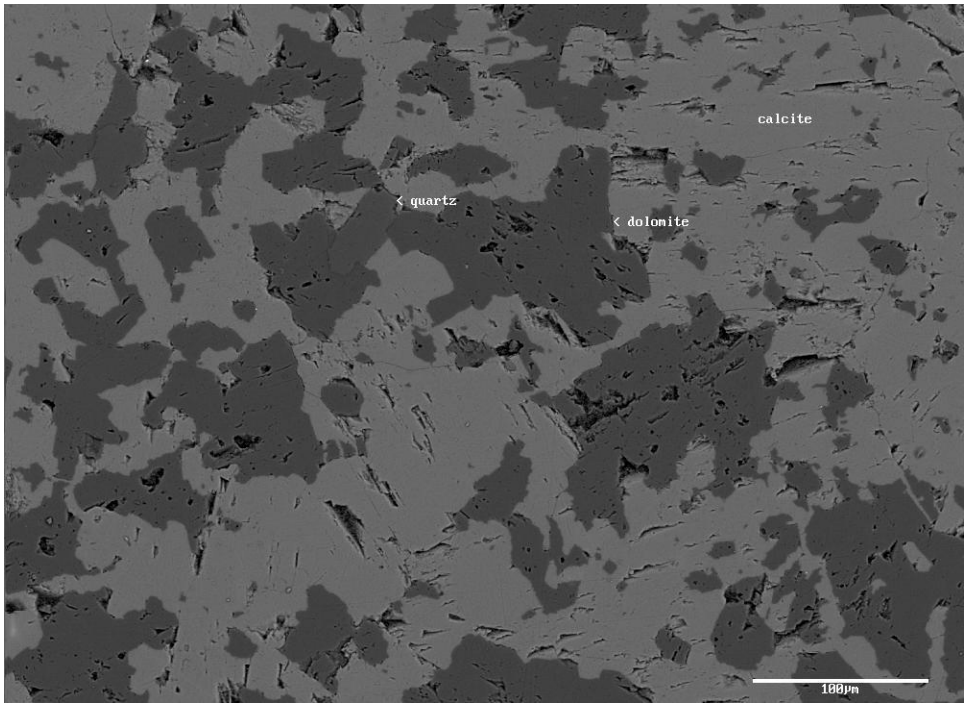

A.3. SEM whole view image for sample CMR3. EDS identifies in this sample image has quartz, dolomite and calcite.

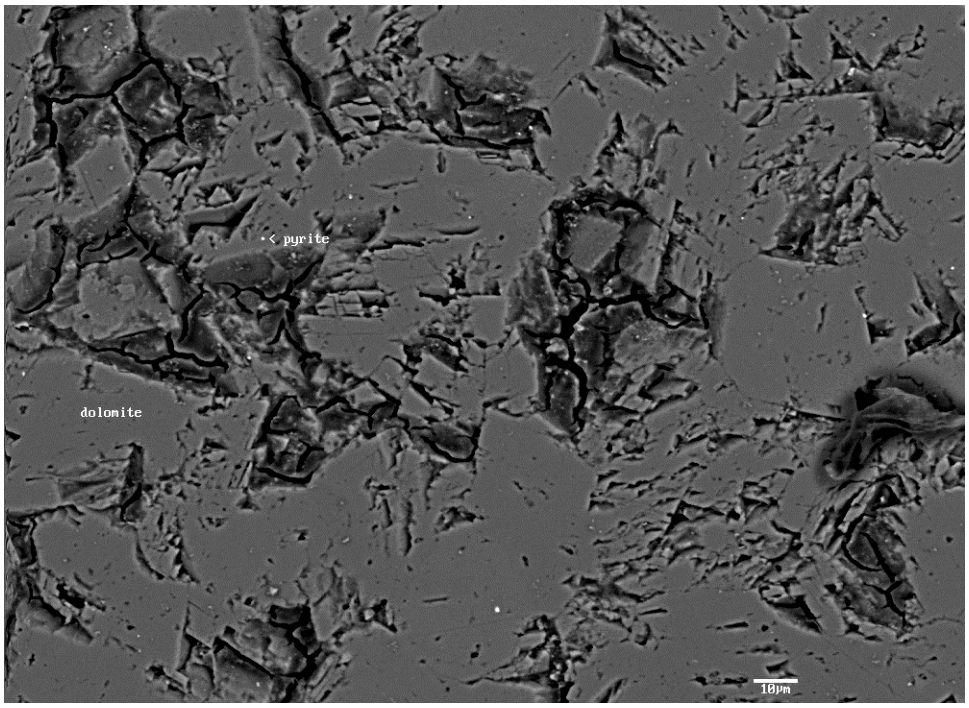

A.4. SEM whole view image for sample CMR4. EDS identifies in this sample image has dolomite and pyrite.

APPENDIX B. THERMAL PROPERTIES DATA

B.1. Linear thermal expansion data of Nisku 1 (NSK1) and Nisku 4 (NSK4) core plugs.

Temp (°C)	NSK1 ξ Axial (μξ)	ξ Lateral (μξ)	NSK4 ξ Axial (μξ)	ξ Lateral (μξ)	NSK1 α_T-axial (μξ/°C)	α_T-radial (μξ/°C)	NSK4 α_T-axial (μξ/°C)	α_T-radial (μξ/°C)
27.12	18	5	15	14				
33.47	43	17	38	35	3.94	1.89	3.62	3.31
44.87	89	48	80	75	4.04	2.72	3.68	3.51
63.57	160	113	145	144	3.80	3.48	3.48	3.69
45.19	82	48	73	69	4.24	3.54	3.92	4.08
34.22	36	17	33	27	4.19	2.83	3.65	3.83
28.04	12	5	11	6	3.88	1.94	3.56	3.40

B.2. Linear thermal expansion data of Nisku 2 (NSK2) and Nisku 5 (NSK5) core plugs.

Temp (°C)	NSK2 ξ Axial (μξ)	ξ Lateral (μξ)	NSK5 ξ Axial (μξ)	ξ Lateral (μξ)	NSK2 α_T-axial (μξ/°C)	α_T-radial (μξ/°C)	NSK5 α_T-axial (μξ/°C)	α_T-radial (μξ/°C)
22.88	1	0	0	0				
29.19	26	24	24	21	3.96	3.80	3.80	3.33
35.32	49	45	45	40	3.75	3.43	3.43	3.10
48.83	100	94	93	84	3.77	3.63	3.55	3.26
58.37	134	125	127	116	3.56	3.25	3.56	3.35
64.43	157	148	150	139	3.80	3.80	3.80	3.80
58.29	132	124	126	115	4.07	3.91	3.91	3.91
48.69	93	86	86	77	4.06	3.96	4.17	3.96
35.56	43	39	37	32	3.81	3.58	3.73	3.43
29.51	21	18	17	12	3.64	3.47	3.31	3.31
22.83	-3	-4	-5	-7	3.59	3.29	3.29	2.84

B.3. Linear thermal expansion data of Nisku 3 (NSK3) core plug.

NSK3 Temp (°C)	ξ Axial (μξ)	ξ Lateral (μξ)	α_T-axial (μξ/°C)	α_T-radial (μξ/°C)
22.51	-12	-12		
41.6	60	63	3.77	3.93
50.26	94	101	3.93	4.39
60.73	132	145	3.63	4.20
50.41	91	102	3.97	4.17
41.68	58	66	3.78	4.12
32.85	25	31	3.74	3.96
22.71	-12	-7	3.65	5

B.4. Linear thermal expansion data of Calmar 1 and 2(CMR1 & 2) core plugs.

Temp (°C)	CMR1 ξ Axial (μξ)	ξ Lateral (μξ)	CMR2 ξ Axial (μξ)	ξ Lateral (μξ)	CMR1 α_T-axial (μξ/°C)	α_T-radial (μξ/°C)	CMR2 α_T-axial (μξ/°C)	α_T-radial (μξ/°C)
27.74	16	17	21	18				
45.04	75	75	96	82	3.41	3.35	4.34	3.70
63.07	135	136	140	143	3.33	3.38	2.44	3.38
45.26	75	72	69	77	3.37	3.59	3.99	3.71
27.13	13	11	13	17	3.42	3.36	3.09	3.31

B.5. Linear thermal expansion data of Calmar Formation sample 3 and 4 (CMR3 & 4) core plugs.

Temp (°C)	CMR3 ξ Axial (μξ)	ξ Lateral (μξ)	CMR4 ξ Axial (μξ)	ξ Lateral (μξ)	CMR3 α_T-axial (μξ/°C)	α_T-radial (μξ/°C)	CMR4 α_T-axial (μξ/°C)	α_T-radial (μξ/°C)
28.84	-20	-21	-20	-20				
46.26	131	68	128	96	8.67	5.11	8.50	6.66
62.36	263	142	263	212	8.20	4.60	8.39	7.20
44.95	149	97	150	129	6.55	2.58	6.49	4.77
28.74	14	18	15	26	8.33	4.87	8.33	6.35
				Average	7.94	4.29	7.92	6.25

B.6. Thermal transport data table of CMR1.

Thermal Conductivity (W/m°C)	Specific Heat (MJ/m³°C)	Probing Depth (mm)	Temperature Increase (°C)	Mean Deviation	Thermal Diffusivity (mm²/s)	Sensor Resistance (Ω)
3.58	2.04	12.40	4.99	0.00	1.75	12.29
3.56	2.03	12.40	5.01	0.01	1.75	12.30
3.55	2.09	12.20	5.02	0.01	1.70	12.30
3.65	1.98	12.70	4.89	0.00	1.85	12.30
3.63	1.98	12.70	3.09	0.01	1.84	12.28
3.59	2.00	12.50	4.98	0.00	1.79	12.29

B.7. Thermal transport data table of CMR2.

Thermal Conductivity (W/m°C)	Specific Heat (MJ/m³°C)	Probing Depth (mm)	Temperature Increase (°C)	Mean Deviation	Thermal Diffusivity (mm²/s)	Sensor Resistance (Ω)
2.89	2.01	12.30	6.49	0.00	1.44	12.35
2.85	1.98	12.30	6.55	0.00	1.44	12.35
2.86	2.01	12.30	6.55	0.00	1.42	12.35
3.39	2.43	12.60	5.78	0.00	1.39	12.36
3.37	2.47	12.50	5.81	0.00	1.37	12.36
3.36	2.36	12.80	5.82	0.00	1.43	12.34

B.8. Thermal transport data table of CMR3.

Thermal Conductivity (W/m°C)	Specific Heat (MJ/m³°C)	Probing Depth (mm)	Temperature Increase (°C)	Mean Deviation	Thermal Diffusivity (mm²/s)	Sensor Resistance (Ω)
3.69	2.65	12.60	4.06	0.00	1.39	12.33
3.64	2.53	12.80	4.11	0.00	1.44	12.32
3.63	2.62	12.60	4.13	0.00	1.39	12.31
3.65	2.60	12.64	4.10	0.00	1.41	12.32
4.45	3.43	12.50	3.45	0.00	1.30	12.34
4.06	3.10	12.60	3.79	0.00	1.31	12.33
3.97	3.35	12.00	3.87	0.00	1.18	12.33
4.02	3.23	12.28	3.83	0.00	1.25	12.33

B.9. Thermal transport data table of CMR4.

Thermal Conductivity (W/m°C)	Specific Heat (MJ/m³°C)	Probing Depth (mm)	Temperature Increase (°C)	Mean Deviation	Thermal Diffusivity (mm²/s)	Sensor Resistance (Ω)
4.60	2.43	12.40	3.06	0.00	1.89	12.36
4.64	2.50	12.60	3.16	0.00	1.85	12.34
4.53	2.37	12.50	3.10	0.00	1.91	12.33
4.59	2.44	12.49	3.10	0.00	1.88	12.34
4.56	2.35	11.90	1.84	0.00	1.94	12.26
4.52	2.31	11.90	3.86	0.00	1.96	12.29
4.57	2.40	11.70	3.86	0.00	1.91	12.30
4.07	1.35	12.80	3.12	0.00	3.02	12.35
4.04	1.34	12.70	3.88	0.00	3.03	12.34
4.03	1.35	12.80	3.91	0.00	2.99	12.34
4.05	1.34	12.77	3.64	0.00	3.01	12.34
4.06	1.47	12.60	2.94	0.00	2.76	12.35

APPENDIX C. MATRIX REACTIVITY IMAGES

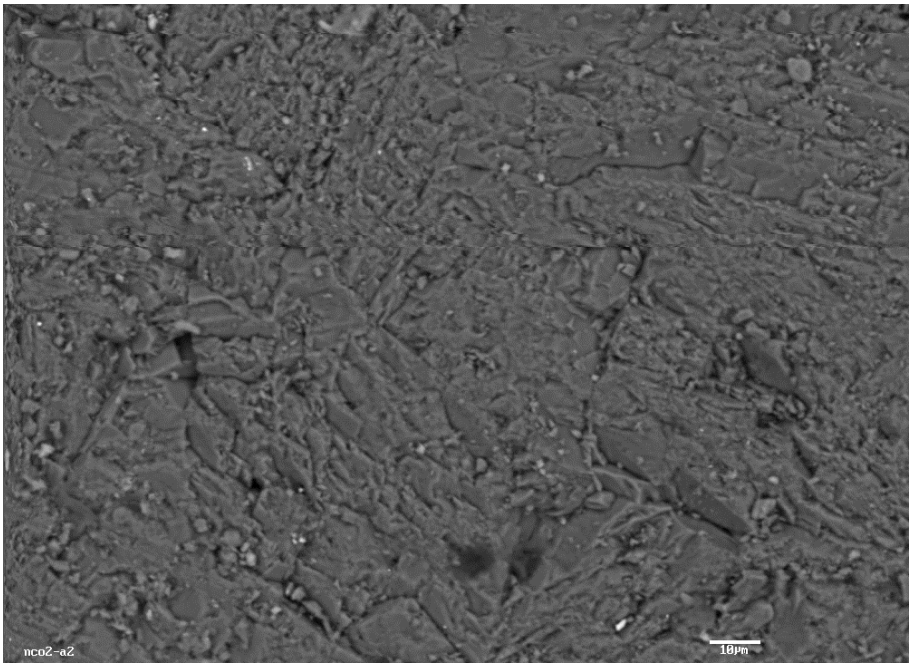

C.1. SEM whole view image for sample CMR3 of side A. EDS identifies in this sample image as NaCl with minor calcite dolostone.

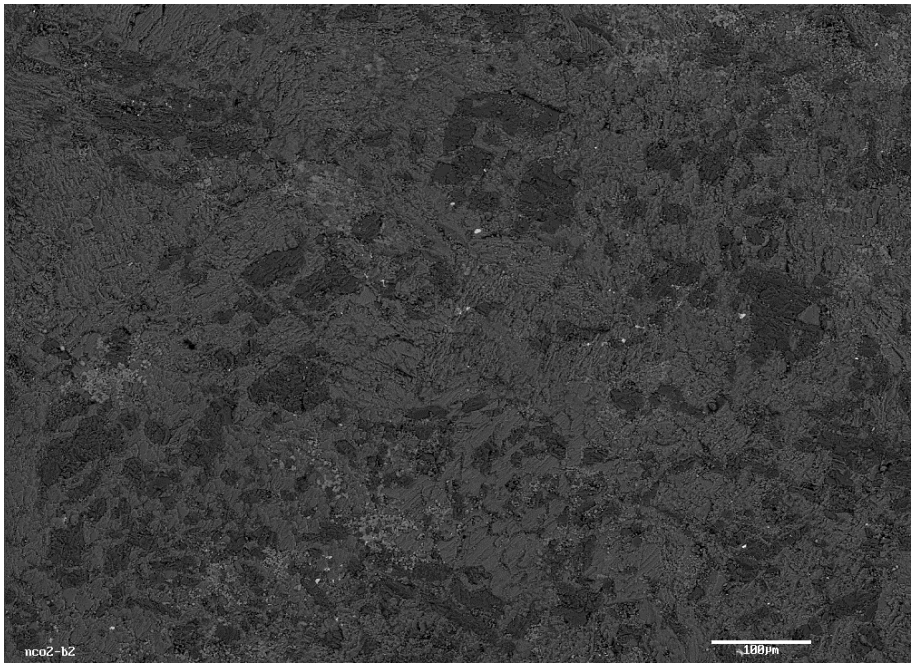

C.2. SEM whole view image for sample CMR3 of side B. EDS identifies in this sample image as dolomite with Cl (epoxy), calcite and pyrite.

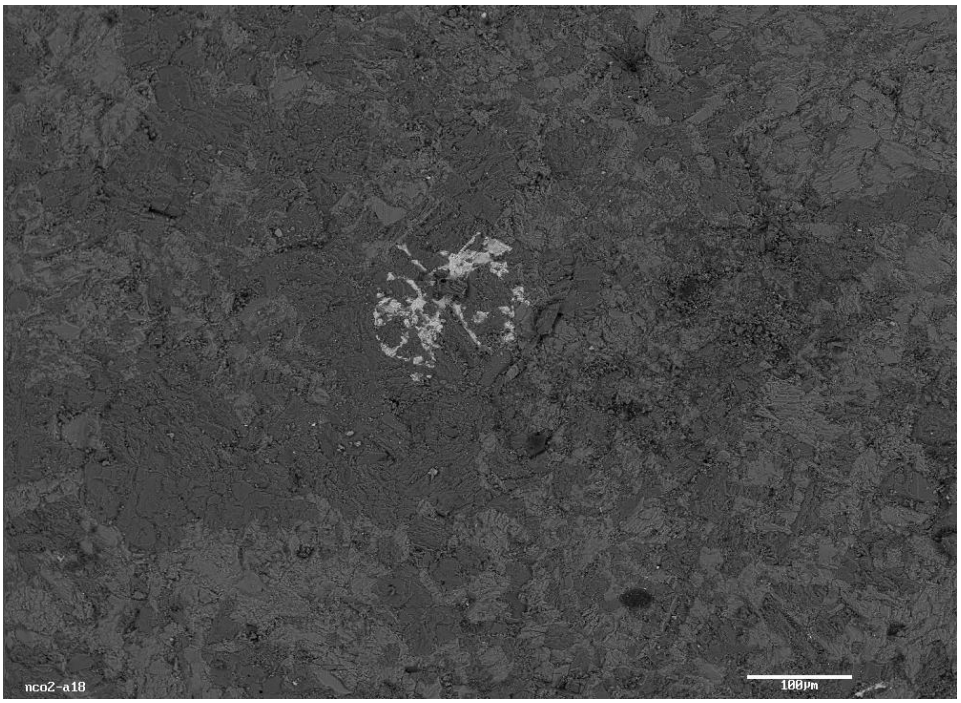

C.3. SEM whole view image for sample CMR3 of side A′. EDS identifies in this sample image as pyrite, calcite and dolomite.

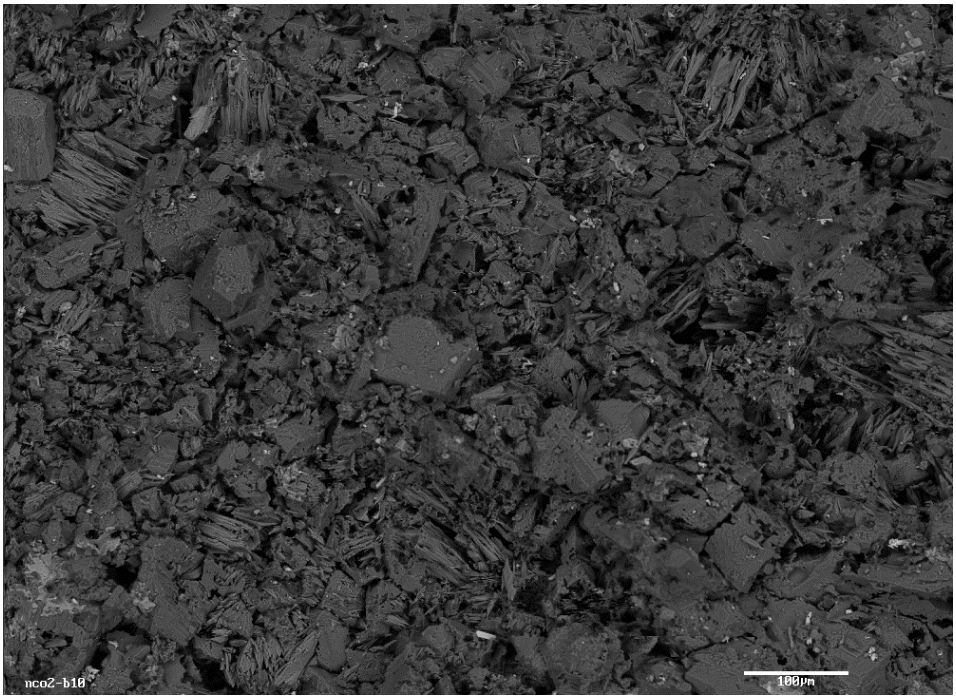

C.4. SEM images for sample CMR3 side B′. EDS identifies in this sample image as pyrite, calcite, dolomite, silicates and K-feldspar.

APPENDIX D. FRACTURED PERMEABILITY DATA

Table D.1. The data of fractured permeability of sample CMR1.

Cell press (Pa)	Cell Temp (°C)	Room Temp (°C)	Flow Rate (m^3/sec)	Pressure Difference (Pa)	k (m^2)
17492006.12	62.7	22.41	2.17E-09	1778847.38	1.3E-17
17492006.12	57.14	22.45	2.17E-09	1778847.38	1.3E-17
17492006.12	53.28	22.51	2.17E-09	1785742.14	1.29E-17
17492006.12	50.71	22.39	1.3E-09	1785742.14	7.77E-18
17492006.12	72.45	22.33	2.17E-09	1785742.14	1.29E-17
17492006.12	66.88	22.41	1.73E-09	1785742.14	1.04E-17
17492006.12	60	22.37	1.3E-09	1785742.14	7.77E-18
17492006.12	55.28	22.42	2.17E-09	1785742.14	1.29E-17
17492006.12	52.18	22.36	1.73E-09	1785742.14	1.04E-17
17492006.12	74.02	22.3	1.3E-09	1785742.14	7.77E-18
17492006.12	67.33	22.3	2.17E-09	1785742.14	1.29E-17
17492006.12	60.32	22.34	8.67E-10	1785742.14	5.18E-18
17492006.12	55.43	22.39	1.3E-09	1785742.14	7.77E-18
17492006.12	63.14	22.35	2.17E-09	1785742.14	1.29E-17
17492006.12	75.52	22.33	8.67E-10	1785742.14	5.18E-18
17492006.12	66.74	22.35	2.17E-09	1785742.14	1.29E-17
17498900.88	59.69	22.39	8.67E-10	1778847.38	5.2E-18
17492006.12	54.96	22.31	1.3E-09	1785742.90	7.74E-18
17492006.12	72.19	22.38	8.67E-10	1785742.14	5.18E-18
17498900.88	71.74	22.41	2.17E-09	1778847.38	1.3E-17
17498900.88	63.55	22.28	1.3E-09	1785742.14	7.77E-18
17498900.88	57.58	22.3	8.67E-10	1785742.14	5.18E-18
17492006.12	56.68	22.3	1.3E-09	1785742.14	7.77E-18
17492006.12	78.93	22.29	1.73E-09	1785742.90	1.03E-17
17492006.12	69.91	22.25	1.3E-09	1785742.90	7.74E-18
17498900.88	61.79	22.42	8.67E-10	1778847.38	5.2E-18
17498900.88	56.25	22.44	1.3E-09	1785742.14	7.77E-18
17498900.88	67.44	22.39	2.17E-09	1785742.14	1.29E-17
17492006.12	73.42	22.33	8.67E-10	1785742.14	5.18E-18
17498900.88	64.89	22.42	1.3E-09	1785742.14	7.77E-18
17492006.12	58.3	22.41	8.67E-10	1785742.14	5.18E-18
17492006.12	55.76	22.22	8.67E-10	1785742.90	5.16E-18
17498900.88	76.37	22.18	1.3E-09	1778847.38	7.8E-18
17498900.88	68.08	22.34	2.17E-09	1778847.38	1.3E-17
17498900.88	60.65	22.45	8.67E-10	1778847.38	5.2E-18
17492006.12	55.42	22.34	1.3E-09	1785742.90	7.74E-18
17498900.88	76.28	22.32	8.67E-10	1785742.14	5.18E-18

17498900.88	71.29	22.35	8.67E-10	1785742.14	5.18E-18
17498900.88	62.99	22.29	1.3E-09	1785742.14	7.77E-18
17498900.88	57	22.36	8.67E-10	1785742.14	5.18E-18
17498900.88	71.35	22.31	1.3E-09	1785742.14	7.77E-18
17498900.88	73.29	22.23	8.67E-10	1785742.14	5.18E-18
17498900.88	64.56	22.29	1.3E-09	1785742.14	7.77E-18
17498900.88	58.02	22.35	8.67E-10	1778847.38	5.2E-18
17498900.88	64.2	22.31	1.3E-09	1785742.14	7.77E-18
17498900.88	75.23	22.33	8.67E-10	1785742.14	5.18E-18
17498900.88	66.22	22.32	1.3E-09	1785742.14	7.77E-18
17492006.12	59.05	22.31	8.67E-10	1785742.90	5.16E-18
17498900.88	55.46	22.3	1.3E-09	1785742.14	7.77E-18
17492006.12	72.89	22.23	8.67E-10	1785742.90	5.16E-18
17498900.88	63.89	22.25	8.67E-10	1785742.14	5.18E-18
17498900.88	58.2	22.27	1.3E-09	1785742.14	7.77E-18
17498900.88	54.38	22.26	8.67E-10	1785742.14	5.18E-18
17498900.88	70.74	22.28	1.3E-09	1785742.14	7.77E-18
17498900.88	64.86	22.24	8.67E-10	1785742.14	5.18E-18
17498900.88	58.84	22.24	1.3E-09	1785742.14	7.77E-18
17492006.12	55.37	22.27	8.67E-10	1785742.90	5.16E-18
17498900.88	73.38	22.34	0	1785742.14	0
17498900.88	66.49	22.31	8.67E-10	1785742.14	5.18E-18
17498900.88	59.9	22.36	1.3E-09	1785742.14	7.77E-18
17498900.88	55.4	22.31	8.67E-10	1785742.14	5.18E-18
17498900.88	72.34	22.31	1.3E-09	1785742.14	7.77E-18
17498900.88	67.23	22.34	0	1785742.14	0
17498900.88	60.62	22.28	8.67E-10	1785742.14	5.18E-18
17498900.88	55.98	22.29	1.3E-09	1785742.14	7.77E-18
17498900.88	70.34	22.3	8.67E-10	1785742.14	5.18E-18
17492006.12	67.33	22.4	0	1785742.90	0
17498900.88	60.63	22.46	1.3E-09	1785742.14	7.77E-18
17498900.88	55.89	22.46	8.67E-10	1785742.14	5.18E-18
17498900.88	72.02	22.32	8.67E-10	1785742.14	5.18E-18
17498900.88	67.2	22.4	0	1785742.14	0
17498900.88	60.49	22.42	1.3E-09	1785742.14	7.77E-18
17498900.88	55.75	22.41	8.67E-10	1785742.14	5.18E-18
17498900.88	71.57	22.28	0	1785742.14	0
17498900.88	66.54	22.44	1.3E-09	1785742.14	7.77E-18
17498900.88	60.02	22.3	8.67E-10	1785742.14	5.18E-18
17498900.88	55.46	22.26	1.3E-09	1785742.14	7.77E-18
17498900.88	71.2	22.3	0	1785742.14	0
17498900.88	65.01	22.3	8.67E-10	1785742.14	5.18E-18
17498900.88	58.97	22.2	8.67E-10	1785742.14	5.18E-18

17498900.88	55.39	22.25	0	1785742.14	0
17498900.88	71.13	22.17	1.3E-09	1785742.14	7.77E-18
17498900.88	64.57	22.22	0	1785742.14	0
17498900.88	58.56	22.19	8.67E-10	1785742.14	5.18E-18
17498900.88	57.02	22.17	1.3E-09	1785742.14	7.77E-18
17498900.88	70.74	22.27	0	1785742.14	0
17492006.12	63.86	22.26	8.67E-10	1785742.90	5.16E-18
17498900.88	58.07	22.32	1.3E-09	1785742.14	7.77E-18
17498900.88	60.61	22.25	0	1785742.14	0
17498900.88	70.11	22.19	8.67E-10	1785742.14	5.18E-18
17498900.88	63.07	22.26	0	1785742.14	0
17492006.12	57.44	22.27	1.3E-09	1785742.90	7.74E-18
17498900.88	65.67	22.16	8.67E-10	1785742.14	5.18E-18
17498900.88	69.26	22.44	0	1785742.14	0
17492006.12	62.08	22.33	8.67E-10	1785742.90	5.16E-18
17492006.12	56.82	22.3	1.3E-09	1785742.90	7.74E-18
17498900.88	70.21	22.3	0	1785742.14	0
17498900.88	67.77	22.27	8.67E-10	1785742.14	5.18E-18
17498900.88	60.81	22.28	0	1785742.14	0
17498900.88	55.88	22.25	1.3E-09	1785742.14	7.77E-18
17498900.88	73.08	22.21	8.67E-10	1785742.14	5.18E-18
17498900.88	67.35	22.25	0	1785742.14	0
17498900.88	60.51	22.31	1.3E-09	1785742.14	7.77E-18
17498900.88	55.7	22.22	8.67E-10	1785742.14	5.18E-18
17498900.88	72.27	22.23	0	1785742.14	0
17498900.88	66	22.27	1.3E-09	1785742.14	7.77E-18
17498900.88	59.54	22.18	0	1785742.14	0
17498900.88	56.58	22.26	8.67E-10	1785742.14	5.18E-18
17498900.88	71.52	22.34	8.67E-10	1785742.14	5.18E-18
17498900.88	64.55	22.37	0	1785742.14	0
17498900.88	58.52	22.28	1.3E-09	1785742.14	7.77E-18
17498900.88	60.1	22.28	0	1785742.14	0
17498900.88	70.24	22.41	8.67E-10	1785742.14	5.18E-18
17498900.88	63.08	22.23	1.3E-09	1785742.14	7.77E-18
17498900.88	57.52	22.35	0	1785742.14	0
17498900.88	66.29	22.29	8.67E-10	1785742.14	5.18E-18
17498900.88	68.95	22.34	0	1785742.14	0
17498900.88	61.85	22.31	1.3E-09	1785742.14	7.77E-18
17498900.88	56.59	22.27	0	1785742.14	0
17498900.88	70.87	22.15	8.67E-10	1785742.14	5.18E-18
17498900.88	67.14	22.24	0	1785742.14	0
17498900.88	60.45	22.29	1.3E-09	1785742.14	7.77E-18
17498900.88	55.67	22.22	4.33E-10	1785742.14	2.59E-18

17498900.88	71.74	22.27	4.33E-10	1785742.14	2.59E-18
17498900.88	65.87	22.2	8.67E-10	1785742.14	5.18E-18
17498900.88	59.39	22.29	0	1785742.14	0
17498900.88	56.58	22.25	1.3E-09	1785742.14	7.77E-18
17498900.88	70.96	22.2	0	1785742.14	0
17498900.88	63.95	22.24	8.67E-10	1785742.14	5.18E-18
17498900.88	57.98	22.28	0	1785742.14	0
17498900.88	63.17	22.3	1.3E-09	1785742.14	7.77E-18
17498900.88	69.7	22.18	0	1785742.14	0
17498900.88	62.48	22.13	8.67E-10	1785742.14	5.18E-18
17498900.88	56.95	22.18	0	1785742.14	0
17498900.88	70.28	22.15	1.3E-09	1785742.14	7.77E-18
17498900.88	67.89	22.16	0	1785742.14	0
17498900.88	60.8	22.26	8.67E-10	1785742.14	5.18E-18
17498900.88	55.82	22.17	0	1785742.14	0
17498900.88	71.6	22.15	8.67E-10	1785742.14	5.18E-18

APPENDIX E. TEMPERATURE DISTRIBUTION AROUND CO_2 INJECTION WELL

Within the CO_2 plume, dimensionless temperature change is found as follows:

$$T_D = \text{erfc}\left(\sqrt{\tau_D}\frac{{R_D}^2}{2(1-{R_D}^2)}\right) \quad (2.9)$$

Where

$$T_D = \frac{T - T_{res}}{T_{inj} - T_{res}}$$

Therefore, temperature change can be calcualted as follows:

$$T - T_{res} = (T_{inj} - T_{res}) \times \text{erfc}\left(\sqrt{\tau_D}\frac{{R_D}^2}{2(1-{R_D}^2)}\right)$$

Direct input parameters are as follows:

T_{res} = initial reservoir temperature (°C)

T_{inj} = injection temperature (°C)

M_w = heat capacity of injection fluid (kJ m^{-3} °C^{-1})

M_s = heat capacity of cap and base rock (kJ m^{-3} °C^{-1})

t = injection time (days)

h = reservoir height (m)

$\emptyset$ = porosity

S_{wr} = residual water saturation

K = thermal diffusivity of cap and base rock ($m^2 day^{-1}$)

Calculated input parameters are as follows:

M_r = heat capacity of fluid filled reservoir rock (kJ m^{-3} °C^{-1})

q = injection rate ($m^3 day^{-1}$)

Then R_C (radius of temperature front) can be calculated as follows

$$R_C = \left(\frac{M_w}{M_r}\frac{qt}{h\pi}\right)^{\frac{1}{2}}$$

$$R_C = \left(\frac{(1582.69)}{(2627.74)} \times \frac{(3195.06)\times(18250)}{(70)\times(3.1415)}\right)^{\frac{1}{2}}$$

$$R_C = 399.63 \text{ m}$$

Constant τ_D can be calculated as follows:

$$\tau_D = \frac{4KtM_s^2}{h^2M_r^2}$$

$$\tau_D = \frac{(4)\times(1.33\cdot 10^{-6})\times(18250)\times(2627.74)^2}{(70)^2\times(2627.74)^2}$$

$$\tau_D = 1.75$$

Sample calculation at r = 100 m:

$$R_D = \frac{r}{R_c} = \frac{100}{R_c}$$

$$R_D = \frac{100}{399.63}$$

$$R_D = 0.25.$$

And,

$$T - T_{res} = (T_{0inj} - T_{res}) \times \text{erfc}\left(\sqrt{\tau_D}\frac{R_D^2}{2(1-R_D^2)}\right)$$

$$T - T_{res} = (30 - 70) \times \text{erfc}\left((1.75) \times \frac{(0.25)^2}{2(1-(0.25)^2)}\right)$$

$$T - T_{res} = -38.027\ (°C)$$

See Table E.1 for calculated temperatures within the temperature profile highlighted in red box.

.

Table E.1. Data of temperature distribution after injection with 10 m increments.

r (m)	R_D	T_D	ΔT (°C)
10	0.025	1.000	-39.981
20	0.050	0.998	-39.926
30	0.075	0.996	-39.833
40	0.100	0.993	-39.701
50	0.125	0.988	-39.530
60	0.150	0.983	-39.319
70	0.175	0.977	-39.065
80	0.200	0.969	-38.767
90	0.225	0.961	-38.422
100	0.250	0.951	-38.027
110	0.275	0.939	-37.580
120	0.300	0.927	-37.076
130	0.325	0.913	-36.510
140	0.350	0.897	-35.878
150	0.375	0.879	-35.173
160	0.400	0.860	-34.388
170	0.425	0.838	-33.516
180	0.450	0.814	-32.548
190	0.475	0.787	-31.474
200	0.500	0.757	-30.281
210	0.525	0.724	-28.957
220	0.551	0.687	-27.489
230	0.576	0.647	-25.861
240	0.601	0.601	-24.058
250	0.626	0.552	-22.065
260	0.651	0.497	-19.871
270	0.676	0.437	-17.473
280	0.701	0.372	-14.878
290	0.726	0.303	-12.121
300	0.751	0.232	-9.276
310	0.776	0.162	-6.473
320	0.801	0.098	-3.921
330	0.826	0.047	-1.887
340	0.851	0.015	-0.609
350	0.876	0.002	-0.092
360	0.901	0.000	-0.003
370	0.926	0.000	0.000
380	0.951	0.000	0.000
390	0.976	0.000	0.000
400	1.001	0.000	0.000

Appendix F. Effluent Chemical Sample Protocol

Every effluent sample was collected at the end of every cycle through the fractured sample. The effluent samples were filtered through a 0.45 um filter within less than 5 minutes of collecting it to avoid the possible precipitates. Afterwards a dilution process were performed.

For trace metals (Fe, Mg, Mn etc) a 1:10 dilution with 0.1 M nitric acid was done. This diluted and preserved the sample. For about 20 mL of final sample to be tested a 2 mL effluent sample from the experiment was added with 18 mL of 0.1 M nitric acid.

For cations a 1:10 dilution with deionized, distilled water was done. For about 20 mL of final sample to be tested a 2 mL effluent sample from the experiment was added with 18 mL deionized, distilled water to preserve the anions to be analysed.

For Si analyses 2 mL to 8 mL of distilled deionized water was used. For Bicarbonate analysis, which was comparatively difficult, a titration process was performed with sulphuric acid of 0.1 M within 10 minutes of collecting the sample. A titration of 10 ml of raw, unfiltered water was used to determine total alkalinity. Remember that this number is all of the titratable species, so not just bicarbonate but other titratable species, like boron, organic acids etc.